INVESTIGATIONS ON MAGNETIC AND SEMICONDUCTING NANOMATERIALS PREPARED BY SOL-GEL AND ELECTROSPINNING ROUTES

A thesis submitted

by

Arnab Kumar Das

to

Indian Institute of Technology Guwahati

in

partial fulfillment of the requirement for the award of the degree of
Doctor of Philosophy in Physics

Department of Physics
Indian Institute of Technology Guwahati
Guwahati 781 039, Assam, India

May 2018

INVESTIGATIONS ON MAGNETIC AND SEMICONDUCTING NANOMATERIALS PREPARED BY SOL-GEL AND ELECTROSPINNING ROUTES

A thesis submitted

by

Arnab Kumar Das

to

Indian Institute of Technology Guwahati

in

partial fulfillment of the requirement for the award of the degree of
Doctor of Philosophy in Physics

Department of Physics
Indian Institute of Technology Guwahati
Guwahati 781 039, Assam, India

May 2018

STATEMENT

The work contained in the thesis entitled "***Investigations on magnetic and semiconducting nanomaterials prepared by sol-gel and electrospinning routes***" has been carried out by me under the supervision of Prof. A. Srinivasan, at the Department of Physics, Indian Institute of Technology Guwahati. This work has not been submitted elsewhere for the award of any degree.

Arnab Kumar Das

28th May 2018

(Arnab Kumar Das)
Roll No: 11612120
Department of Physics
Indian Institute of Technology Guwahati
Guwahati – 781039
India.

CERTIFICATE

It is certified that the work contained in the thesis entitled "***Investigations on magnetic and semiconducting nanomaterials prepared by sol-gel and electrospinning routes***" submitted by Arnab Kumar Das (Roll No: 11612120), a Ph. D. student of the Department of Physics, Indian Institute of Technology Guwahati for the award of degree of Doctor of Philosophy has been carried out under the supervision of Prof. A. Srinivasan. This work has not been submitted elsewhere for the award of any degree.

28th May 2018

(Dr. A. Srinivasan)
Professor
Department of Physics
Indian Institute of Technology Guwahati
Guwahati – 781039
India.

Dedicated to

My beloved parents . . .

ACKNOWLEDGEMENTS

It is my privilege to express my deep sense of gratitude to my thesis supervisor Prof. A. Srinivasan for his resourceful guidance, constructive criticisms and careful supervision in guiding me throughout my research work. His knowledge, relevant ideas and energetic spirit have helped me to complete the thesis work successfully. I am grateful to my doctoral committee members (Prof. A. Perumal, Prof. P. Padmanabhan, Dr. D. Pamu and Prof. P.S. Robi) for reviewing my research work regularly and providing valuable guidelines and suggestions for the improvement of my research work. I am thankful to Prof. Subhradip Ghosh, the current Head, Department of Physics, and former Heads, Prof. S. Basu and Prof. P. Poulose, for their immense support.

I am very much thankful to Dr. Manoranjan Kar, IIT Patna for his help in Raman measurement of ZnO samples.

I am thankful to Dr. Ramanujan Govindaraj, kalpakkam, for his help in Mössbauer measurements on $CaFe_2O_4$ samples.

I am grateful to Indian Institute of Technology Guwahati, and the Ministry of Human Resource Development, Government of India, for the financial support.

I express my sincere thanks to Dr. Sidananda Sarma, Scientific Officer in Department of Physics, for guiding me to operate various high precision instruments in the department. Also, I thank Mr. Chandan Borgohain, Dr. Kula Kamal Senapati and Mr. Kesho Singh, Scientific Officers of Central Instruments Facility for patiently and enthusiastically extending their expertise in handling various instruments used for my research work.

I am fortunate to have my seniors, Dr. Bhargab Deka, Dr. Rahul Das and other lab seniors, Dr. Akhilesh Kr. Singh, Mr. Bhagban Kisan, Dr. P.C. Shyni, Dr. Tribedi Bora and Dr. Ramesh Ghosh who helped me in various ways throughout my research work. My lab mates, Dr. Bipul Deka, Dr. R. Gopalrao, Ravi, Budhadeb, Pratap, Kamal, Camelia, Aneeta, Manisha and Nitu will always be remembered for the wonderful time we shared together. I thank Rajkumar a lot for all his help and criticisms.

I owe a lot to my beloved parents. My parents have encouraged me lot to pursue my PhD career. Without their infinite motivation and support I could not have finished my PhD. I sincerely thank my brothers (Asoke), sister (Rimi) and all my family members for their

moral support and constant encouragements. My dear Dadu and my Mother are responsible for whatever minimal success I have achieved in my life, and they will remain the major motivation for me till the last day of my life. Finally, my sincere thanks are due to all those have been helped me in whatever manner and brought me to this position, some of whom I may have inadvertently forgotten to mention in this acknowledgement.

Arnab Kumar Das

Arnab Kumar Das

PREFACE

Low dimensional or nanostructured materials offer several advantages over their bulk counterparts due to quantum confinement along one or more dimensions. As a consequence, it is possible to tailor their properties and exploit phenomena that are specific only to these low dimensional materials. Such attempts have led to the development of nanomaterials for several new applications in optoelectronics, spintronics and health care. This thesis explores the synthesis and properties of two classes of materials, namely, dilute magnetic semiconductors (DMS) and non-spinel type ferrites in their nanocrystalline forms in order to evaluate them for possible applications.

DMS are spintronic materials which are being synthesized and theoretically modeled since several years. However, the current interest is to obtain ferromagnetic DMS exhibiting intrinsic ferromagnetism with Curie temperature (T_C) well above room temperature. The synthesis of one dimensional (1-d) DMS is expected to be attractive for the fabrication of low dimensional, spin-based electronic and optoelectronic devices. Transition metals with partially filled *d* states such as Sc, Ti, V, Cr, Mn, Fe, Co, Ni and Cu have been incorporated as magnetic atoms in DMS by researchers. The electron spin of the partially filled *d* states has been found to be responsible for the observed magnetic behavior in these DMS. Ferromagnetism has been predicted and confirmed in several nanocrystalline III-V group DMSs doped with transition metal (TM) ions such as Mn, Cr, V, and Co. However, III-V semiconductors require complex processing steps and are expensive to synthesize. Moreover, obtaining T_C above room temperature in III-V-based DMS poses a major challenge. In the quest for DMS with high T_C, TM doped ZnO, which is a II-VI semiconductor, has emerged as an attractive candidate as it is abundant in nature, non-toxic and inexpensive to synthesize. Subsequent to prediction of room temperature ferromagnetism (RTFM) in nanocrystalline ZnO and GaN containing small amounts of Mn (5%) and the same was confirmed in Mn-doped ZnO thin films, nanowires and ZnO nanoparticles. However, recent experimental reports indicate conflicting and inconsistent ferromagnetic properties in TM doped ZnO. There are also several controversial and conflicting proposals for the mechanism leading to RTFM in TM doped ZnO including clustering, segregated phases and defect mediated ferromagnetic coupling. Hence, the origin of experimentally observed ferromagnetism in TM doped II-VI semiconductors is still a matter of continuing debate.

Ferrites form a large class of oxides with remarkable magnetic properties, which have been investigated during the past several decades. The interest in them stems from their wide variety of applications such as millimeter wave integrated circuitry, power handling, permanent magnets and magnetic recording. Spinel ferrites possess the crystal structure of the natural spinel $MgAl_2O_4$. Among ferrites, calcium ferrite ($CaFe_2O_4$) stands out as a material of interest both from applications as well as basic scientific viewpoints. The main reason for this is $CaFe_2O_4$ can crystallize in orthorhombic structure unlike most other ferrites which crystallize in cubic spinel structure. Moreover, the large ionic radius of Ca forces it to be 8- or 9-fold coordinated in the $CaFe_2O_4$ structure. Ca–Fe–O is known for its application as oxidation catalysts, high-temperature sensors, gas absorbers, ceramic membranes and electrodes for solid oxide fuel cells. Evolution of spinel (cubic) and orthorhombic structures in nanocrystalline $CaFe_2O_4$ has not been carefully studied so far.

It is possible to obtain novel 1-d (undoped and TM doped) ZnO nanostructures by electrospinning route. Comparison of such novel structures with other nanostructures already reported in the literature might throw light on the mechanism behind RTFM in these nanostructures. Similarly, nanocrystalline $CaFe_2O_4$ with controlled cubic and orthorhombic crystal structures have not been systematically prepared and evaluated towards possible applications so far. With a motivation to address these issues, this thesis work has been devoted to the (i) preparation of poly vinyl alcohol (PVA) nanofibers containing zinc acetate using electrospining technique and understanding the evolution of nanocrystalline ZnO from the composite as a function of heat treatment temperature and the corresponding physical properties, (ii) preparation of PVA nanofibers containing Zn, Co and Mg salts using electrospining technique and understanding the evolution of nanocrystalline TM doped ZnO as a function of heat treatment temperature in these composites and the resulting physical properties, (iii) preparation of $CaFe_2O_4$ nanopowders by sol-gel route and monitoring the evolution of crystal structure as a function of heat treatment temperature and the corresponding structural and magnetic properties, (iv) preparation of $CaFe_2O_4$ nanopowders with Co substituted in Ca sites using sol-gel technique and observation of crystal structure evolution as a function of heat treatment temperature and the resulting structural and magnetic properties, and (v) preparation of PVA nanofibers containing Ca and Fe salts using electrospinning technique and understanding the evolution of nanocrystalline $CaFe_2O_4$ as a function of heat treatment temperature and the resulting structural and magnetic properties.

The work done for the PhD thesis is presented in six chapters. **Chapter 1** provides a brief introduction to the contents of the thesis. A review of the literature related to the materials of interest to the thesis work is also included in this chapter. **Chapter 2** discusses the experimental techniques employed in the investigations, including sample preparation procedures and experimental methodologies adopted. The principle and theory behind the experiments performed, the experimental set up used and the measurement procedures followed for determination of the physical properties are also discussed here.

In **Chapter 3**, the effect of annealing temperature (T_A) on the evolution of nanocrystalline microstructure and the resulting electronic, vibrational, magnetic and electron paramagnetic resonance (EPR) properties of as spun PVA/ZnO nanofibers prepared by electrospinning technique are reported. Heat treatment of as spun composite nanofibers results in single phase hexagonal wurtzite structure with the average crystallite size in the nanometer range. The average crystallite size and lattice constant were found to increases with increase in T_A. Raman spectra show the presence of the E_2(H) phonon mode characteristic of wurtzite ZnO and the E_1(LO) mode which is a signature of O-vacancy defects in the crystal. The decrease in the intensity and the broadening of the E_1(LO) peak with increasing T_A indicate a variation in defect concentration in ZnO with temperature. The average room temperature magnetization decreases with increasing T_A and attains a maximum value of 0.039 emu/g at 10 kOe for the PVA/ZnO nanofibers annealed at 500 °C. High temperature magnetization reveals a well-defined magnetic phase transition around 885 K due to the induced ferromagnetic phase. Steady state photoluminescence (PL) and EPR spectra confirm that large concentration of singly ionized oxygen vacancy present in the annealed samples are responsible for the observed RTFM in these the samples.

Chapter 4 reports the effect of annealing on Mg and Co substituted ZnO nanofibers. Mg doped inter-twined 1-d ZnO nanowires have been prepared by electrospinning metal oxide precursors and PVA followed by heat treatment. Annealed nanowires are crystalline with single hexagonal structure of ZnO for Mg doping up to 5 wt.% as revealed by X-ray diffraction (XRD) studies. The average crystallite size and lattice constant increase as Mg concentration is increased. Analysis of the blue-green PL band shows that the oxygen vacancies decrease upon Mg doping. Enhancement in band gap energy from 3.25 to 3.56 eV and a reduction in oxygen defects observed upon Mg^{2+} doping in ZnO nanowires might help in our tryst to develop wide bandgap optoelectronic

devices. Inter-twined Co doped ZnO nanowires were successfully prepared by electrospinning method followed by heat treatment at 550 °C. XRD analysis confirmed that Co^{2+} ions get incorporated in the lattice site of Zn^{2+} ions in the ZnO structure and annealed nanowires exhibit single phase (hexagonal wurtzite) structure of ZnO for Co doping up to 3 wt.%. On the other hand, Raman and EPR spectroscopy indicate the presence of Co_3O_4 phase in samples with more than 2 wt.% Co. Average crystallite size and microstrain decreased with increase in Co doping in ZnO nanowires. Enhancement in band gap energy from 3.29 to 3.38 eV is observed upon Co doping in ZnO nanowires. Samples were weakly ferromagnetic at room temperature with considerable paramagnetic component, but magnetization increased with increase in Co concentration in ZnO nanowires. The observed ferromagnetism in the Co doped ZnO nanowires can be attributed to exchange interaction between local spin-polarized electrons and conduction electrons of Co.

Chapter 5 discusses the formation of nanocrystalline cubic $CaFe_2O_4$ and $Ca_{1-x}Co_xFe_2O_4$ (x = 0.1) powders by sol-gel method and their transformation to orthorhombic phase upon annealing. Room temperature XRD patterns shows that as-synthesized cubic nanocrystalline $CaFe_2O_4$ powder transforms to orthorhombic phase when annealed above 400 °C. Annealing as-synthesized powder at 1100 °C yields single phase $CaFe_2O_4$ powder with orthorhombic structure. Cubic $CaFe_2O_4$ shows superparamagnetic behavior. Weak ferrimagnetic behaviour appears in the sample upon crystallization of the orthorhombic phase at temperatures above 400 °C with considerable reduction in magnetization. The orthorhombic phase exhibits antiferromagnetic to paramagnetic transition with T_N ~175 K. Temperature dependent Mössbauer spectroscopy confirmed the superparamagnetic behaviour of the spinel $CaFe_2O_4$ and the antiferromagnetic to paramagnetic transformation in orthorhombic $CaFe_2O_4$. In the case of $Co_{0.9}Ca_{0.1}Fe_2O_4$ powder, room temperature XRD patterns show that cubic nanocrystalline $CaFe_2O_4$ powder transforms to orthorhombic phase when annealed at 1100 °C. However, as T_A is increase beyond 500 °C, some extra peaks due to the Co precipitation are observed. The average crystallite size decreased with Co content as compared to $CaFe_2O_4$ powder. The sample also show ferromagnetic behavior with high saturation magnetization.

Chapter 6, presents the synthesis of PVA nanofibers containing Ca and Fe salts and the effect of annealing them at different temperatures up to 1000 °C. Room temperature XRD patterns indicate that as-spun cubic nanocrystalline $CaFe_2O_4$ transforms

to orthorhombic phase when annealed above 500 °C. Annealing as spun nanofibers at 1000 °C yielded single phase $CaFe_2O_4$ nanowires with orthorhombic structure. Cubic $CaFe_2O_4$ shows superparamagnetic behaviour and weak ferrimagnetic behaviour appears in the sample upon crystallization of the orthorhombic phase at temperatures above 500 °C. The orthorhombic phase exhibits ferromagnetic and paramagnetic contributions. Due to significant contribution to the magnetic anisotropy energy barrier by the L-S coupling at Ca^{2+} lattice sites, the blocking temperature (T_b) of $CaFe_2O_4$ nanoparticles shifts with change in average crystallite size.

Chapter 7 provides a summary of the results obtained in the thesis and suggests possible directions of future work.

References and publications which have originated out of this thesis work are listed at the end of the thesis.

CONTENTS

Chapter 1

INTRODUCTION

This chapter contains a review of the literature on the dilute magnetic semiconductor and ferrites. The focus of this work is also outlined.

Low dimensional materials which have at least one of the dimensions in the range of 2 to 100 nm exhibit several new properties hitherto unknown in their bulk counterparts [ROSA15]. The fact that many of these properties are strongly influenced by the nanometric size as well as the dimensionality of the nanoparticle has enthused researchers to explore these properties more with the hope to find new applications for these materials. New magnetic phenomena observed in nanodots, nanowires, thin films, and multilayers and macroscopic heterogeneous materials that contain nanoscopic particles have thus opened up the new field of nanomagnetism [BINN14]. Applications of nanomagnetism range from spintronics (in which information is manipulated, stored and transferred using electron spins), ultra-high density magnetic storage media and read-heads to biosensors as well as medical applications such as targeted drug delivery and cancer therapy [ROSA15]. Spintronics exploits both the intrinsic spin of the electron and its associated magnetic moment in addition to its electronic charge. Researchers are now focusing on using the spin degree of freedom of the electron for newer device performance using such spintronic materials [SCHU05, MACD05, PICO04, DIET03, ZUTI04]. In particular, spintronics based diluted magnetic semiconductors (DMS) provide a new technology that transforms data reading and writing methodology from electronic charge domain to electron spin domain. Significant research is now being performed on DMS obtained by inducing ferromagnetism in non-magnetic semiconductors by doping dilute concentrations of magnetic elements [DIET14, ZHAN13, FENG13, DIET10, YANG14]. Despite a large amount of work already done, further research is actively being pursued in this topic to find out better materials from application and viability viewpoints. The main motive behind this thrust is that the manipulation of the electron spin in semiconducting devices will improve the conventional semiconductor technology since there are four degrees of freedom [FPAN08, PEAR07]. Hence, it has been suggested that DMS could effectively serve as building blocks for technologies like non-volatile memory devices with increased data processing speed and decreased power consumption [SAWO01, DDAW07, SDAS03, FMAT14, SHE012, HOHN10].

Magnetic data storage devices mainly depend on the technological skill to produce device structures of lower dimensions and sizes without losing stability and lifetime of the stored data. So, to improve the functionality of electronic devices, spin functionality of the carries need to be explored. The general ambition is to use spintronic materials and devices at ambient temperature. To achieve this, the primary aim in the research of DMS materials, is to develop ferromagnetic (FM) semiconductors with Curie temperature (T_C) well above room temperature. Several DMS materials with high T_C have been predicted such as Mn-doped

GaN [ABON07], Co-doped TiO_2 as well as TM doped ZnO [PEAR07, NORB04, KITT05]. Subsequently, many excellent findings leading to different spintronic applications have been reported [GHOS13, NHOA13, WALS08, CHEN12, QLI012, CLAU07, MOHA14, CHAM09, CHEN08, HASS11]. Although many experimental reports on DMS materials exist, they mostly report low T_C, low magnetization or even absence of magnetic ordering [PANI08, KASP08, COEY08a, YPAN06]. In reality, research on DMS faces considerable challenges related to uniformity of dopant incorporation, secondary FM phases, contamination issues, etc [KASP08, WANG08a, ANEY10]. The large difference in the T_C reported by different experimental groups due to difficulties incurred during sample preparation is another teething issue. Hence, optimization of preparation and growth conditions are important to observe strong FM behaviour in DMS materials, Doping (n- or p-type) is used to produce indirect carrier mediated FM interaction or controlled growth of defects (vacancy, interstitials) for defect mediated FM interaction in DMS material [CHAN11, KATA13, NAEE12]. Defect states introduced by growth methods and conditions have direct influence on the analysis of magnetization results, as they can either directly contribute to the magnetization or indirectly through the exchange mechanism [DEBE11, PATT06, GHOS13]. The defect-related magnetism in DMS materials has made the field popular [PDEV10, CHAK11, LHU013]. Despite the enormous interest, it is still not fully clear whether the observed magnetism in DMS is due to the intrinsic/extrinsic defects or due to the dopant atoms.

1.1. Potential DMS materials

In the beginning, research on DMS was confined to doping of III-V or II-VI semiconductors, where the host lattice was wurtzite or zinc-blende type structure and the dopants were transition metal (TM) elements such as Cr, Mn, Fe, Co and Ni. In general, the magnetic (3d) ions in DMS materials are located at substitutional or interstitial sites of the host [OHNO96, OLEJ08, DIET00]. It took several years to develop appropriate materials which could be applicable in technology development [CHEN13, WANG08, KUDR04]. Great progress was achieved when spin dependent devices based on (Ga, Mn)As were discovered [OHYA10, OHNO00]. Although T_C of (Ga,Mn)As could be raised up to 190 K, researchers are not hopeful of achieving higher T_C [HASS11, WANG13]. In order to find a correlation between FM and semiconducting properties, the predicted T_C [PEAR03] of several promising semiconductors is plotted as a function of their bandgap in Figure 1.1.

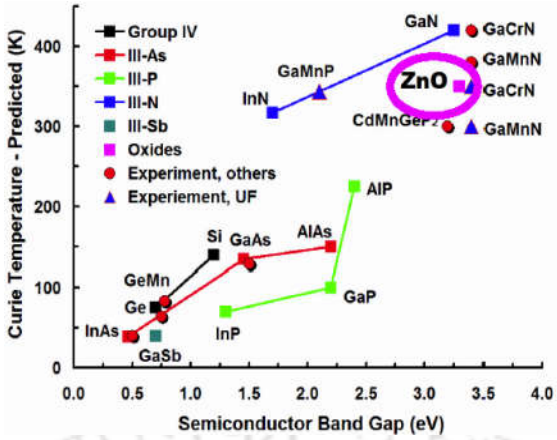

Figure 1.1: Predicted T_C of prospective semiconductors as a function of bandgap [PEAR03].

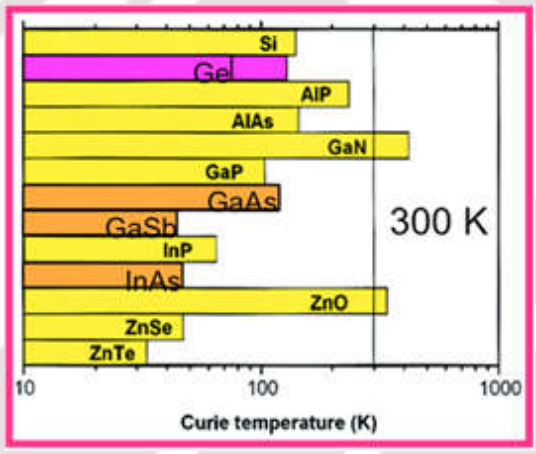

Figure 1.2: Curie temperatures evaluated for various group IV semiconductors and III-V and II-VI semiconducting compounds containing 5% of Mn per cation [DIET00].

Lately, DMS based on II-IV metal oxide wide band gap semiconductors, such as ZnO, TiO_2, SnO_2, In_2O_3 and $(In,Sn)_2O_3$ have attracted considerable attention due to their promise as high temperature FM materials. Oxides differ in many ways from the conventional elemental and compound semiconductors [JANO07, DIEB03, SANG14]. So, researchers have attempted to dope several elements in oxide semiconductor to enhance their property. In this regard, doping of magnetic TM elements provides exciting possibilities. Most extensive research in this field has been done on two wide band gap functional metal oxides, viz., ZnO and TiO_2. Initially, the work of Matsumoto et al. [MATS01] on the observation of ferromagnetism in Co doped TiO_2, and the subsequent work on Mn doped ZnO motivated the researcher to explore oxide DMS more closely [DIET01, FUKU99]. Another motivating fact

is a larger (~35%) concentration of TM ions can be substituted in the semiconducting lattice of II-VI semiconductors as compared to ~8% for III-V semiconductors [KNUT10]. T_C evaluated for various III-V as well group IV and II-VI semiconducting compounds containing 5% of Mn per cation is displayed in the bar chart in Figure 1.2 [DIET00].

1.2. ZnO based DMS

ZnO is a II–VI compound semiconductor with a direct wide bandgap (3.37 eV at room temperature), large excitonic binding energy (60 meV) and excellent optoelectronic properties [WANG08a, JANO09]. ZnO crystallizes in the hexagonal wurtzite structure with lattice constants, a = 3.25 Å and c = 5.12 Å. ZnO is an inherently n-type semiconductor but p-type conductivity can also be induced in it by appropriate doping [JANO09]. ZnO exhibits high photoconductivity and considerable piezoelectric response [WANG06]. The coexistence of magnetic, electric, and optical properties increases the scope for TM-doped ZnO to be a multifunctional material. ZnO-based DMS have been studied after the theoretical prediction of Dietl on Mn doped p-type ZnO [DIET03] and Sato and Katayama-Yoshida's [SATO00] first-principles calculations on doping of 3d TM ions (like V, Cr, Fe, Co and Ni), which revealed room temperature FM ordering [DIET01, KATY02]. After these theoretical prediction, experimental confirmations appeared on ZnO doped with a wide range of TM ions such as Mn, Co, Ni, Fe, V, Cr, Al, Cu, etc.[PANI12, CHIK13, SCHW04, BAIK05, SRIN13] for both hole [NORB04, KITT05] and electron-mediated [SCHW04, VENK04] ferromagnetism in ZnO.

TM-doped ZnO compounds are being synthesized and fabricated in the form of nanostructures or thin films by a wide variety of physical and chemical routes like pulsed laser deposition (PLD) [XLIU06], molecular beam epitaxy (MBE) [OPEL12], magnetron sputtering [TFLI07], chemical vapor deposition (CVD) [ZUKO06], co-precipitation method [DGAO09], solvo-thermal reaction [BPAL14], sol-gel method [HAYS07] electrospinning [ARNA16], etc. Though, there is no conclusive understanding on the origin of magnetic interaction in most of the cases [AVRU10], the literature is abound with debates and possibilities. High surface-to-volume ratio associated with nanomaterials may also influence the properties of TM-doped ZnO DMS. Sanchez et al. [SANC08] reported that uncompensated surface spins enhances the spin polarization induced by substituted Co ions and produces RTFM even in the absence of magnetic ions. Recently, Peng et al. [PENG09] predicted an enhancement of hole-mediated magnetization due to the size effect in

nanomaterials. These reports indicate that ZnO nanostructures have the potential to be promising DMS.

In recent years, extensive experimental and computational research is underway on undoped or non-TM doped oxide systems as alternatives to achieve FM semiconductors [RUBI07]. Since the undoped or non-TM doped oxides do not contain ions with partially filled d or f bands, this type of ferromagnetism in undoped oxides is referred to as 'd_0 ferromagnetism'[COEY10, COEY08]. In addition, observation of room temperature ferromagnetism (RTFM) in nonmagnetic ion doped [HERN10, HJXU10] and undoped ZnO [SUND09, PANI10] indicates that magnetic properties are not exclusively related to the presence of the magnetic ions but rather strongly mediated by point defects, such as oxygen vacancy (V_o), zinc vacancy (V_{Zn}) and interstitial zinc (Zn_i) [PANI10, KHAL09]. Defect related FM moment in undoped nanostructures is of much lower magnitude (10^{-3} emu/g) as compared to doped DMS (~0.04 emu/g) [HAYS07]. This 'd_0 ferromagnetism' is often observed only in thin films and nanostructures having high surface to volume ratio and strong surface effects [DENG10]. Hence, it is imperative to clarify the origin of defects and the coupling mechanism behind RTFM in undoped ZnO.

1.2.1. Crystal structure of ZnO

Most of the II-VI binary compound semiconductors crystallize in either zinc blende or hexagonal wurtzite structure. ZnO can crystallize in three different structures, viz., wurtzite (B4), zinc blende (B3) and rock salt (B1) as demonstrated in Figure 1.3. Among these, the wurtzite structure is the thermodynamically stable structure at ambient conditions, while zinc blende structure is stabilized only by growth on cubic structures and rock salt structure can be obtained at high pressures [OZGU05].

The wurtzite structure has a hexagonal unit cell with lattice parameters, $a = b = 3.250$ Å and $c = 5.206$ Å [ABRA69]. It belongs to P63mc space group with Zn atoms occupying the (0.667, 0.333, 0.000) position having a multiplicity factor of 2 and oxygen atom occupying the (0.667, 0.333, 0.380) site with multiplicity factor 2. Thus, there are two formula units per unit cell as shown in Figure 1.4. In both the cases, Zn and O atoms have tetrahedral co-ordination.

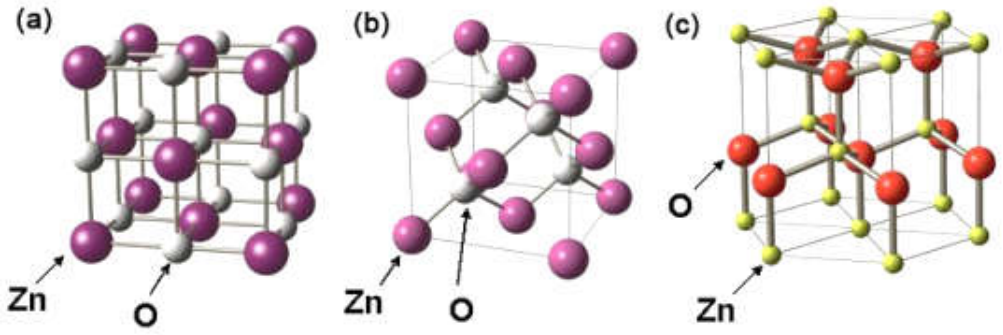

Figure 1.3: ZnO crystal structures: (a) rock salt (B1), (b) zinc blende (B3) and (c) wurtzite (B4).

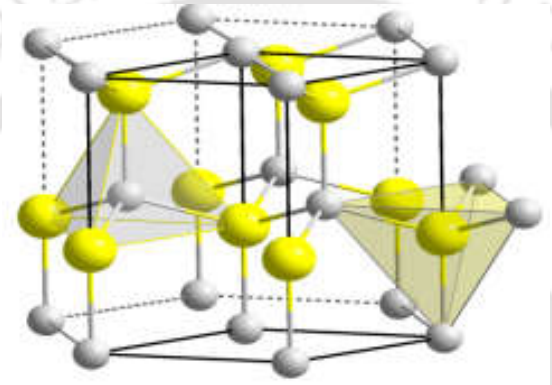

Figure 1.4: Hexagonal wurtzite structure.

1.2.2. Defects in ZnO nanostructures

Intrinsic defects: Depending on the preparation technique, certain intrinsic defects are observed in ZnO nanowire structures which influence the band edge ultra violet (UV) emission. These intrinsic defects have strong spectroscopic effect in photoluminescence (PL) spectrum. Lin et al [BLIN01] and Djurisic [DJUR07] identified oxygen and zinc related intrinsic defects and some other related defects through PL spectroscopy. Liu et al. [JLIU09] demonstrated that PL from ZnO nanowires can be tuned from UV to green by controlling the native defects either by oxygen gas flow during growth process or by post-growth annealing in oxygen environment. Some reports show that the most commonly observed green emission is caused by the presence of Zn vacancy [KOHA00, JANO07]. In contrast, other groups have claimed that it is not due to Zn vacancy, but due to oxygen vacancy [VANH96, BLIN01]. Therefore, a systematic generalized correlation of the defects and the corresponding emission needs to be done. First–principles calculations on ZnO nanostructures [JANO09] show the

possible formation of six types of native point defects in ZnO, viz., oxygen and zinc vacancies (V_O and V_{Zn}), interstitials (O_i and Zn_i), and antisites (O_{Zn} and Zn_O). The calculations show that there is also a possibility of formation of three types of oxygen vacancy defects according to their charge states, viz., neutral (V_O^0), singly ionized (V_O^+) and doubly ionized (V_O^{++}). The atomic configurations of the various point defects in the ZnO crystal are shown in Figure 1.5.

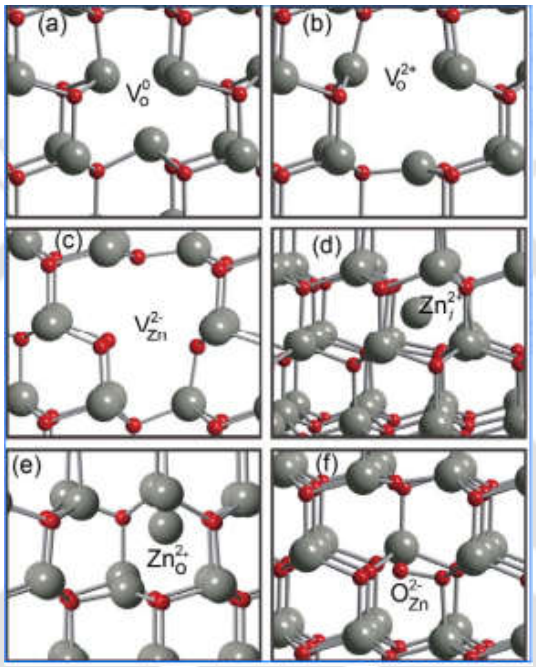

Figure 1.5: Several point defects calculated from first-principal calculation [JANO07].

Moreover, the calculations also show that oxygen vacancies are deep donors and zinc vacancies are deep acceptors under n-type conditions. Zinc interstitials are shallow donors but have high formation energy. On the other hand, zinc antisites are also shallow donors but with higher formation energy. Oxygen antisites have the highest formation energy among the acceptor type defects and they are also deep donors. Oxygen interstitials have high formation energy and are expected to exist in significant concentrations.

Extrinsic defects: Undoped ZnO is an n-type semiconductor with carrier concentration ~10^{17} cm^{-3} [BETH88]. However, it is not suited for practical application purpose where higher carrier concentration is required. Therefore, doping of group III and V elements in ZnO nanostructure is essential to increase the carrier concentrations required for applications [CHHS10, CXU005]. When a large amount of the dopant element is added in ZnO, there is possibility of formation of either a mixed oxide or a second phase depending on the solubility

limit of the dopant in the compound. Also, formation of mixed oxide and clusters cannot be ruled out. The distribution of the dopant in the crystallites/grains of the matrix material can be homogeneous or heterogeneous. Doping helps to increase or decrease the band gap of the ZnO nanostructure by introducing the defect states as either donor or accepter level, depending on the dopant element. Introducing a dilute amount of cation (TM ion) in ZnO can lead to RTFM [BELG06]. But there is considerable debate on whether the ferromagnetism in TM doped ZnO is due to the TM cluster, or segregation of secondary magnetic phases [SHIN04, COEY05] or solely related to its intrinsic nature [RAMA06]. Since the nature of the individual dopant as well as its concentration and distribution determine the defect structure of the crystal, it is also bound to influence the electronic and optical properties of the resulting ZnO crystal.

1.2.3. Optical properties of ZnO

In all semiconductors, the band gap transition can be facilitated by illumination with light, i.e., these materials can be photo-activated, since the band gap energy falls within the optical electromagnetic spectrum energy. Upon illumination of light, the electrons are excited from valence band to conduction band, resulting in resonance absorption of light at a particular wavelength λ_g. There are two types of band gap transition in semiconductors, viz., (i) direct band gap and (ii) indirect band gap transition. A semiconductor in which the bottom of the conduction band and the top of the valence band are placed at a common wave vector, **k**, is a direct transition semiconductor, as shown in Figure 1.6. In this transition, energy and momentum are conserved. Therefore, the phonons do not take part in direct transitions. On the other hand, a semiconductor with the bottom of the conduction band and the top of the valence band having different **k** values is an indirect transition semiconductor. In this case, the electronic transition from valance band to conduction band is electrically dipole forbidden and the transition is phonon assisted. Hence, both energy and momentum of the created electron-hole pair change in this transition. Therefore, absorption and emission of light are weaker in indirect semiconductors as compared to direct band gap semiconductors. The relation between band gap energy (E_g) and absorption coefficient (α) of optical absorption is given by the equation [BARD54],

$$\alpha h\nu = A(h\nu - E_g)^{\gamma} \qquad (1.1)$$

where A is a constant, γ a value representing the optical transition mode and $h\nu$ is the photon energy (in eV). γ depends on the optical transition mode and takes the values 1/2, 3/2, 2 and 3

for direct allowed, direct forbidden, indirect allowed and indirect forbidden transitions, respectively. Fitting the experimental absorption data with correct choice of γ reveals the band gap and the nature of transition. From the optical absorption spectra, the band gap can be calculated by extrapolating the tangent of $(\alpha h\nu)^{1/2}$ versus $h\nu$ plot to $(\alpha h\nu)^{1/2} = 0$ for indirect allowed band gap and $(\alpha h\nu)^2$ versus $h\nu$ plot to $(\alpha h\nu)^2 = 0$ versus $h\upsilon$ plot to for direct allowed band gap. This plot is known as Tauc's plot [TAUC66]. Though bulk ZnO has a direct bandgap of ~3.37 eV at room temperature, bandgap shows a blue shift for ZnO nanoparticles [BHAT08].

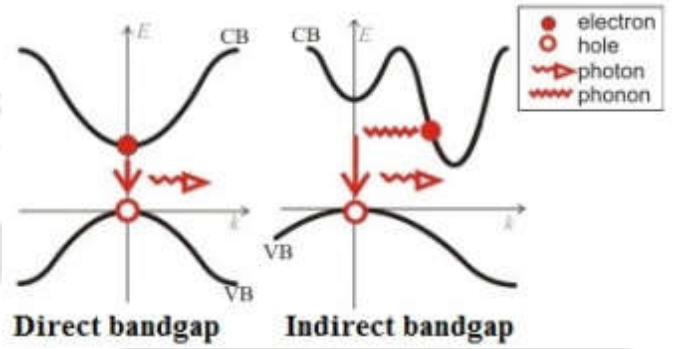

Figure 1.6: Direct and indirect transition semiconductors.

Raman scattering is an effective tool for studying the nature of crystallinity and defect states in the crystal structure of materials. In the hexagonal wurtzite ZnO, the number of atoms per unit cell is 4 and there are a total of 12 phonon modes present [STRO01]. One longitudinal-acoustic (LA), two transverse-acoustic (TA), three longitudinal-optical (LO), and six transverse-optical (TO) branches. Raman spectroscopies have been commonly used to derive zone-center and some zone-boundary phonon modes in ZnO. We know that ZnO crystallizes in hexagonal wurtzite structure with 2 formula units in the primitive cell. The optical phonons at the Brillouin zone belong to the following representation. The A_1 and E_1 branches are Raman active, the two nonpolar E_2 branches are Raman active only, and the B_1 branches are inactive (silent modes) [MEAD77]. The A_1 and E_1 modes are each split into LO and TO components with different frequencies due to the macroscopic electric fields associated with the LO phonons [OZGU05]. The low-frequency E_2 mode is associated with the vibration of the heavy Zn sublattice, while the high-frequency E_2 mode involves only the oxygen atoms. The complete set of phonon mode frequencies has been measured using Raman spectroscopy for ZnO in both bulk and thin film forms [DAME66, YFLU00]. Ashkenov et al. [ASHK03] observed no significant differences in the E_1 (TO), A_1 (TO), and

E_2 mode frequencies of bulk and pulsed-laser deposited ZnO thin film. A small redshift was observed in longitudinal-optical-phonon mode frequencies of ZnO films with respect to the bulk ZnO, which can be attributed to existence of vacancy point defects within the film [ASHK03]. Figure 1.7 illustrates the Raman spectra of bulk and thin film ZnO.

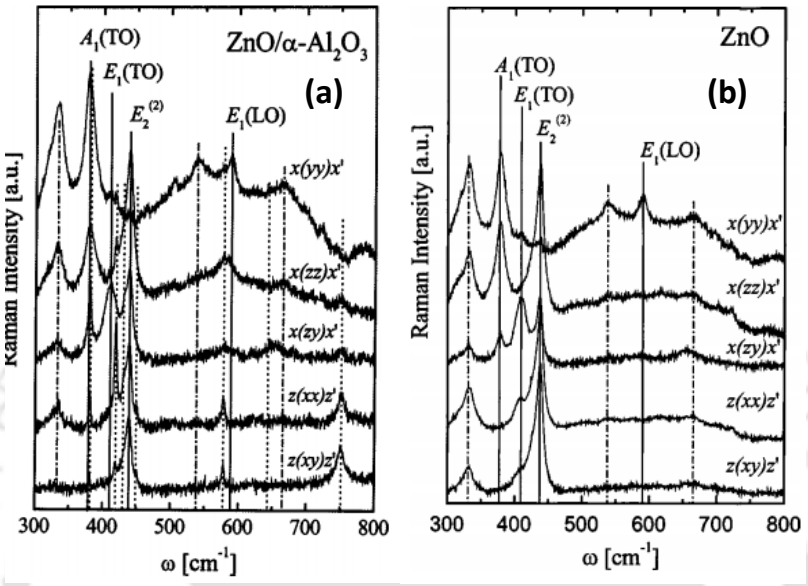

Figure 1.7: (a) Raman spectra of (a) bulk and (b) thin film ZnO [ASHK03].

The solid vertical lines in Figure 1.7 (a) and (b) indicate E_1, A_1, and E_2 phonon modes of ZnO. The dashed-dotted lines mark features observed at 332, 541, and 665 cm^{-1} which were assigned to possible multiple phonon scattering processes [DAME66, CALL77]. The dotted lines are related to the sapphire phonon mode frequencies (A_{1g} mode: 417 and 645 cm^{-1}; E_g mode: 379, 430, 450, 578, and 751 cm^{-1}) [PORT67]. A_1(LO) was observed in both samples because the scattering cross section for this mode is smaller than that of the A_1(TO). Some researchers have reported additional Raman peaks at 205, 331, and 539 cm^{-1} in their ZnO nanostructure [RAJA00]. Similar peaks at 208, 332, and 541 cm^{-1} are also reported for bulk ZnO. In both cases, these peaks have been assigned to the second-order Raman spectrum arising from zone-boundary.

1.2.4. Magnetic properties of ZnO

As mentioned earlier, RTFM in Mn doped ZnO [DIET00] has initiated immense interest in ZnO nanoparticles specially since its origin is still not fully understood. Several models and mechanisms have been proposed to explain the magnetism in DMS materials. RTFM could arise from a number of possibilities such as the intrinsic property of the doped DMS host

matrix, extended defects in the ZnO nanomaterials, formation of some nanoscale TM-related secondary phases etc. Some of the widely reported FM interactions are based on Zener model, RKKY model, Dietl's application of the Zener model, the approach of additional (electron/hole) doping, and first-principles calculations. There are two interacting subsystems in DMS: the delocalized conduction band electrons, valance band holes and the diluted system of localized magnetic moments associated with the TM ions. FM interaction couples the spins of s-like electrons or p-like holes near the band edges to the d-shell spins of the TM ions. The incorporation of the TM atoms or ions into the ZnO host lattice involves either replacement of cationic ions on regular host sites or positioning them on interstitial sites. The magnetic properties of the final system depend on many more parameters including the concentration and distribution of the TM ions, type and concentration of defects, n-type doping, p-type doping, etc.

The Zener model is the first model proposed, where exchange interactions between carriers and localized spins (s–d interaction) is considered [ZENE51]. Later Dietl et al. [DIET03] have used the Zener description to realize possible origin of RTFM as hole-mediated exchange interactions and theoretically predicted a T_C value above room temperature in p-type ZnO with 5% Mn atoms [DIET00]. After analyzing the density of states, Sato et al [SATO01] proposed that the FM state is stabilized by additional electron doping in the case of Fe, Co and Ni doped ZnO. According to this model, there is an exchange interaction between the charge carriers introduced in the ZnO host through specific point defects or additional doping and magnetic cations. Higher concentration of TM ions as well as higher concentration of electron dopants lead to higher stabilization of FM as a ground state. Lee and Chang [CLEE04] have investigated the magnetic interactions between the Co ions, considering different geometries of Co ion sitting on Zn regular sites in a ZnO supercell [ECLE04]. The difference originates from the hexagonal symmetry of the wurtzite structure. Sluiter et al. [SLUI05] have developed a simple and general picture about the trends of magnetic interactions for the TM series in DMS. According to their prediction, long-range interaction is necessary for FM interaction in Co substituted ZnO DMS and it can be mediated by defect induced states. Moreover, both hole and electron doping promote FM in Co-doped ZnO, which is advantageous as compared to the previous report of Sato et al., [SATO01] where only electron doping could enhance FM interaction in TM-doped ZnO.

The surface-to-volume ratio is high in nanostructures in comparison with the corresponding bulk material, and therefore surface effects become more pronounced with

decrease in particle size. Sanchez et al. [SANC08] investigated the local magnetic order at the surface of ZnO using first principles calculations. They showed that uncompensated surface spins play a crucial role on the saturation magnetization. The surface enhances the spin polarization induced by Co atoms, thereby resulting in magnetic behavior which is missing in the bulk [SANC08]. Hence in nanostructured DMS, the surface may show uncompensated spins which is ferromagnetically ordered [DENG10]. Furthermore, there exists a controversy whether the ferromagnetism observed in oxide DMS is related to intrinsic defects or 'd_0 ferromagnetism' [COEY08]. In addition, some reports of RTFM on nonmagnetic element doped [HERN10] and undoped oxide such as ZnO, TiO_2, MgO, CeO_2, etc., [SUND09, PANI10] indicate that in specific cases the magnetic properties may be not exclusively related to the presence of the magnetic ions but could be strongly mediated by point defects such as O_v, Zn_v, or Zn_i) [PANI10, KHAL09]. However, it is very difficult to establish a direct link between the magnetization and defects due to complexity of defect states in ZnO. This only shows that the nature of d_0 FM in undoped systems needs further investigations to resolve this issue.

The role of defects (vacancy, interstitial, grain boundary defects) in the origin of FM interaction for the DMS oxides has been explained in Coey's model [COEY05]. Long-range interaction is necessary to obtain RTFM in small concentration of Co doped ZnO DMS which can be mediated by defect induced states [SLUI05]. According to the bound magnetic polaron (BMP) model, bound electrons (or holes) in the defect states can couple with TM ions and cause the FM regions to overlap, giving rise to long range FM ordering [COEY05]. When donors or acceptors are present, the sp-d exchange interaction often leads to the formation of BMPs. The BMP consists of the bound electron (hole) together with the spins of the TM ions within a hydrogenic Bohr orbit of radius r_H (= 0.76 nm for ZnO). Due to the sp-d interaction, the latter spins can have a significant net FM alignment. In this case, the BMP resembles a 'FM ball' embedded in the host lattice doped with TM ions that surround it [MCCA97]. According to Sarma [CALD07], a combination of percolation of magnetic polarons at lower temperature and carrier mediated ferromagnetism at higher temperature may be the reason for the very high T_C obtained in oxide DMS [CALD07]. A schematic diagram of magnetic polaron is shown in Figure 1.8.

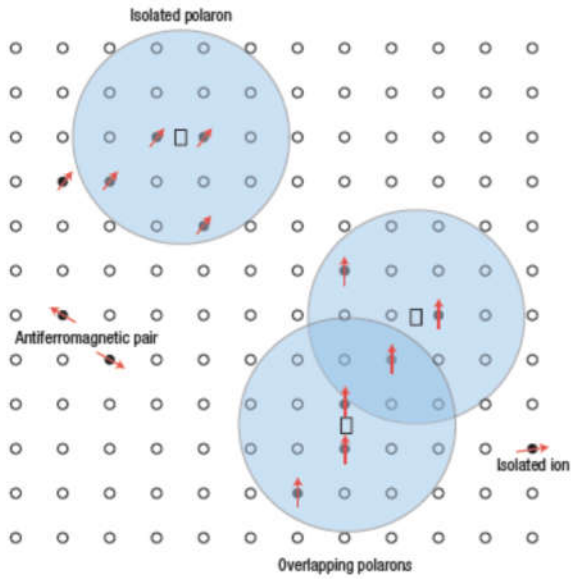

Figure 1.8: Representation of magnetic polarons. Open circles represent cation sites and squares denote unoccupied oxygen sites (oxygen sites are not shown) [COEY05].

1.2.5. Some applications of nanostructured ZnO

The concept of spin transistors (SFET) was first proposed by Datta and Das [DATT90] which motivated others to study such novel spin-controlled electronic devices. The advantage of the Datta-Das SFET is that spin-dependent device operation is controlled not only by external magnetic fields, but also by external electric field. Later, on Huang et al. [HUAN07] have demonstrated a silicon spin-FET in which spin polarized electrons are controlled by external gate voltage with 37% electron current spin. Spin based FET structure on III-V group based DMS have also been attempted [CIOR09]. However, no spin-FET based on FM oxide semiconductor has been experimentally developed yet. Using lithographic patterning technique, top gate electrode based ZnO nanowire FET (or MOSFET) was demonstrated by Heo et al [YWHE04] which is shown in Figure 1.9.

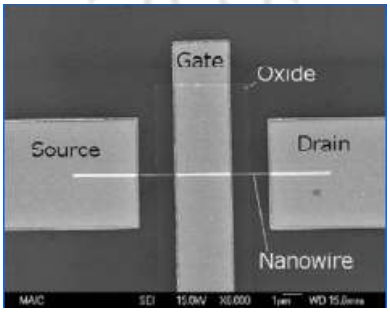

Figure 1.9: SEM image of a ZnO single nanowire based FET [YWHE04]

ZnO nanostructures have been widely used for sensing applications because of their high sensitivity to the chemical environment. Nanostructures have the advantage of a high surface area and electronic processes are strongly influenced by surface processes. ZnO nanowires have demonstrated high sensitivity even at room temperature The sensing process is done by oxygen vacancies on the surface that influence the electronic properties of ZnO. Upon oxidation or adsorption of molecules such as NO_2 at vacancy sites, electrons are withdrawn and effectively depleted from the conduction band which helps to reduce the conductivity. A ZnO nanorod sensor of H_2 gas has been developed [WANG05]. The sensitivity of this sensor was improved by sputter deposition of Pd clusters on the ZnO nanorod surface. The sensor detects hydrogen concentrations down to 10 ppm in N_2 at room temperature, whereas there is no response to O_2. The same group have also shown H_2 sensitivity for Pt-coated ZnO nanorods [TIEN05]. A different group used a thick film of ZnO nanoparticles for H_2 sensing [ROUT06]. A sensitivity of 10-1000 ppm H_2 was achieved for a Pt-impregnated, 3% Co-doped ZnO nanoparticle film at a working temperature of 125 °C or lower.

ZnO nanostructures show lasing action based on exciton recombination (~ 60 meV) at room temperature. Bao et al [JBAO06] have constructed a single nanowire light-emitting diode. A ZnO homojunction light-emitting diode (LED) has been fabricated on a single-crystal GaAs substrate by ultrasonic-assisted spray pyrolysis [GTDU06]. Lasing has been observed by different groups in ZnO nanowire arrays grown by a variety of methods. Huang et al. [HUAN01] have used nanowires grown by CVD on sapphire and shown a threshold of 40 kW/cm^2 under optical excitation. Lasing action has been observed in solution-grown ZnO nanorod arrays on F-doped SnO_2 glass substrates [GOVE02]. The observed UV-lasing efficiency is similar to that reported for nanowire arrays grown on Al_2O_3 substrates in a high temperature process.

ZnO has been used in dye-sensitized solar cells (DSSC) as an electrode material [BEDI97, KEIS02]. Investigations of nanoporous dye-sensitized ZnO films show that ultrafast electron injection from the dye into the conduction band of ZnO particles takes place [KATO04, FURU03]. DSSC usually have an electrolyte (redox system) to regenerate the dye by donating electron to its ground state after excitation. Recently, solid organic hole-transporter material has been replaced with the liquid electrolyte [BACH98]. Compared to fully organic solar cells, nanostructured hybrid solar cells have the advantage that the morphology of the film can be controlled by growth of ZnO nanostructure. Recently, poly(3-

hexylthiophene) has been used as a hole transporter in combination with ZnO nanostructures. These devices have an efficiency of ~0.5% under standard solar conditions [OLSO06]. Ravirajan et al. [RAVI06] have systematically investigated the influence of various ZnO nanostructures on the device performance. They compared flat ZnO layers, ZnO nanoporous layers, and vertically aligned nanowires in this study. The charge recombination time in the vertically aligned ZnO nanorods is very slow and gives a half-life of several milliseconds which is over two orders of magnitude lower than that for nanoparticles which is advantageous for solar cell applications. These investigations suggest that nanowire structures will further enhance the performance of hybrid solar cells in the future.

1.3. Classification of ferrites and their structures

Magnetic materials are widely used in different technological applications like, power generation, communication, data storage and retrieval, sensors etc. Researchers have devoted themselves to discover many novel magnetic materials to serve as alternatives to the existing materials with reduced cost and enhanced properties. Among them, ferrites form an important class of materials for their wide use in various applications. Ferrites are basically FM materials composed of iron oxide as their main constituent along with other metal oxides. Depending upon the crystal structure, ferrites can be classified into (a) spinel ferrites (b) garnets (c) ortho-ferrites and (d) hexagonal ferrites.

1.3.1. Spinel ferrites

Spinel ferrites are described by the chemical formula MFe_2O_4 where M stands for divalent cations such as Zn^{2+}, Co^{2+}, Fe^{2+}, Ni^{2+}, Cu^{2+} or Mn^{2+}. The Fe^{3+} ions can also be replaced by other trivalent ions like Al^{3+}, Cr^{3+}, Ga^{3+}, etc. Spinel ferrites are generally ferrimagnetic in nature. The crystal structure of the spinel ferrite contains two types of lattice sites, viz., tetrahedral sites (with four oxygen neighbours, known as A sites) and octahedral sites (with six oxygen neighbors, known as B sites). There are twice as many B sites as A sites. The two sublattices are non-equivalent because of the presence of two types of crystallographic sites and they contain two types of different ions. In a normal spinel, the cations sit at the A sites and the Fe^{3+} ($^6S_{5/2}$) cations sit at the B sites. Most of the spinel ferrites crystallize in cubic $MgAl_2O_4$-type structure, which is shown in Figure 1.10. The relatively large oxygen ions form a face centered cubic lattice in which there are 32 octahedral sites and 64 tetrahedral sites. In spinel structure, only 8 of the tetrahedral sites and 16 of the octahedral sites are occupied by the metal ions [BLUN03].

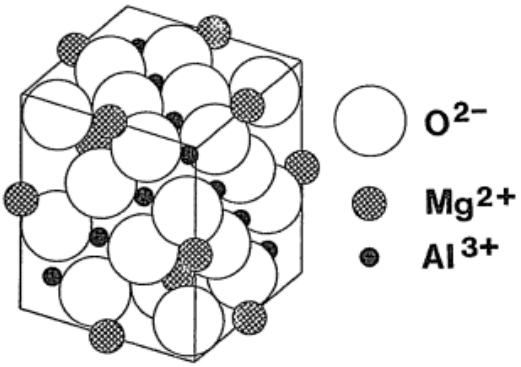

Figure 1.10: Typical spinel structure with unit cell of $MgAl_2O_4$ as example [KITT05].

In an inverse spinel, the M^{2+} cations sit at half of the B sites, while the Fe^{3+} cations occupy the other half of the B sites and all the A sites. In inverse spinel, the moments of the Fe^{3+} cations on the A and the B sites are antiparallel, so that the total moment of the sample is due to the M^{2+} ions only. The crystal structure of inverse spinel is shown in Figure 1.11, where 8 of the octahedral B sites are occupied by M^{2+} ions and 8 of the octahedral and 8 of the tetrahedral sites are occupied by the Fe^{3+} ions.

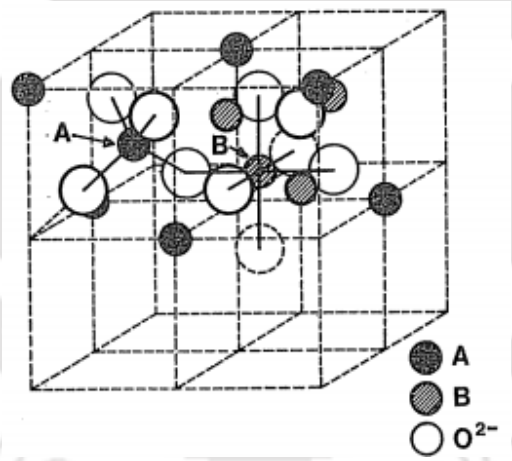

Figure 1.11: Typical unit cell of an inverse spinel ferrite.

Magnetic structures of normal and inverse spinel ferrites are shown in Figure 1.12. In the case of $MnFe_2O_4$ which has normal spinel structure, Mn^{2+} and Fe^{3+} ions have moment of $5\mu_B$ each. So, the net magnetic moment of normal $MnFe_2O_4$ is due to 8 uncompensated Fe^{3+} ions on the octahedral sites. However, in $NiFe_2O_4$ which is known to be an inverse spinel, the observed moment is due to the uncompensated magnetic moments of the 8 Ni^{2+} ions on the octahedral sites.

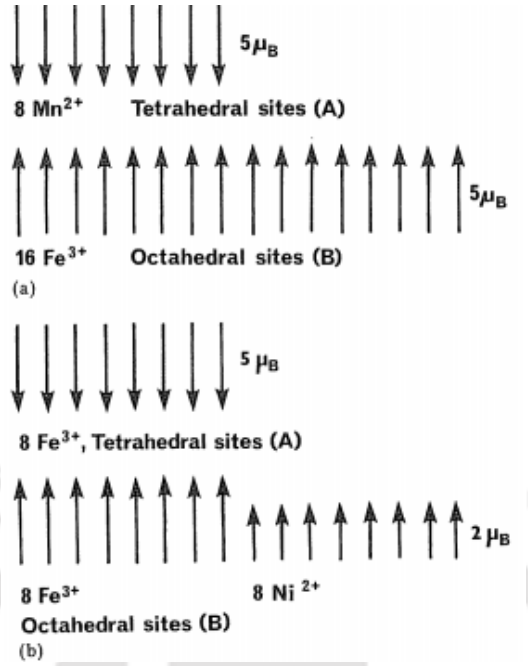

Figure 1.12: Magnetic structures of (a) normal spinel ($MnFe_2O_4$) and (b) inverse spinel ($NiFe_2O_4$) ferrites [MCCU94].

1.3.2. Garnets

Garnets form another family of ferrimagnets which have the chemical formula $R_3Fe_5O_{12}$ where R is a trivalent rare earth atom. Their crystal structure is also cubic and the unit cell contains 8 molecules of $R_3Fe_5O_{12}$ i.e. (160 atoms) [BLUN03]. The metal ions are distributed over three types of sites. The R ions occupy the dodecahedral sites (also called c sites), where they are surrounded by 8 oxygen ions and the Fe^{3+} ions are distributed over the tetrahedral and octahedral sites in the ratio 3:2. In yttrium iron garnet ($Y_3Fe_5O_{12}$), Y^{3+} has no magnetic moment (it is 4d° element) and the moments of the Fe^{3+} ions at the tetrahedral sites are antiparallel to those at the octahedral sites. So, the net moment of $Y_3Fe_5O_{12}$ is $5\mu_B$.

1.3.3. Ortho-ferrites

Ortho-ferrites have the general formula $MeFeO_3$, where, Me is a large trivalent metal ion, such as rare-earth ion or Y. They crystallize in a distorted perovskite structure with an orthorhombic unit cell. These ortho-ferrites show a weak ferromagnetism, which has been attributed to the small canting in the alignment of two antiferromagnetically coupled lattices. The direction of spin orientation of the Fe ion in $HoFeO_3$ and $ErFeO_3$ has been experimentally determined [HANE87] at room temperature and found to be parallel to the (100) axis. On lowering the temperature, the spin axis rotates such that at 1.25 K the direction

is (001) for $HoFeO_3$ and (110) for $ErFeO_3$. The spin moment on the rare earth ion gets ordered at a much lower Neel temperature [6.5 K for $HoFeO_3$ and 4.3 K for $ErFeO_3$].

1.3.4. Hexagonal ferrites

Another type of ferrite known as known hexagonal structure ferrite (or simply hexaferrites) are very important for applications viewpoint [VALE12]. These compounds have the general formula $MeFe_{12}O_{19}$ where Me is a divalent ion of a large ionic radius such as Ba^{2+}, Sr^{2+} or Pb^{2+}. Some compounds with trivalent Me (e.g., La^{3+}, Al^{3+}, Ga^{3+}, Cr^{3+}, Fe^{3+}) are also known [ALBA73]. In these, one iron per formula unit is present as Fe^{2+} to allow for charge compensation. Barium hexaferrite ($BaFe_{12}O_{19}$) is a typical example of this class of ferrites. In $BaFe_{12}O_{19}$, 8 of the Fe^{3+} ions are antiparallel to the other 4, so that the net moment is equivalent to $4Fe^{3+}$ ions, i.e. $20\mu_B$.

1.4. Magnetism in ferrites

Magnetization in ferrites arises from uncompensated antiferromagnetism. So, the magnitude of magnetization depends on composition, cation distribution and the relative strength of the possible interactions. Since cation-cation distances are large in ferrites due to their crystal structure, direct exchange interactions are negligible. Interactions in ferrites is mainly due to superexchange interaction between octahedral and tetrahedral cations or A-O-B interactions [SMIT53, VISW90, GOLD90]. The next acceptable interaction is B-O-B superexchange since A-O-A interaction is very weak [VALE94]. Magnetization depends on the strength of exchange interactions of the ferrites and this exchange interaction is mostly controlled by cation distribution. The magnetic exchange forces between the metal ions in the ferrites are mediated via oxygen ions by an exchange mechanism (also known as the superexchange interaction). If there are identical magnetic ions per unit volume, then a fraction x is located on A-sites and a fraction y = (1-x) on the B-sites. Let μ_A and μ_B represent the average moment of A and B ions in the direction of field at temperature T. μ_A and μ_B are not identical because ions A and B are exposed to different molecular fields. Then, the magnetization of the A-sublattice is $M_A = xn\mu_A$. The total magnetization of the two sublattices is

$$M = M_A + M_B \tag{1.2}$$

The molecular field acting on the sublattice A is

$$H_{mA} = -\gamma_{AB}M_B + \gamma_{AA}M_A \tag{1.3}$$

and molecular field acting on the sublattice B is

$$H_{mB} = -\gamma_{AB}M_A + \gamma_{BB}M_B \tag{1.4}$$

Here, M_A and M_B represent the magnetizations of the A and B sublattices, respectively. The strength of the exchange interactions between A-A, B-B and A-B ions are represented by γ_{AA}, γ_{BB} and γ_{AB}, respectively. The molecular field coefficients represented by γ are to be regarded as positive quantities and the negative sign corresponds to the antiparallel interaction between A and B ions, whereas the positive sign corresponds to the parallel interaction between the same site ions.

The magnetization of each sublattices obeys the Curie law, i.e.,

$$M_A = \frac{C_A}{T}(H + H_{mA}) \tag{1.5}$$

$$M_B = \frac{C_B}{T}(H + H_{mB}) \tag{1.6}$$

Since the Curie constants C_A and C_B are not identical for the two different sites, the above equations are modified by introducing the term density of ferrimagnetic materials on the right hand side. Now inserting the values of H_{mA} and H_{mB} in equations, the magnetization on the two different sites are obtained as

$$M_A = \frac{\rho C_A}{T}(H + \gamma_{AA}M_A - \gamma_{AB}M_B) \tag{1.7}$$

and

$$M_B = \frac{\rho C_B}{T}(H + \gamma_{BB}M_B - \gamma_{AB}M_A) \tag{1.8}$$

After solving these two equations, the mass magnetic susceptibility of a material is obtained as

$$\chi = \frac{M}{\rho H} = \frac{T}{C} + \frac{1}{\chi_0} - \frac{K}{T - \Theta} \tag{1.9}$$

where $C = C_A + C_B$ and K is a constant and Θ has the dimension of temperature. Therefore,

$$\chi = \frac{C}{T - \Theta} \tag{1.10}$$

The above equation confirms that a ferrimagnetic material obeys Currie-Weiss law [CULI72, VISW90, BLAX62].

1.5. Properties of ferrite nanostructures

Magnetic oxide nanoparticles contain oxides of magnetic elements such as Co, Ni, Fe. Magnetic nanoparticles have become important imaging tools for diseases like cancer, diabetes, and others. The unique ability of magnetic nanoparticles to response to an external magnetic field has been used for magnetic resonance imaging (MRI), cell tracking, tissue engineering, and drug delivery, and magnetic induction heating hyperthermia [WHIT03]. Magnetic nanomaterials have a major impact on the development of modern magnetic storage technology [GRUN01, PRIN98, DORM97]. As predicted by Frenkel and Dorfman [HIMP98, FREN30], a FM particle is expected to consist of a single magnetic domain below a critical particle size. The rough estimate of this critical particle size was first calculated by Kittel [KITT46]. An approximate radius of 15 nm is estimated for a spherical sample of a common FM material. The magnitude of magnetic moment of a particle is proportional to its volume. These single domain FM particles can be viewed as large magnetic units, each having a magnetic moment of about thousands of Bohr magnetons. Based on the magnetic response, magnetic nanoparticles are classified as diamagnetic (no response to external magnetic field, negative susceptibility), paramagnetic (weak response, low positive susceptibility) and ferromagnetic (high positive susceptibility) and antiferromagnetic. Depending on the size, magnetic nanoparticles even represent special class of magnetism known as superparamagnetism (zero coercivity, zero remenance and high saturation magnetization). Superparamagnetism is a unique feature of magnetic nanoparticles. It is of great interest because of the technological applications of magnetic nanoparticles including high-density data storage [KRYD96], contrast enhancement of magnetic resonance imaging (MRI)[MITC97] and magnetic drug delivery [HAFE97]. Superparamagnetic properties of nanoparticles are determined by the magnetocrystalline anisotropy, which comes from the L-S coupling at crystal lattices. According to the Stoner-Wohlfarth theory [STON47], the magnetocrystalline anisotropy E_A of a single-domain particle can be approximated as

$$E_A = KV\sin^2\theta \tag{1.11}$$

where K is the magnetocrystalline anisotropy constant, V is the volume of the nanoparticle, and θ is the angle between the magnetization direction and the easy axis of the nanoparticle. In magnetic nanoparticles with a spherical shape, the magnetocrystalline anisotropy can be

approximated as the total magnetic anisotropy [MOUN96]. E_A serves as an energy barrier for blocking the flips of magnetic moments. When E_A becomes comparable with thermal activation energy, k_BT, where k_B as the Boltzmann constant, thermal activation can overcome the anisotropy energy barrier and the nanoparticles become superparamagnetic with the magnetization direction randomly flipping. The characteristic time for one moment flip to the next is called the Neel relaxation time and is approximated by Neel-Arrhenius relation [GRIM75],

$$\tau = \tau_0 \exp(\frac{eV}{k_B T}) \tag{1.12}$$

where τ_0 is the time between flip attempts and is typically in the range 10^{-9} to 10^{-12}s depending on the material, V is the particle volume, k_B is the Boltzmann constant, and T is absolute temperature. From equation 1.12, it is clear that the relaxation time decreases or flipping frequency increases as the particle size decreases. The size limit required to achieve superparamagnetism can vary with core material composition. Higher magnetic saturation magnetization is the additional attractive property of superparamagnetic magnetic nanoparticles as compared to paramagnetic materials when exposed to an external magnetic field [WALK12, ZELE10]. This high magnetic saturation is the result of reorientation of individual domain. Because of the interesting properties of magnetic nanoparticles, iron oxide based spinel ferrites have become a very important material for application purpose.

1.6. Spinel ferrite nanostructures

Spinel ferrites have become important magnetic material system for reasons mentioned above [FINK89]. Chen et al. [CHEN99] have prepared $MgFe_2O_4$ nanoparticles by co-precipitation method which exhibited superparamagnetic properties for particle sizes ranging from 6 to 12 nm. They also anticipated that nanoparticles of $MgFe_2O_4$ may possess superparamagnetic properties even at relatively larger sizes. Giri et al. [GIRI05] have studied $MnFe_2O_4$ nanoparticles for hyperthermia therapy application. The specific absorption rate (SAR) was measured at a frequency of 300 kHz and a field of 10–45 kA/m. The variation of SAR and magnetization of $Fe_{1-x}Mn_xFe_2O_4$ with Mn concentration has also been studied by them. Biocompatibility and higher SAR value of these materials were found to be useful for hyperthermia applications. Jeun et al. [JEUN09] have studied the effect of particle-particle interaction on self-heating properties of $NiFe_2O_4$, $MgFe_2O_4$ and $CoFe_2O_4$. The study reveals that inter-particle interactions play a vital role in determining the magnetic properties of

magnetic nanoparticles. Arnold et al. [ARNO07] reported synthesis of $CaMn_2O_4$ nanowires with dimensions below 20 nm. They have proposed that nanowire geometry coupled with strain and possible quantum confinement effects lead to the FM ordering in this material. Tang et al. [TANG92] reported the size dependence of T_C and saturation magnetization of $MnFe_2O_4$ particles. They described the T_C enhancement by a finite-size-scaling formula and ascribed it to the confined measures of the material in three dimensions. Hynu et al. [HYUN09] demonstrated a concept to fabricate highly efficient photocatalyst configuration of bulk $CaFe_2O_4/MgFe_2O_4$ heterojunction. Chinnasamy et al. [CHIN00] prepared nanostructured $ZnFe_2O_4$ powders with different grain sizes by ball milling and found the magnetization increased with decrease in grain size. Chao et al. prepared magnesium and cobalt ferrite nanoparticle by micelle and reverse micelle method [CHAO00] with particle size of 4-30 nm. Qui et al. [CLIU00] have shown size dependent superparamagnetic properties of $MgFe_2O_4$ nanoparticles prepared by co-precipitation method with particle sizes of 6-18 nm. Potential applications of $MgFe_2O_4$ nanoparticles in ferro-fluids, magnetic refrigeration and magnetic resonance imaging have been pointed out [CHEN98]. According to McMichael et al [MCMI92], superparamagnetic ferrite materials can be used as a magnetic refrigerant. Nanocrystalline MFe_2O_4 (where M = Mn, Co, Mg and Ca) have been synthesized by micelle [CLIU00a, RANA10], sol–gel auto combustion [THAN10] and polymeric precursor [XMLI07] methods. Among these ferrites, calcium ferrite stands out as a material of interest both from applications as well as basic scientific viewpoints. The structure of $CaFe_2O_4$ remained unknown for number of years. Burdese [BURD52] reported that $CaFe_2O_4$ crystallizes in orthorhombic structure unlike most of the other spinel ferrites, which are cubic. $CaFe_2O_4$ has orthogonal unit cell with lattice parameter (a = 9.230 Å, b = 10.705 Å, c = 3.024 Å) with space group space group Pnma, No. 62 [DECK57]. Moreover, the large ionic radius of Ca forces it to be 8- or 9-fold coordinated in the $CaFe_2O_4$ structure [CORL67]. However, there are only a few reports on orthorhombic $CaFe_2O_4$. It has been prepared in bulk and nanocrystalline forms using polymeric precursor [CAND04], citrate gel [KHAN13] and mechano-synthesis [BERC10] routes and its properties have been explored to a limited extend.

1.7. Some applications of spinel ferrites

Ferrites are regarded as much better magnetic materials than pure metals because of their high resistivity, lower cost, easier manufacture and superior magnetization properties. Ferrites are generally used in radar, audio–video and digital recording, memory cores of

computers, satellite communication and microwave devices [HAGF95, PRAS98, VISW90]. Ferrites also find applications in high frequency devices operating from microwave to radio frequencies. Ferrites are available as both soft magnetic and hard magnetic ferrites, which is another reason for its wide application. Let us now see some specific applications of nanocrystalline spinel ferrites.

Thin films of spinel ferrites can be used as write-once read many times media working with blue wavelengths [LAUR99]. Soft magnetic ferrite films have been prepared by a combination of sol-gel and spin-coating techniques for use as inductors in microelectronics [YANG06]. New generation of magnetic field sensors based on ferrites and piezoelectric oxide layers are being developed [FETI06]. These sensors can provide high sensitivity, miniature size, and virtually zero power consumption. Ferrite cores based on nanocrystalline $Mn_xNi_{0.5-x}Zn_{0.5}Fe_2O_4$ have been developed with low eddy current for switched mode power supplies [VERM06, ZASP04]. Magnetic nanoparticles, mainly magnetite (Fe_3O_4) are present in various living organisms [LOWN62]. Many biomedical applications have been developed based on biogenic and synthetic magnetic micro- and nanoparticles [ZHAN98]. Magnetic nanoparticles have been used to deliver radionuclides to specific tissues. An approach has been developed to directly label a radioisotope in vivo with ferrite particles in rat tissue [CMFU05]. Magnetite superparamagnetic particles have been used to enhance magnetic resonance imaging, [MART98, TCYE95]. Thermal energy from magnetic hysteresis loss of ferrites can be used in hyperthermia, that is, the heating of specific tissues or organs for treatment of cancer [HERG06]. This therapy is based on the fact that cancerous cells can be selectively killed by local heating since healthy tissues can withstand much higher temperatures than the malignant ones [SHAR12].

1.8. Focus of the Present Thesis

This thesis work is motivated by the (1) controversy existing in understanding the mechanism behind RTFM in ZnO nanostructures, (2) lack of information on the non-cubic ferrite $CaFe_2O_4$ and (3) lack of reports on other low dimensional forms of these technologically important magnetic materials. So, undoped and TM doped ZnO with novel 1-d nanostructure were prepared by a combination of sol-gel and electrospinning techniques. Similarly, 0-d and 1-d $Co_xCa_{1-x}Fe_2O_4$ have been prepared by these techniques. Investigations carried out on these nanostructures have yielded several interesting results and insights which are presented in chapters 3 to 6 of this thesis. In chapter 3, the effect of annealing temperature on the

evolution of nanocrystalline microstructure and the resulting properties of as-spun PVA/ZnO nanofibers prepared by electrospinning technique are presented. Chapter 4 discusses the effect of annealing on Mg and Co substituted ZnO nanofibers. Chapter 5 explores the formation of nanocrystalline cubic $CaFe_2O_4$ and $Co_xCa_{1-x}Fe_2O_4$ (x = 0.1) powders by sol-gel method and their transformation to orthorhombic phase upon annealing. Chapter 6 presents the synthesis of PVA nanofibers containing Ca and Fe salts and the effect of annealing them at different temperatures up to 1000 °C.

Chapter 2

EXPERIMENTAL TECHNIQUES

In this chapter, experimental techniques used for preparing and evaluating the nanostructures are discussed together with a brief description of the theory associated with these techniques. The methodology adopted to analyze the experimental data obtained from various tools is also discussed here.

Methodologies used in the preparation of nanostructures are often specific to the materials concerned. Similarly, the procedures adopted for acquiring specific experimental data and for the extraction of required parameters from the data depend on the need. Hence, the experimental techniques used in this thesis work are briefly outlined below.

2.1. Sample preparation

Sol-gel and electrospinning methods have been employed either independently or together to prepare both the semiconductor and ferrite nanostructures. A brief discussion on both these techniques is given below.

2.1.1. Sol-gel technique

The sol-gel process is a wet-chemical technique where initially a stable colloidal solution called 'sol' is formed [BRIN90]. The sol is a liquid suspension of solid particles ranging in size from 1 nm to 1μm. It can be obtained by hydrolysis and partial condensation of precursors such as an inorganic salt or a metal alkoxide. In hydrolisis process a metal cation (M^{z+}) dissolved in water, introduced on the form of salts are solvated by water molecules according to the reaction,

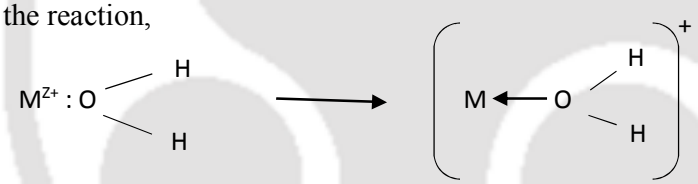

(2.1)

For TM cations, charge transfer occurs from the filled bonding orbital of the water molecule to the empty d orbitals of the TM [FORT80]. Depending on the acidity level of water and the magnitude of the charge transfer, an equilibrium is established which is known as hydrolysis.

$$[M(OH_2)]^{z+} \rightleftharpoons [M\text{-}OH]^{(z-1)+} + H^+ \rightleftharpoons [M{=}O]^{(z-2)+} + 2H^+ \qquad (2.2)$$

Subsequent condensation of the sol particles into a 3-dimensional network produces a 'gel'. The gel is a diphasic material in which the solids encapsulate the solvent. The encapsulated liquid can be removed from a gel by either evaporative drying or by supercritical drying /extraction. When gels are dried by evaporation, the dried product is called xero-gel. When the gels are supercritically dried, it is called aerogel. Various sol-gel processes are illustrated in Figure 2.1.

This method has been used for the fabrication of nanoscale metal oxides, glasses, glass-ceramics, etc. [BAAB15]. A simple wet gel procedure was adopted to prepare calcium ferrite nanoparticles in this thesis work. It involves the following steps: Analytical grade

$Ca(NO_3)_2.4H_2O$ and $Fe(NO_3)_3.9H_2O$ taken in 1:2 molar ratios were first dissolved in 100 ml doubly distilled deionized water. The mixture maintained at a moderate temperature of 40 to 50 °C was constantly stirred until a light greenish sol is obtained. Then, 5 ml of ethylene glycol was slowly added to the warm sol under constant stirring to obtain a thick greenish gel. The xerogel product was subsequently obtained by drying the gel at in air at 120 °C for 12 h. The dried calcium ferrite nanometer sized powders were heat treated at elevated temperature to fully crystallize them.

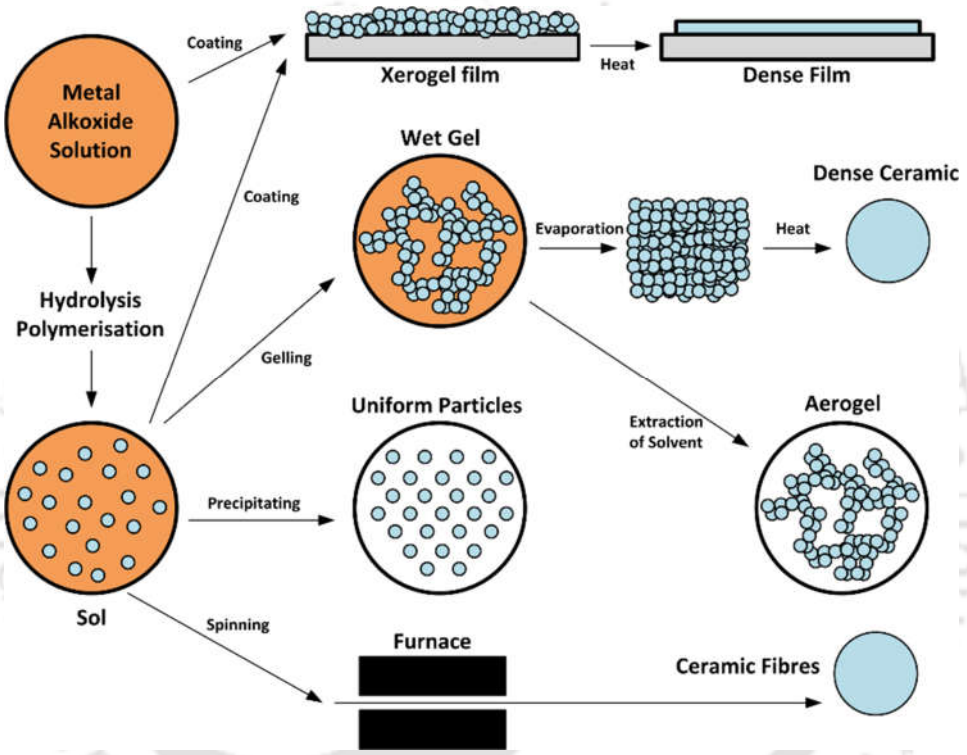

Figure 2.1: Schematic of sol-gel processes leading to nanoscale powders or a dense film.

2.1.2. Electrospinning technique

The process of electrospinning (ES), namely utilizing electrostatic forces to generate polymer nanofibers, traces its roots back to the process of electrospraying, in which solid polymer droplets are formed rather than fibers [RAMA05]. In fact, a number of processing parameters must be optimized in order to generate nanofibers as opposed to droplets, and so a typical electrospinning apparatus can be used to form fibers, droplets, or a beaded structure depending on the various processing parameters. ES technique was used for producing nanofibrous membranes from composite polymer solutions in this thesis work. The electrospinner (Nabond NEU), the experimental arrangement and the final product obtained

are depicted in Figure 2.2. A typical ES setup consists of a metal capillary with a blunt tip through which the liquid to be electrospun is forced out, a high voltage DC power supply source which injects charges into the liquid and a grounded collector. A syringe pump (or gravitational force or pressurized gas) is usually used to force the liquid through the capillary forming a pendant drop at the flat tip. The positive electrode of the high voltage source is then connected to the metal capillary [TRAV08a].

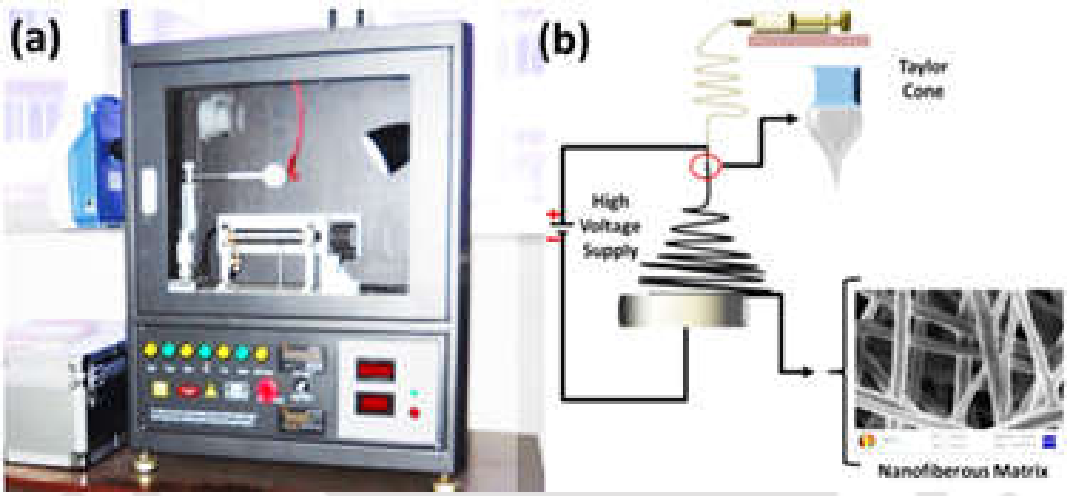

Figure 2.2: (a) Photograph of the ES setup used. (b) Schematic diagram of experimental design.

When the voltage source is then turned on, charges are injected into the polymer solution. Increasing the electric field strength causes the repulsive interactions between like charges in the liquid and the attractive forces between the oppositely charged liquid and collector to begin to exert tensile forces on the liquid. This elongates the pendant drop at the tip of the capillary [RAMA05a]. As the electric field strength is increased further, a point will be reached at which the electrostatic forces balance out the surface tension of the liquid leading to the development of the Taylor cone. If the applied voltage is increased beyond this point a fiber jet will be ejected from the apex of the cone and be accelerated toward the grounded collector. The fiber jet undergoes a chaotic bending instability, which increases the transit time and the path length to the collector and aiding in the fiber thinning and solvent evaporation processes. The solid polymer fibers are then deposited onto a grounded collector. Depending on the application, a number of collector configurations can be used, including a stationary plate, rotating drum, etc. Typically, the use of a stationary collector will result in

the formation of a randomly oriented fiber mat. Despite the relative ease in the use of ES technique, there are a number of processing parameters that can strongly influence the fiber formation, fiber diameter and structure which can be grouped as intrinsic and extrinsic parameters. Intrinsic parameters include the type of polymer and its molecular weight, type of solvent, concentration of the polymer in the solvent, viscosity, electrical conductivity and surface tension of the solution. Extrinsic parameters consist of the electric field strength, distance between nozzle (metallic needle, anode) and the collector (cathode), solution flow rate, shape and movement of the collector. Apart from these, ambient parameters such as temperature and humidity also influence the ES process.

In this thesis work, all the processing parameters were optimized for obtaining composite nanofibers using polyvinyl alcohol (PVA) solutions. For the preparation of the ES solution, an aqueous PVA solution (12 w/v %) was first prepared by dissolving appropriate amount of PVA (MW ~80,000, Sigma-Aldrich) powder in deionized water heated to 80 °C under constant stirring until a homogeneous solution was obtained. The metal precursor solution was separately prepared by dissolving appropriate amount of the metal salt in deionized water accompanied by stirring. The metal precursor solution was finally added slowly to the warm PVA solution with continuous stirring to obtain a homogeneous mixture. It was found that stirring for 2 h yields the homogenous mixture. This mixture was kept at room temperature for 4-5 h to obtain a viscous solution suitable for ES. All such solutions containing various concentrations of the metal precursor were electrospun under applied electrical potential difference of 12~20 kV with a needle to collector distance of ~15 cm. A drum shaped collector (cylinder), rotating about its axis at ~400 rpm was used as the collector of the nanofibrous membranes. A constant solution flow rate of ~1-2 ml/h was maintained in all experiments and all the experiments were performed at controlled ambient conditions.

2.1.3. Post synthesis heat treatment

In order to optimally crystallize the nanocrystalline microstructure and to induce temperature dependent structural phase transitions, as-synthesized xerogel powders and as-spun composite nanofiber mats were heat treatment at elevated temperatures in ambient conditions using a resistive tubular furnace (Okay, India). This tubular furnace could be used to attain temperatures up to 1600 °C. The temperature of the constant temperature heat zone at the center of the furnace extends to 150 mm. The annealing temperature was controlled to ± 2 °C using a commercial PID temperature controller. The annealing temperature and annealing

time were optimized depending upon the requirement as will be explained in the following chapters.

2.2. Characterization Techniques

Several standard characterization tools have been utilized to characterize the samples. X–ray diffraction (XRD), field emission scanning electron microscopy (FESEM), transmission electron microscopy (TEM) and energy dispersive X-ray absorption spectroscopy (EDS) unit attached to the FESEM were used to determine the crystal structure, morphology, orientation, and composition, respectively, of the nanocrystalline samples. Micro–Raman, ultraviolet-visible (UV–vis) absorption and photoluminescence (PL) spectrometers were used for spectroscopic studies. Magnetic properties were measured using a vibrating sample magnetometer (VSM) and Mössbauer spectrometer equipped with a variable temperature sample holder. A differential thermal analyzer cum thermo-gravimetric (DTA-TG) analyzer was employed to understand the thermal evolution of the as-synthesized samples.

2.2.1. Morphology, structure and composition

2.2.1.1. Field–Emission Scanning Electron Microscopy

Scanning electron microscope (SEM) is a useful tool for high resolution surface imaging in materials science. In principle, it is similar to an optical microscope operating in the reflection geometry. However, as the name suggests, SEM uses a fine beam of electrons instead of visible light to probe the morphological features of objects. The use of electrons has two main advantages over optical microscopes, viz., much higher magnifications are possible since electron wavelengths are much smaller than photon wavelengths and the depth of field is much larger. The electron wavelength λ_e (in nm) depends on the electron velocity v or the accelerating voltage V (in kV) as per the relation [CHAR92],

$$\lambda_e = \frac{h}{mv} = \frac{1.22}{\sqrt{V}} \tag{2.3}$$

Thus, for a typical 30 kV acceleration voltage, the resolution is extremely high. On the other hand, ultra-high vacuum sample holder, sophisticated electric and magnetic field based beam control elements and circuits, high resolution imaging and associate electronic hardware and software are required to fabricate the electron microscope. Vacuum environment allows the movement of the electrons along a columnar path without scattering which helps to prevent discharges inside the instrument. The type of electron source is the main difference between

SEM and field emission SEM (FESEM). In SEM, electrical current is used to heat up the filament and induce thermionic emission of electrons from it.

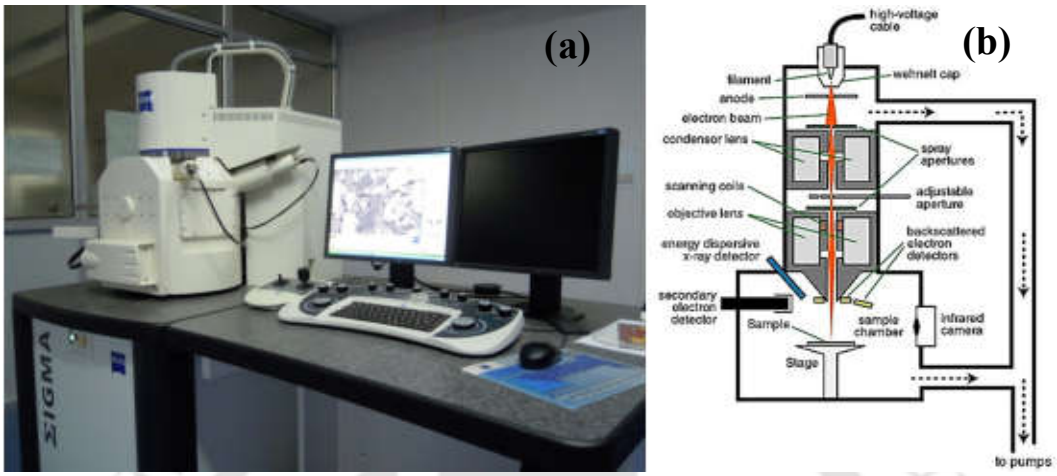

Figure 2.3: (a) Photograph of the Field Emission Scanning Electron Microscope (Sigma Zeiss, Germany). (b) Schematic diagram of the electro-optical components in an FESEM.

A photograph of the FESEM (Sigma Zeiss, Germany) used in the present study is shown in Figure 2.3(a). A schematic diagram of the experimental geometry of an FESEM is provided in Figure 2.3(b). The field emission source is tungsten filament (cathode) with sharp tip which is placed in a huge electrical potential gradient. The significance of the extremely thin and sharp tip (diameter ~10-100 nm) is that an electric field can be concentrated to an extreme level so that the work function of the material is lowered. This favours easy emission of electrons from the cathode. After emission, the electrons are accelerated by the anode. An accelerating voltage of 0.5 - 30 kV is commonly applied between the cathode and anode. This voltage combined with beam diameters determines the resolution of the image. As the voltage increases, better point-to-point resolution can be obtained. Because of the smaller size of the electron source, the beam produced by this emitter is about 1000 times smaller than that in a standard scanning electron microscope (SEM), which markedly improves the image. The beam is collimated by electromagnetic condenser lenses, focused by an objective lens, and scanned across the surface of the sample by electromagnetic deflection coils. The primary imaging method is by collecting emitted secondary electrons that are released by the sample. A secondary electron detector is placed near to the specimen. By correlating the sample scan position with the resulting signal, an image is formed on the screen that is strikingly similar

to what would be seen through an optical microscope. The FESEM is equipped with a special objective or focusing lens that projects the magnetic field below the lens. Very high resolution is obtained by shortening the specimen–lens distance and using a specially designed in–lens. The distance is shortened by placing the specimen in the lens magnetic field. In this case, secondary electron detector is placed above the objective in–lens (called as in–lens detector), which makes significant difference in the image compared to the conventional image of the secondary electron detector. Very high resolution and contrast can be obtained by using in–lens detector. In the current work, the samples were either xerogel or 1-d powders or as-spun nanofiber strips. These samples were directly mounted on the FESEM stub using carbon tape. This stub is connected to the anode of the FESEM and is at the focus of the electron beam. The carbon tape served as adhesive to stick the powders apart from providing an electrical conduction path to the sample.

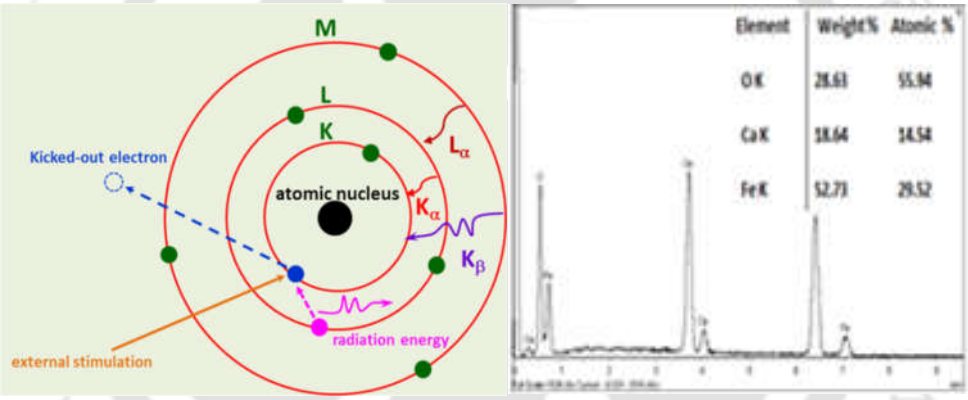

Figure 2.4: (a) Schematic of X-ray emission by high energy electrons. (b) Typical EDS spectrum of a sample with elemental composition map in atomic and percentages.

Composition of the sample over regions as small as the beam diameter can be obtained by energy dispersive spectrometer (EDS) attachment in a SEM or FESEM [CHAR92]. EDS analysis is based on the understanding that when high energy electrons collide with the electrons of atoms in the specimen, they knock some of them off. A position vacated by an ejected inner shell electron is eventually occupied by a higher-energy electron from an outer shell by emitting an X-ray. The amount of energy released by the transferring electron depends on which shell it is transferring from, as well as which shell it is transferring to. Furthermore, the atom of every element releases X-rays with unique amounts of energy during the transferring process. Thus, by measuring the amounts of energy present in the X-

rays being released by a specimen during electron beam bombardment, the identity of the atom from which the X-ray was emitted can be established. Figure 2.4 (a) schematically shows the processes involved. The EDS spectrum is just a plot of how frequently an X-ray is received for each energy level. As EDS analysis provides elementary composition of the system. Empirical formulation of the system can be obtained by taking atomic fraction (or weight fraction) of different elements. A typical EDS spectrum and the estimates of elemental composition percentages are illustrated in Figure 2.4 (b).

2.2.1.2. Transmission Electron Microscopy

Transmission electron microscope (TEM) is one of the important characterization techniques using which structural information can be acquired by high resolution imaging close to the atomic level (0.2 nm) as well as by electron diffraction [CHAR92]. The high resolution TEM (HRTEM) known as lattice imaging, gives structural information and reveals the presence of defects or dislocations in the crystal lattice. The growth orientation and lattice spacing can be studied from the lattice fringe image. Crystallographic information about the nanomaterials such as crystal structure (cubic, tetragonal, hexagonal or monoclinic etc.), crystallinity (single crystalline, poly-crystalline or amorphous) can be drawn from the selected area electron diffraction (SAED) patterns. In the case of a crystalline material, electron diffraction will only occur at specific angles which are the characteristic features of the crystal structure present. Moreover, elemental and chemical composition analysis down to sub-nanometer scale can be acquired with additional detector such x-ray detector which is known as energy dispersive x-ray (EDX) analysis. Figure 2.5(a) shows the schematic diagram of a TEM. It works on the principle of optical projection. When an object is placed in front of a light source, its image is enlarged and a shadow is created on the screen placed at a far distance behind this object. Electrons emitted from an electron gun are accelerated to high voltages (typically 100 to 400 kV) and focused on the sample by a number of condenser lenses [SCHR06a]. It is normal to use a lanthanum hexaboride (LaB_6) crystal for thermionic electron emission. These electron pass through a series of electric and magnetic lenses, get focused and then scanned across the sample.

The sample is placed on a small copper grid a few mm (~3 mm) in diameter. The static beam has a diameter of a few microns. The sample must be sufficiently thin (a few tens to a few hundred nm) to be transparent to electrons. The transmitted and forward scattered electrons form a diffraction pattern in the back focal plane and a magnified image in the image plane.

With additional lenses, either the image or the diffraction pattern is projected onto a fluorescent screen for viewing or photographic recording.

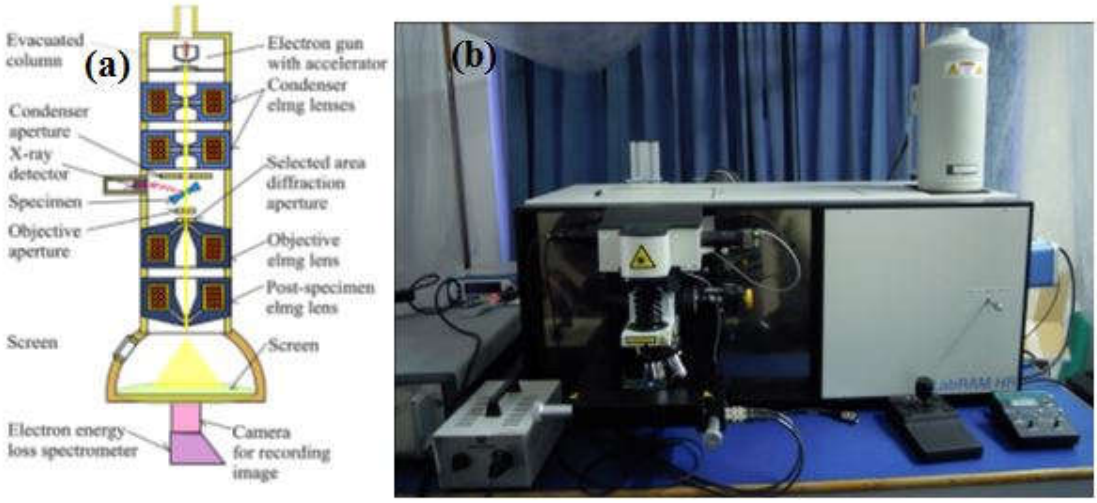

Figure 2.5: (a) Schematic diagram of a transmission electron microscope. (b) Photograph of the TEM (JEOL, JEM 2100) used in the present investigations.

In our present study, a TEM (JEM2100, JEOL, Japan) operating at 200 kV with high resolution charge coupled device (CCD) camera (Gatan, USA) was used for the regular TEM and HRTEM imaging. Figure 2.5(b) shows a picture of the instrument. Sample for TEM imaging is an arduous task since the parts of interest should be thin enough for transmission of the electrons. In our case, the nanostructures samples were already in the form of powders. So, they were dispersed in ethanol in low concentrations. A transparent dispersion of the nanostructures was obtained by high frequency sonication which were then drop casted on the carbon coated copper grid containing few hundreds of square shaped hollow meshes with dimension of ~1 μm. After normal drying to evaporate the alcohol, the sample loaded grid was used for TEM imaging. Improved resolution of the lattice image was obtained after by fast Fourier transformation (FFT) using Digital Micrograph (Gatan, USA) image analysis software. In addition, selected area electron diffraction (SAED) patterns were recorded and analyzed to obtain inter planar distance along the preferred orientation in the nanostructures.

2.2.1.3. X–ray Diffraction

Powder x-ray diffraction (XRD) is the most widely used non-destructive technique for primary structural characterization of materials. XRD patterns provide information on crystal phases, lattice parameters, average crystallite size and strain in the material. In powder XRD

of crystalline materials, a collimated beam of x–rays, with wavelength λ = 0.5–2.0 Å, incident on a finely powdered sample is diffracted by the atoms in the plane satisfying the Bragg's law,

$$2d\sin\theta = n\lambda \qquad (2.4)$$

where d is the spacing between atomic planes in the crystalline phase, θ is the angle of incidence of the x–ray beam with the atomic plane, n is the order of diffraction (we consider only the first order diffraction, i.e., n = 1, because the higher order peaks are mostly too weak in intensity to detect experimentally). The intensity of the diffracted x–rays is measured as a function of the diffraction angle 2θ. In powder samples, the crystallites are oriented in random orientations, thereby enabling the capture of x-rays reflections from all possible planes. It should be noted here that preferred orientation of the crystallites can occur. In an x-ray diffraction pattern, the position and intensity of the diffraction peaks are characteristic for the crystallographic structure and the atomic composition of the material. In the case of a multi-phase composition, the resulting pattern is a combination of the patterns of all structures present. Phase identification can be done by matching the XRD pattern with reference patterns of pure substances. Owing to the huge data bank available from JCPDS Powder Diffraction Files, practically every phase of every known material can be identified.

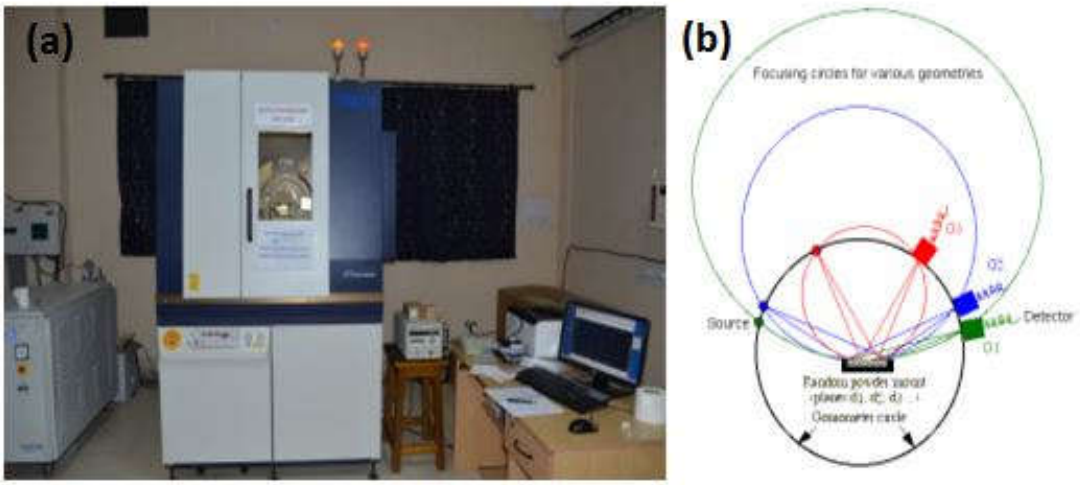

Figure 2.6: (a) Photograph of rotating anode based Rigaku TTRAX III, 2500 powder X-Ray diffractometer. (b) Schematic diagram of the measurement using θ-θ goniometer.

X–ray diffraction patterns of the nanostructured samples prepared in this thesis work were obtained using a commercial x-ray diffractometer (TTRAX III, Rigaku 2500) using a Cu Kα1 (λ = 1.5406 Å) radiation. A photograph of the XRD instrument in our laboratory is

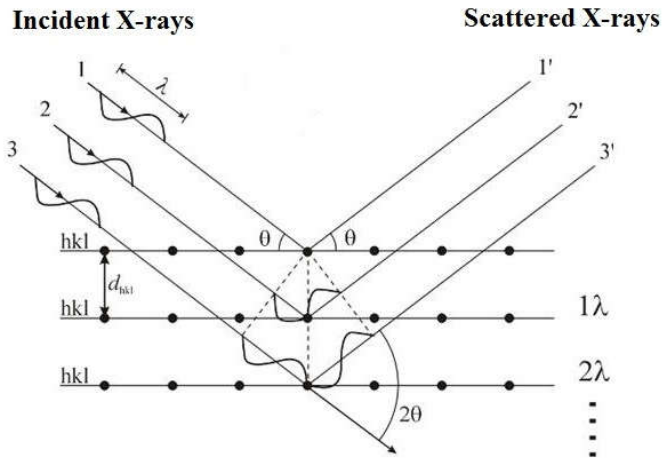

Figure 2.7: Schematic ray diagram of diffraction of X-rays by a crystal.

shown in Figure 2.6(a). It uses a rotating anode based x-ray source which is capable of operating up to 18 kW of input power. However, all measurements made for this thesis work were carried out using an acceleration voltage of 50 kV and tube current of 200 mA i.e., at input power of 10 kW. The angular step size used was 0.01°. The average size (d_{av}) of the fine crystallites and the microstrain (ε) can be estimated from the broadened peaks using the Williamson–Hall relation [KHOR11a],

$$\beta \cos\theta = K\lambda / d_{av} + 4\varepsilon \sin\theta \qquad (2.5)$$

where β is the full width at half maximum of the Bragg peak (in radians), θ is the diffraction angle at the peak maximum, and K is a constant which depends on the shape of the crystallite. Here, it is taken as 0.89 by assuming the shape of the crystallites to be spherical. The first term in Eqn. 2.4 is the Schërrer's relation which presumes that the peak broadening is entirely due to the small crystalline size of the sample, or

$$d_{av} = K\lambda / \beta \cos\theta \qquad (2.6)$$

This relation is used to estimate d_{av} of nanocrystallites from XRD patterns with very few peaks or in the case of samples with no internal strain. The instrumental broadening effect has been taken into account by subtracting it from the β_{obs}. For this, width (FWHM) of peaks in XRD pattern of standard (well crystallized) Si recorded under same conditions was used. A schematic representation of the XRD phenomenon from a crystal and the geometry employed to record the powder XRD pattern are shown in Figure 2.7.

2.2.2. Optical characterization

2.2.2.1. Ultraviolet-visible-near infrared spectrophotometry

Figure 2.8: Photograph of the Diffuse Reflectance Spectrometer (Perkin Elmer, LAMBDA 750)

The energy gap (E_{bg}) of semiconductors determines their applications in optoelectronics, photocatalysts and photovoltaics. The optical reflectance or absorbance is a result of interaction of light with the material. The basic principle behind the technique is that visible or near infrared (NIR) light is used to excite electrons from the valance band to the empty conduction band. A sharp increase in absorption (or reflection) at energy close to the band gap results in the absorption edge in the UV-visible-NIR absorbance (or reflectance) spectra. This technique is mostly applicable to thin film samples. For powder samples, usually UV-visible absorption spectroscopy is carried out by dispersing the sample in a liquid medium like water, ethanol or methanol. If the particle size of the sample is not small enough or not well dispersed in the solvent, it precipitates and it is very difficult to get good absorption spectrum. So diffuse reflection spectroscopy (DRS) is used, which enables one to obtain absorbance as well as the band gap energy (E_{bg}) with more accuracy [MORA07]. Reflectance of samples can be measured using either an integrating sphere or a specular reflectance accessory. Integrating spheres are used for samples with a significant diffuse reflectance component such as powders and other 'rough' materials. Samples are placed at the back of the sphere and the light is reflected back off the sample and collected by the sphere. Measurements generally provide the total reflectance. The latter measurement is achieved by allowing the specular component to exit the sphere through the open specular port. The absorbance can be calculated using Kubelka-Munk formula [KUBE31] which states that the Kubelka-Munk (K-M) function,

$$F(R_\infty) = \frac{(1-R_\infty)^2}{2R} = \frac{k}{s} \qquad (2.7)$$

where $R_\infty = \frac{R_{sample}}{R_{s\,\tan dard}}$, k = K-M absorption coefficient and s = K-M scattering coefficient.

Here, we used a Perkin-Elmer (LAMBDA 750) spectrophotometer for the DRS measurements. Figure 2.8 shows a photograph of the DRS spectrophotometer used in this study. It performs the measurement in the UV-visible-NIR range i.e., 200 – 2500 nm. Deuterium and tungsten halogen light sources are provided to perform the measurements in the required wavelength region. An integrating sphere along with a set of detectors (photomultiplier tube, InGaAs and PbS) is used to collect the diffuse reflectance light being reflected from the sample in all direction and convert it to electrical signal. Calibrated spectralon diffuse reflectance standard is used as reference. A sample holder kit with a quartz piece on the front is used to hold the powder sample. A schematic diagram of diffuse reflectance mechanism is shown in Figure 2.9.

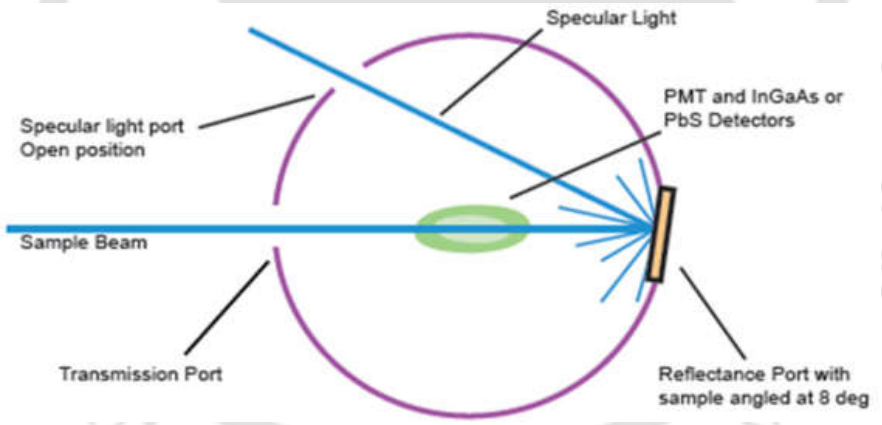

Figure 2.9: Schematic diagram illustrating diffuse reflectance mechanism.

2.2.2.2. Micro-Raman Spectroscopy

Micro–Raman spectroscopy is a vibrational spectroscopic technique which is based on Raman spectroscopy [LUKA12]. It is now widely used to characterize both structural as well as spectroscopic characterization of a bulk and nanostructured materials. Raman scattering corresponds to the interaction between incident photons and the optical phonons. In a micro-Raman measurement, an intense laser beam is incident on the sample through a commercial microscope with spot size about few microns. The weak back–scattered light or signal from

the sample is passed through a double monochromator to reject the Rayleigh scattered light component and the Raman–shifted wavelengths are detected by a photodetector or CCD detector. The Raman lines broaden for disordered materials, allowing a distinction to be made between single crystal, polycrystalline, and amorphous materials. Raman spectral profile contains information about structure, crystallinity, strain and phonon confinement effects in nanostructures [OZGU05]. The frequency of the Raman signal is also shifted by stress and strain in nanostructure. Both compressive and tensile stress can be determined with compressive stress giving an upward and tensile stress a downward shift compared to the peak position of the unstrained crystal [DRESS07]. A high resolution micro–Raman spectrometer (LabRAM HR–800, Jobin Yvon, USA) with liquid nitrogen cooled CCD detector used in the present studies is shown in Figure 2.10 (a). All measurements were performed at room temperature using a 488 nm line of an argon ion laser at a resolution of 0.3 cm^{-1}. The laser power at the sample side was 0.9 mW.

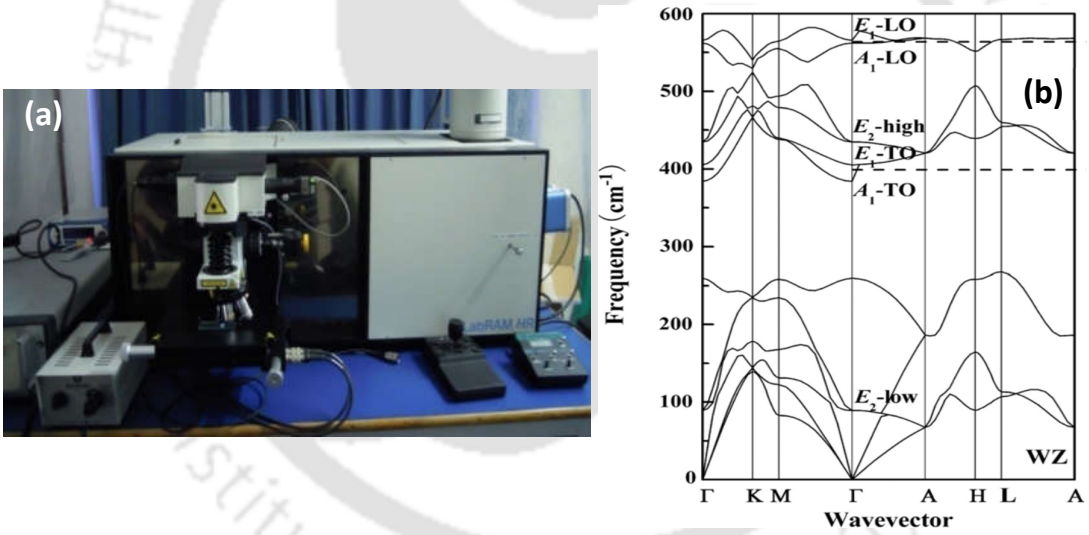

Figure 2.10: (a) Photograph of the micro–Raman spectrometer (LabRAM HR–800, Jobin Yvon,USA). (b) Calculated phonon dispersion curves of wurtzite (WZ) ZnO crystal [YWU09].

We know that ZnO crystallizes in hexagonal wurtzite structure with space group $P6_3mc$ which has two formula units in the primitive cell. Single crystalline ZnO at Γ point of the Brillouin zone has eight sets of optical phonon modes [ZHAN09a] which are shown in phonon dispersion curve of pure hexagonal ZnO in Figure 2.10(b). They are the $A_1 + E_1 + 2E_2$ modes, which are Raman active, $2B_1$ modes which are Raman silent and $A_1 + E_1$ modes

which are infrared active. The polar modes of A_1 and E_1 are split into transverse (TO) and longitudinal optical (LO) phonon, while the nonpolar modes of E_2 have two frequencies identified as E_2^{high} and E_2^{low} associated with oxygen atoms and Zn sub lattice, respectively [OZGU05]. E_1^{LO} mode is caused by the defects such as oxygen vacancy, zinc interstitial or their complex, which enables to identify the defects present in the ZnO nanostructures. Compared to bulk ZnO, the decreased dimensions of ZnO nanowires lead to spatially confined phonons, giving rise to the phonon quantum confinement effect. Characteristics of phonon confinement could be due to [DRES07] (1) frequency downshift and Raman line shape broadening, whereas structural defects and residual stress could also contribute to the phonon linewidth broadening and (2) generation of new features absent in the corresponding bulk spectrum. Raman spectrum typically shows Lorentzian line shape [BART72]. Experimental data are analyzed by fitting multiple peaks with Lorentzian peak shape profile to extract the peak parameters.

2.2.2.3. Photoluminescence spectroscopy

Photoluminescence (PL) is the emission of light from a material under optical excitation [THON01]. Excitation energy is required to excite the electron from lower energy level (ground state) to higher energy level (excited state). Light of suitable energy is directed onto a sample, where it is absorbed and imparts excess energy into the material in a process called photo-excitation. This causes electron-hole pair generations within the material and those electrons move into permissible excited states. The excess energy can be released by the sample through the emission of light or luminescence, when these electrons return to their equilibrium states and the whole process is called photoluminescence. The energy of the emitted light (PL) relates to the difference in energy levels between the two electron states involved in the transition between the excited state and the equilibrium state. The quantity of the emitted light is related to the relative contribution of the radiative process between the various excited states (as defect states near the conduction act as a luminescence centers) and the equilibrium states. Features of the emission spectrum provide the information about the band gap energy, impurity/defect level and electron hole recombination mechanism. The intensity of the PL signal can be used to extract qualitative information about the contribution of various defect states. The most common radiative transition in semiconductors is between the states in the conduction and valence bands, with the energy difference being known as the band gap. Radiative transitions in semiconductors also involve localized defect levels within

the band gap of the semiconductor. The PL energy associated with these levels can be used to identify specific defects, and the amount of PL can be used to determine their relative concentration. The return of the excited electrons to equilibrium state to recombine with holes, also known as "recombination," can involve both radiative and non-radiative processes. The amount of PL and its dependence on the level of photo-excitation and temperature are directly related to the dominant recombination process [GILL97a]. Analysis of PL helps us to understand the underlying physics of the recombination mechanism. The fundamental limitation of PL analysis is its reliance on radiative events. Materials with poor radiative efficiency, such as low-quality indirect band gap semiconductors, are difficult to study using ordinary PL. Similarly, identification of impurity and defect states depends on their optical activity. More intense laser excited PL is generally preferred to study the defect/ impurity states such as oxygen vacancy as compared to ordinary xenon-lamp based PL system. We used 325 nm He-Cd laser and 405 nm diode laser (Coherent, Cube) excitation in conjunction with a spectrometer (focal length: 15 cm; blaze wavelength: 500 nm; groove density: 150 g mm^{-1}) equipped with a cooled CCD (Princeton Instruments, PIXIS 100B) detector in the present studies. Extended NIR PL measurements were carried out using a liquid N_2 cooled InGaAs detector (OMA-V-SE, Roper Scientific).

Figure 2.11: Photograph of the Photoluminescence spectrometer with CCD detector.

Figure 2.11 shows a photograph of the PL instrument used in the present study. The PL measurements were mostly carried out at room temperature. The measurements were performed by spreading powder samples on a conducting black carbon tape. Each spectrum was corrected for the detector response as a function of wavelength after background subtraction. The steady state PL peaks profiles are usually Gaussian in nature, expressed by

$$y = y_0 A \exp[-(\frac{(x - x_c)^2}{2w^2})] \quad (2.8)$$

where is y_0 the offset constant, x_c, w and Aare the peak position, width and peak amplitude, respectively. The measured PL spectrum was analyzed by fitting with Gaussian line-shape function or multiple Gaussian functions using a peak fitting software (Microcal Origin).

2.2.3. Magnetic characterization

2.2.3.1. Vibrating Sample Magnetometer (VSM)

VSM measures net the dipole moment of a material exposed to magnetic field [SVOB04a, CZIC06a]. The magnetic moment of the material can be obtained either as a function of applied magnetic field called magnetic hysteresis (M-H) loop to investigate the evolution of magnetic properties with field or as a function of temperature (M-T) to understand the temperature induced magnetic phase transition in a material. When a solid sample is placed in a uniform magnetic field, a dipole moment proportional to the product of the sample susceptibility and the applied field is induced in the sample. If the sample is made to undergo sinusoidal motion, an electrical signal can be induced in suitably located stationary pickup coils. This signal amplitude is proportional to the magnetic moment of the sample, the vibrating amplitude and the vibration frequency. Through the use of lock-in-amplifier and feedback techniques, only that portion of the signal arising from the magnetic moment is picked up and is converted into direct read-out in the unit of magnetization (e.g. emu) on a digital panel meter. An electromagnet based VSM (Lakeshore Model 7410, USA) was used to characterize room temperature and temperature dependent magnetic properties in the temperature range 20 K – 300 K and 300 K- 1100 K. VSM consists of the following major parts: a) Vibration exciter and sample holder, b) Water cooled electromagnet and power supply, c) Hall probe, d) pick-up coils, e) amplifier, f) control panel, g) lock-in amplifier and h) computer interface. The sample is fixed at the lower end of a non-magnetic quartz sample rod. The sample is fixed at the lower end of the sample holder after completing the calibration procedure using standard Ni sphere. The measurement sequence is then programmed as per the user's choice using the software (IDEASVSM) provided with the instrument such that the program starts either from the maximum field or from the zero applied field. The sequence is made so that sufficient number of data points are collected, which helps to extract the magnetic parameters (saturation magnetization, remanence magnetization, coercivity, etc.) accurately. The exciter is vibrated at a frequency of 72 Hz and

the signal received from the hall probe and the pick-up coils is converted into the magnetic moment of the sample. The magnetic field is increased automatically in user-defined steps for acquiring the M-H loops. Similarly, for low and high temperature M–T measurements, a closed cycle refrigerator or a high temperature oven attachment capable of providing a controlled heating/cooling of the sample from room temperature to 25 K or 1223 K, respectively, was used.

For M–T measurements, weighed quantity of the nanocrystalline sample is wrapped on the quartz securely using Teflon tape or placed in the ceramic holder attached to the high temperature quartz rod after prior the calibration using standard Ni sample. The CCR/oven is purged with high purity helium/nitrogen gas during the experiment. Magnetization was recorded at different temperatures at a constant in-plane applied magnetic field. Figure 2.12 displays a schematic diagram and photographic view of the VSM used in the present study.

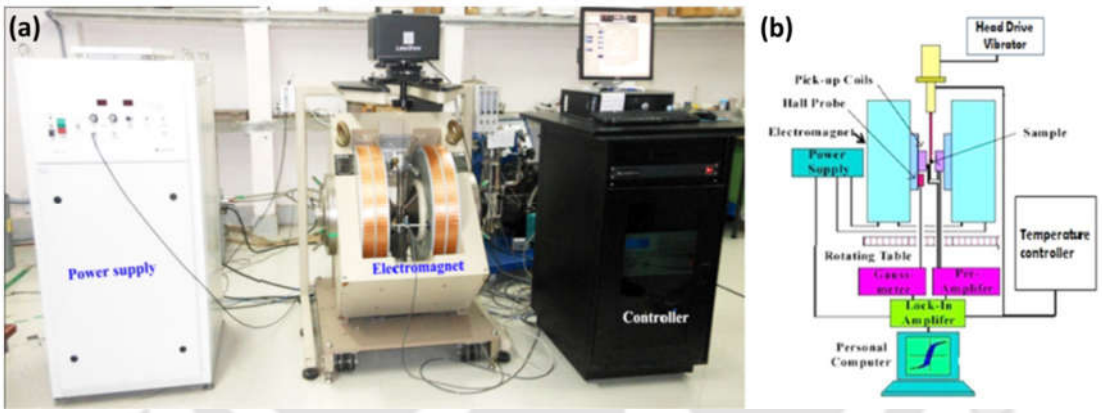

Figure 2.12: (a) Photograph of Lakeshore VSM Model 7410. (b) Block diagram of a VSM.

2.2.3.2. Electron paramagnetic resonance

Electron paramagnetic resonance (EPR) spectroscopy which was earlier referred to as electron spin resonance (ESR) is a powerful, sensitive, informative and non-destructive technique for the characterization of the electronic structure of materials with unpaired electrons. EPR is based on Zeeman effect which explains the splitting of energy level of a particle having spin ½ in a magnetic field. The energy difference between the two levels is given by

$$\Delta E = g\mu_B H \qquad (2.9)$$

where, g is the Landé g-factor, μ_B is Bohr magneton and H is the amplitude of magnetic field. Since the energy difference between the two states depends on the magnetic field, electrons at

the lower energy state can jump to the excited state at a particular value of the magnetic field. Alternatively, one can fix the magnitude of the applied field and vary its frequency. At certain value of frequency, the electrons can jump to the higher state giving rise to an absorption peak in the spectrum. At resonance,

$$h\nu = g_e \mu_B H \tag{2.10}$$

where, ν is the frequency of the magnetic field, h is Planck's constant. Neither the field nor the frequency of resonance is a unique fingerprint for a system because spectra can be obtained at different value of h or frequency satisfying Eqn. 2.10. Therefore, the g-factor is the most useful parameter for the characterization of ESR spectra.

Figure 2.13: Photographic view of ESR spectrometer (JEOL, JES-FA200).

Figures 2.13 displays photographic view of ESR used in the present study. The microwave source generates and supplies microwave at controlled frequency and power, which are transmitted to the sample cavity through a waveguide. The sample cavity is mounted in the midst of the electromagnet pole pieces perpendicular to the magnetic field, H which can be varied in a controlled way. In addition to the main magnetic field, another magnetic field which is weaker comparative to the main field is generated and superimposed on the cavity by Zeeman modulation coils. Thus, the signal response from the cavity is modulated at the Zeeman modulation frequency. The ideal way to obtain an EPR spectrum is to fix the magnitude of the magnetic field and continuously vary its frequency. However, microwave generators are tunable only to a limited range of frequency. Hence, the microwave frequency is fixed and magnitude of the magnetic field is varied. The magnetic field is swept until it reaches a point when the sample absorbs the microwave frequency and

jumps to the higher energy level. Commercial ESR spectrometer works in the frequency range from several MHz to several GHz: 1-2 GHz (L-band) and 2-4 GHz (S-band), 8-10 GHZ (X-Band), 35 GHz (Q-band) and 95 GHz (W-band). In the present investigation, we have carried out the ESR measurement on samples in powder using JEOL Spectrometer (JES-FA200) operating at X-band frequency (ν = 9.4 GHz) with 100 kHz magnetic field modulation.

2.2.3.3. Mössbauer Spectroscopy

Mössbauer spectroscopy is a versatile technique that can give very precise information about the chemical, structural, magnetic and time-dependent properties of a material [LONG71]. The principle of the experiment is illustrated in Figure 2.14. A source containing ^{57}Co nuclei provides a ready supply of excited ^{57}Fe nuclei which decay to the ground state via a gamma ray cascade including a 14.4 keV γ-ray of frequency (ν) 3.5×10^{18} Hz. This γ-ray can excite a transition in a sample, if it is absorbed resonantly by it. To do this, the γ-ray energy must match the energy gap in the sample. By moving the source at speed v, one can very slightly adjust the frequency of the γ-ray because of Doppler effect. Due to the high frequency of the γ-ray photon, the Doppler shifts can be quite significant. A velocity of v = 1 mm s^{-1} leads to a shift of νν/c ~12 MHz. Thus, one can probe any splitting in the ground state in the source or absorber nucleus which might result from magnetic or other interactions [BLUN03]. The technique would be useless if the γ ray photon emitted by the excited ^{57}Fe nucleus did not have a well-defined frequency. This is why the relatively slow decay of the ^{57}Fe nucleus is vital. The plodding 0.2 μs half-life corresponds to an uncertainty of only about 2 MHz in the frequency. A second vital feature is that the ^{57}Fe atoms are in the solid state. In order to conserve momentum, a free Fe atom would be subject to a recoil velocity ~hν/m_{Fe}c ~80 m s^{-1} which would ruin the experiment. However, a ^{57}Fe atom which is held rigidly in a solid transmits that momentum to the entire crystal. If the recoil energy is lower than a certain value, the probability of phonon emission becomes extremely small and the gamma ray can be emitted without any loss of recoil energy. This recoil-free emission and resonant absorption of γ-rays is the essence of the Mössbauer effect. The resonant absorption may be slightly shifted when the source is moving at a particular velocity. This isomer shift is due to the slight change in the Coulomb interaction between the nuclear and electronic charge distributions over the nuclear volume which is associated with the slight increase of size of the ^{57}Fe nucleus in the I = 3/2 state. Furthermore, one may observe a number of resonant absorption lines as a function of source velocity. This can be due to quadrupole splitting or

magnetic splitting. The first effect is due to the electric quadrupole moment of the excited ^{57}Fe nucleus. Although the ground state of ^{57}Fe has I = 1/2 and hence no electric quadrupole moment, the excited state of interest has I = 3/2 and nuclei with I > 1/2 can have a non-zero quadrupole moment. If the nucleus is subjected to an electric field gradient, as found in certain crystal environments, the interaction between the nuclear quadrupole moment and the electric field gradient splits the excited I = 3/2 state into a doublet, so that two lines are produced in the Mössbauer spectrum. The second effect is caused by the interaction between the nucleus and the local magnetic field. This can split the I = 1/2 ground state into a doublet, and the excited I = 3/2 into a quadruplet, leading to six possible lines in the Mössbauer spectrum (the selection rule is $\Delta m_I = 0, \pm 1$). This effect can be used to detect magnetic exchange interactions and local magnetic fields. All these shifts and splitting's are illustrated schematically in Figure 2.12. The observed splittings are typically in the range 10^7-10^8 Hz and are therefore 11 or 12 orders of magnitude smaller than the energy gap between the ground (I = 1/2) and excited state (I = 3/2) of the ^{57}Fe nucleus. Thus, one is measuring energy splitting of less than 1 μeV with a 14.4 keV photon.

The source for ^{57}Fe spectroscopy is commercially available ^{57}Co which is mounted on the shaft of a vibrator. The source is generally kept at room temperature and the absorber (sample under study) may be cooled down to liquid nitrogen or liquid helium temperatures in a cryostat. The γ-rays are detected by a scintillation counter, gas proportional counter or a semi-conductor detector. The pulses from the detector are amplified and send it in a multi-channel analyser (computer), which is synchronised with the vibrator. A constant frequency clock synchronizes a voltage waveform which serves as a reference signal to the amplifier which controls the vibrator. The difference between the monitored signal and the reference signal is amplified and drives the vibrator at the same frequency (typically, 50 s^{-1}) as the channel address advance. Each channel corresponds to a certain relative velocity and is held for a fixed time interval depending on the frequency and number of channels used. The incoming γ-counts are collected in their corresponding channels until satisfactory resolution is reached. The measured Mössbauer spectrum is analyzed using special least squares fitting programs. The Doppler velocity range required to encompass the hyperfine resonance signals generally recorded in the case of ^{57}Fe spectroscopy is less than ± 10 mm s^{-1}. For quantitative comparison of the spectra with different samples, the velocity scale must be calibrated using appropriate reference substances. For example, most researchers use magnetic α-iron as

reference absorber, which shows a well resolved sextet resulting from magnetic dipole splitting.

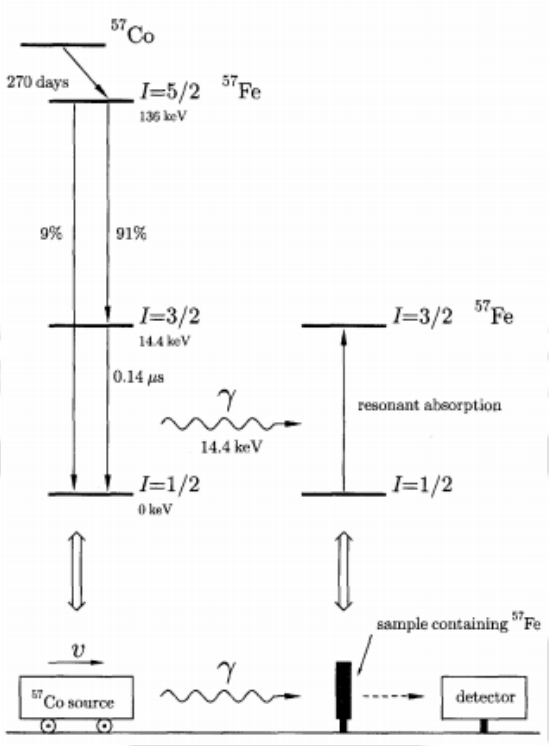

Figure 2.14: Schematic illustration of the principle of Mössbauer spectroscopy [BLUN03].

Mössbauer spectrometer built by Dr. R. Govindaraj in Indira Gandhi Centre for Atomic Research, kalpakkam, was used in the current work. The spectrometer was operated in constant acceleration mode and in transmission geometry. ^{57}Co dispersed in Rh matrix with a specific activity of 50 mC was used as the source for the Mössbauer measurements. Each Mössbauer spectrum was acquired in 1024 channels. The spectra were calibrated with a 10 μm α-Fe foil at 300 K and isomer shifts were calculated with respect to that of α-Fe at 300 K. Spectra were fitted to Lorentzian line shapes of line width Γi using a nonlinear least squares program to obtain hyperfine parameters such as isomer shift δ_i, quadrupole splitting Δ_i, and magnetic hyperfine fields (B_{hf}) experienced by relative fractions f_i of distinct ^{57}Fe absorber atoms. For carrying out Mossbauer measurements under the application of an external magnetic field parallel to the direction of γ-ray, the sample was sandwiched between two rare earth based ring magnets each of magnetic field strength close to 0.3 Tesla. Sample-magnet assembly was then placed in such a manner that the magnets are concentric with the direction of the γ-ray. The sample was placed in a variable temperature sample stage which

enabled one to make measurements temperatures down to 100 K in a controlled inert atmosphere.

2.2.4. Thermal analysis

2.2.4.1. Thermo-gravimetric analyzer

A thermogravimetric analyzer (TGA) continuously measures the mass (or weight) of a sample as its temperature is varied at a constant heating rate. A TGA consists of a sample pan which hangs off a hook and is connected to a microgram balance arm which is countered by a tare pan. The sample pan is inserted into a furnace as shown in Figure 2.15(a).

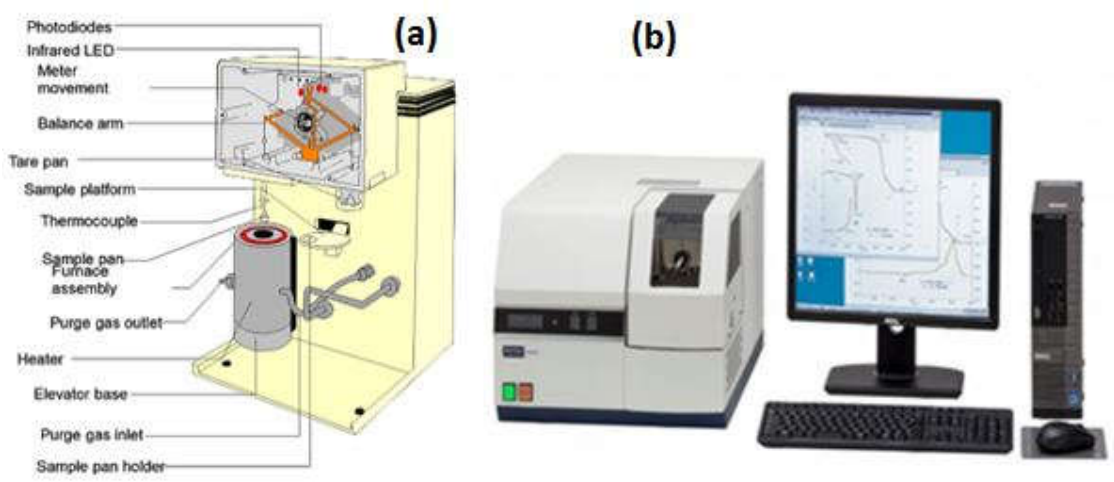

Figure 2.15: (a) Schematic diagram of a TGA. (b) Photograph of Simultaneous Thermal Analyser (NETZSCH STA 449).

The basic principle of TGA is that it records the change in the mass (or weight) of the sample as it is heated at a steady rate. This change in weight can be used to determine the thermal stability or phase change in the sample. Usually, a sample loses weight as it is heated up due to decomposition, reduction, or evaporation. Similarly, a sample could also gain weight due to oxidation or absorption. The TGA machine tracks the change in weight of the sample via a microgram balance. Temperature is monitored via a thermocouple. The TGA can also track change in weight as a function of time at a set temperature. Data can be graphed as weight percent or time versus temperature. The data produced by this lab was graphed as weight percent versus temperature. TGA output curves can be analyzed in a number of ways. If the material is stoichiometric, the molar weight of the component is burned off and can be calculated based on the weight percent lost and the total molar weight

of the material. In the current studies, a simultaneous Thermal Analyser (NETZSCH STA 449) which is a simultaneous differential scanning calorimeter cum thermogravimetric analyser was used. The instrument shown in Figure 2.15 (b) can simultaneously measure heat flow from or into the sample as well as sample weight loss or gain as a function of temperature up to 1600 K. However, the present measuremnts were restricted only to recording the TG curves of the samples during the heating cycle. Heating rate of 10 K/minute was used during all the measurements. Standard Al and Al_2O_3 pans of 40 µl and 70 µl size, respectively, were used as sample containers. The sample quantity used for this analysis was 5-10 mg. Inert atmosphere was maintained during the measurements by purging high purity argon gas.

Chapters 3, 4, 5 and 6 will describe the experimental work carried out on nanocrystalline ZnO based DMS and $CaFe_2O_4$ based ferrites using the techniques described above.

Chapter 3

INVESTIGATIONS ON NANOCRYSTALLINE ZnO OBTAINED FROM PVA/ZnO NANOFIBERS

This chapter presents investigations carried out on the effect of heat treatment on the evolution of nanocrystalline ZnO from composite PVA/ZnO nanofibers and the properties of these novel ZnO nanostructure.

As mentioned in the first chapter, RTFM has been observed in undoped wide band gap semiconductors such as TiO_2 [HONG06], ZnO [KHAL09] and MgO [BOUB10], making the phenomenon very interesting from both scientific as well as application viewpoints. However, its origin is still under debate. Of these wide band gap DMS, ZnO, has a large exciton binding energy and high solubility of TM ions which make it attractive for applications in electronic and optoelectronic devices [PARK90]. Moreover, diverse magnetic properties have been observed in this DMS [ZHAN06, RAMA06]. Since its magnetization is very low, extrinsic effects such as impurities do not influence the observed ferromagnetism. Considering the fact the dimensionality of the nanomaterial and the preparative procedure influence its properties, it is apt to investigate new forms of nanocrystalline ZnO. In this chapter, novel 1-dimensional ZnO nanostructures have been prepared by electrospinning route and the properties of the same have been investigated.

3.1. Preparation

The first step was to prepare the precursor polymer solution for electrospinning. For this, aqueous polyvinyl alcohol (PVA) solution (12 wt %) was prepared by dissolving PVA (MW ~80,000, Sigma-Aldrich) powder in appropriate amount of deionized water heated to 80 °C under constant stirring until a homogeneous solution was obtained. Then, 20 wt.% aqueous zinc acetate [Zn $(CH_3COO)_2 .2H_2O$, Merck Specialities Pvt. Ltd., India] solution was added slowly to the PVA solution with continuous stirring for 2 h to obtain a homogeneous mixture. The mixture was kept at room temperature for 4-5 h to obtain a viscous solution suitable for electrospinning. The solution was electrospun using a commercial electrospinner (NABOND NEU) under a potential difference of 16 kV, spinneret to collector distance of 12 cm and solution flow rate of 2 ml/h. The composite nanofibers ejected from the tip of the metallic syringe needle (anode) were collected on a grounded collector drum rotating at 400 r.p.m. The cross woven nanofibers were in the form of a mat (or membrane) of a few tens of micrometers thickness. As-spun nanofibers were taken either in sealed fused silica ampoules under 10^{-3} Pa or in an open alumina crucible and heated @ 4 °C/min in an electric furnace to the annealing temperature (T_A). T_A between 500 and 600 °C were used and the samples were held at each T_A for 90 minutes each. This annealing procedure based on thermos-gravimetric analysis of the as-spun samples, removed the organic matter present in the as-spun composite nanofiber samples and induced crystallization of the metal precursors into nanocrystalline ZnO.

3.2. Thermo-gravimetric analysis

The as-spun nanofibers consist of a composite of PVA and zinc acetate. In order to obtain the target compound ZnO from the precursor, heat treatment is essential. In order to understand the effect of heat treatment on the as-spun nanofibers and to optimize the heat treatment conditions, thermos-gravimetric analysis (TGA) was performed on the samples. Figure 3.1 shows the TGA plot of the as-spun sample in which the weight loss was recorded from room temperature to 800 °C at a constant heating rate at 10 °C/min. Three distinct stages of weight loss can be seen in the figure. First large weight loss is observed between 50 and 140 °C corresponding to the removal of water from the compound. Second sharp fall in weight is observed between 140 and 270 °C which represents the decomposition of PVA and organic component from the precursor salt. The final weight loss is observed between 270 and 460 °C. This shows that at temperature above 460 °C there is no organic matter in the sample and the thermal reaction to crystallize ZnO from the precursor is also complete. The residual weights of the samples were about 28% for the initial sample weight. This also shows that the aqueous and organic matter in the as-spun nanofibers is nearly 72%. Figure 3.1 provided the basis for the heat treatment carried out on the as-spun samples to obtain nanocrystalline ZnO.

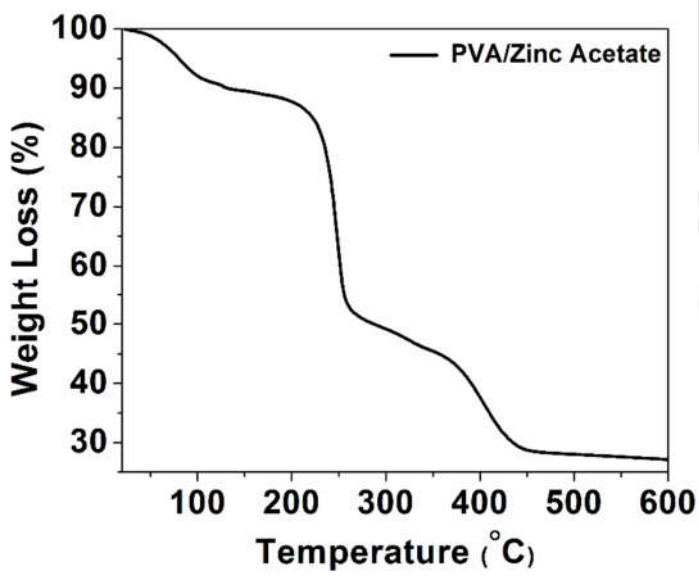

Figure 3.1: TGA plot of Zinc acetate/PVA composite nanofibers.

3.3. Structural characterization and morphology

X-ray diffraction (XRD) pattern of as-spun composite nanofibres showed amorphous features with no crystalline peaks. Figure 3.2. shows the room temperature XRD patterns of the composite nanofibers annealed at 500 °C, 550 °C and 600 °C for 90 minutes each. It can be seen that all the Bragg peaks present in the XRD patterns could be indexed to hexagonal wurtzite structure of ZnO (JCPDS file # 36-1451) which establishes the phase purity of the ZnO samples. The lattice parameters, a = 0.3248 nm and c = 0.5211 nm, calculated for the sample heat treated at 500 °C are in agreement with the values of a = 0.3256 nm, c = 0.5218 nm reported for ZnO nanoparticles in the literature [YLIU09].

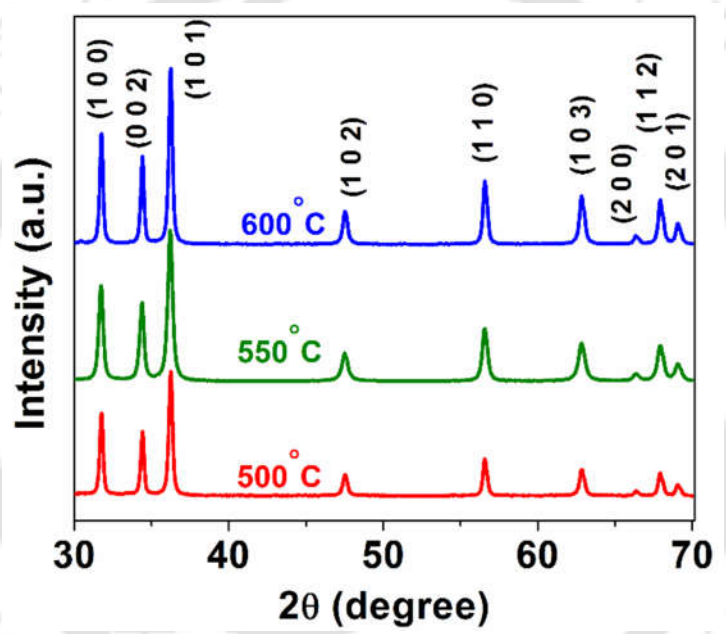

Figure 3.2: XRD patterns of electrospun composite nanofibers heat treated at T_A = 500, 550 and 600 °C for 90 minutes each in air.

Table 3.1 displays the lattice parameters and unit cell volume of ZnO obtained by heat treatment of the nanofibres at different T_A's. Designations ZnO_500, ZnO_550 and ZnO_600 denote the final product after heat treatment at respective T_A. Effect of heat treatment conditions on the structural parameters of the ZnO crystallites can be understood from the data presented in the table. The broadened reflections observed in XRD patterns indicate that the crystallites are strained and sub-micron in size. Williamson-Hall method [AKZA11] described in chapter 2 was used to calculate the average crystallite size (d_{av}) and strain (ε)

present in the samples and the results are tabulated in Table 3.1. d_{av} increases as T_A is increased from 500 to 600 °C, which is expected as the nucleated nanocrystallites grow in size when heat treated at higher temperatures. Microstrain increases moderately when heated from 500 to 550 °C, but shows a higher value at 600 °C. If the ZnO crystallites were well isolated, the microstrain should decrease when heat treated at higher T_A. The observation of a contrary trend in these samples shows that the crystallites are interconnected and hence impose considerable strain on each other when they grow at higher T_A.

Table 3.1: Average crystallite size (d_{av}), microstrain (ε), lattice parameters (a, c) and unit cell volume (V) of ZnO nanostructure in heated treated nanofibres.

Sample ID	d_{av} (nm)	ε ($\times 10^{-3}$)	a (nm)	c (nm)	V (nm)^3
ZnO_500	35	1.22	0.32484	0.52058	0.04760
ZnO_550	54	1.29	0.32497	0.52062	0.04761
ZnO_600	89	2.36	0.32527	0.52115	0.04775

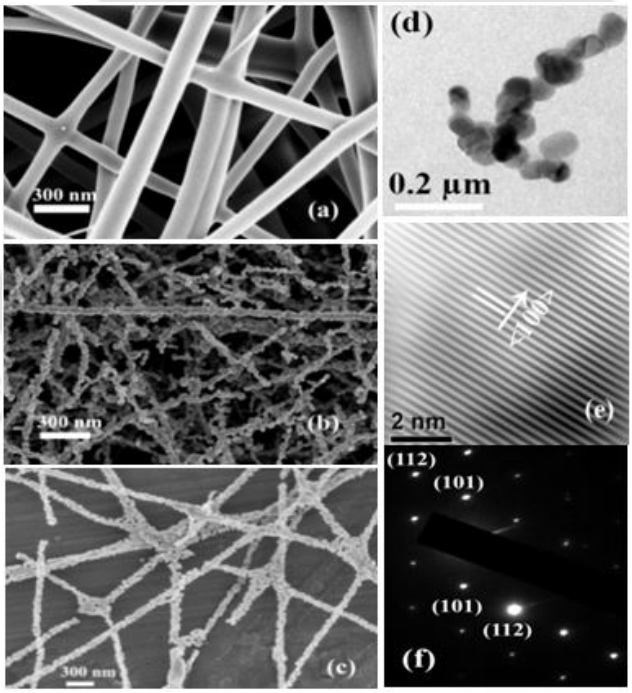

Figure 3.3: FESEM images of (a) as spun, (b) 550 °C, and (c) 600 °C air annealed nanofibers. (d) Low resolution TEM image, (e) HRTEM image of lattice fringes and (f) SAED pattern of 550 °C annealed sample are also displayed.

FESEM micrograph (Figure 3.3(a)) of the as-spun composite nanofibrous membranes indicate homogenous and interconnected fibrous network with no beads or string formation. The as-spun nanofibers are smooth and bead-free because of the amorphous nature of the zinc acetate/PVA composite and the optimal electrospinning conditions, respectively. However, after annealing at 550 °C, the surface of the nanofibers turns rough and the fiber diameter decreases as a consequence of the removal of PVA and the conversion of the Zn salt into ZnO with wurtzite structure as depicted in Figure 3.3(b,c). Average diameter of the individual fibers was estimated from multiple FESEM images using Image J™ software. The average diameter of the as-spun fibers was in the range of 100-120 nm. Upon heat treatment at 550 °C, fiber diameter shrank dramatically to diameters ranging from 50-60 nm as depicted in Figure 3.3(b). Nanofibres annealed at 600 °C also show a rough surface, but the fiber diameter increased to 90-100 nm [*cf.* Figure 3.3(c)]. The increase in the fiber diameter is a consequence of an increase in the average crystallite size upon heat treatment at 600 °C. Figure 3.3(d) shows the TEM images of the 550 °C annealed sample under low magnification which reveals a connected bead-like continuous and inter-twinned 1-d nanostructure as indicated by the microstrain data. This shows that ZnO crystallites initially nucleate as spherical crystallites. However, due to the restricted growth geometry and high concentration of nucleates, the crystallites merge and grow as interconnected beads leading to a weakly bound but extended 1-d ZnO nanostructure. Such a variation in the nanostructure is special and typical of the electrospun ZnO obtained in this work. HRTEM lattice image shown in Figure 3.3(e) clearly illustrates nanocrystalline nature of ZnO. The inter-planar *d*-spacing of the crystal plane shown was calculated to be 0.28 nm which corresponds to the lowest order (100) plane of wurtzite ZnO. The selected area electron diffraction (SAED) pattern shown in Figure 3.3(f) confirms the XRD results presented earlier *i.e.*, the presence of single phase ZnO in wurtzite structure.

3.4. Optical Properties

Ultraviolet–visible (UV-vis) absorption spectra of the annealed samples have been used to find the possible modifications in the band structure of ZnO. Figure 3.4 shows the room temperature UV-vis spectra of undoped samples obtained by annealing at different temperature. The peak in the absorption data can be related to the wavelength corresponding to band edge (λ_g) from which the band gap (E_g) can be estimated. Though this is not an accurate method for determining the band edge, it provides a reasonable estimate of the same

for powder samples to which the Tauc relation cannot be applied without knowledge of the path length (sample thickness). Band gap estimated from the plots shows a shift for samples annealed at different temperatures. The peaks are red shifted with respect to the 500 °C sample (380 nm) and the exciton absorption is observed at 382 and 386 nm for 550 °C and 600 °C, respectively. Since the nanostructure sizes are larger than excitonic Bohr radius of ZnO, size effect is unlikely to be the cause for the observed change in bandgap energy with annealing temperature. Hence, this band gap shift is due to the effect of annealing at elevated temperatures which increases the ZnO crystallite size.

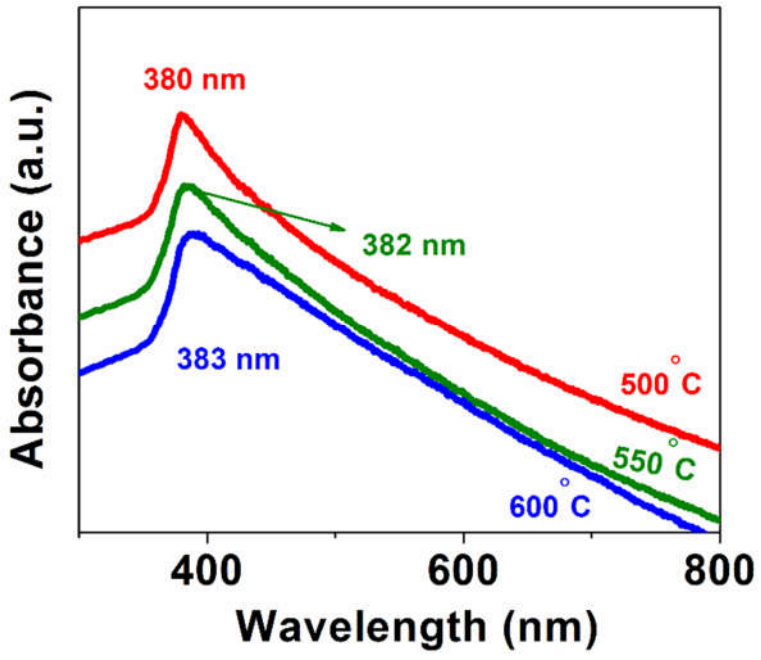

Figure 3.4: UV of ZnO nanofibers annealed at 500 °C, 550 °C and 600 °C in air.

3.5. Magnetic Properties

The as-spun sample with amorphous structure showed diamagnetic nature and annealing up to 400 °C did not induce ferromagnetism in the sample. This is understandable when one looks at the TGA results which suggest that conversion of the precursors to ZnO crystallites is complete only after 460 °C. Hence, the samples were annealed between 500-600 °C for 90 minutes each to induce crystallization and possible ferromagnetism in the sample. Temperature dependent magnetization of 550 °C annealed sample recorded under field-cooled (FC) condition with an applied magnetic field of 1.5 kOe and zero field-cooled (ZFC) condition is shown in Figure 3.5(a). It can be seen from the figure that the annealed samples

are weakly ferromagnetic with low magnetization. Moreover, the M_{ZFC}-T and M_{FC}-T curves overlap and exhibit a nearly linear decrease in magnetization up to 300 K with no transition to paramagnetic state up to 300 K. Such bhaviour has also been noted by others in ZnO nanoparticles and thin film [PHAN13, XING11].

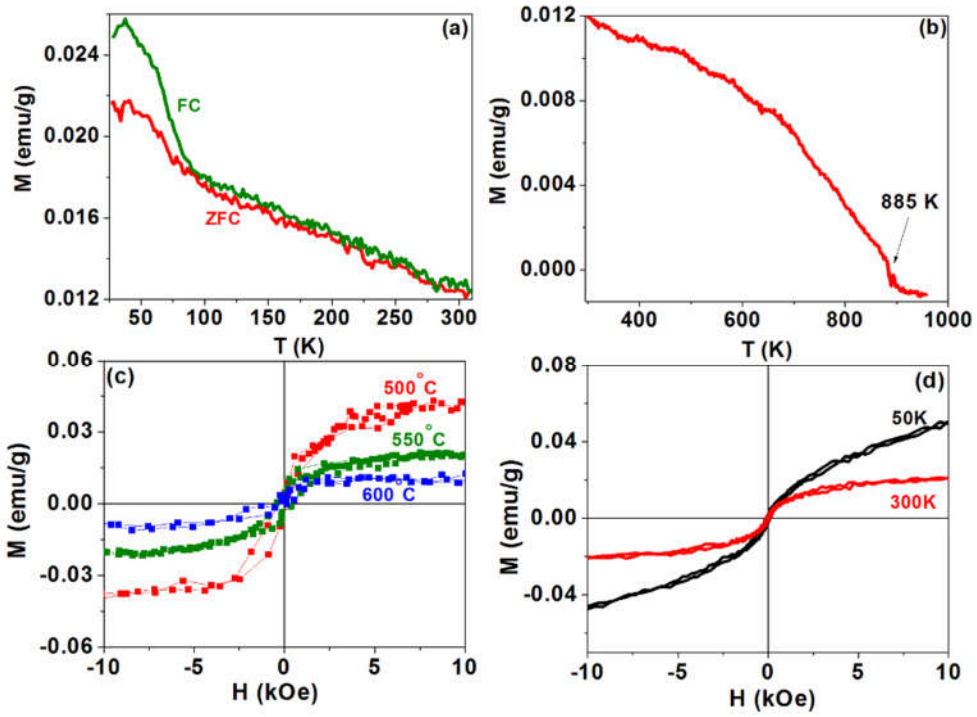

Figure 3.5: (a) ZFC-FC magnetization curve and (b) M-T curve of 550 °C annealed sample (FC curved recorded under 1.5 kOe field). (c) Room temperature M-H curves of samples annealed in air. (d) M-H curves of 550 °C air annealed sample recorded at 50 and 300 K.

The M-T curve of the sample recorded from 300 K to 950 K under the same applied field showed a ferromagnetic to paramagnetic transition at T_C ~ 885 K, which is far above room temperature (cf. Figure 3.5(b)). A comparison with reports in the literature on undoped ZnO nanostructures shows that highest T_C reported is 740 K [XING11]. In comparison, the present studies on electrospun ZnO nanowires show a much higher T_C which would be useful for practical applications. Variation of magnetization of the samples with applied field was recorded at room temperature. The field dependent magnetization curves of the 500, 550 and 600 °C annealed samples are shown in Figure 3.5(c), all the samples exhibit magnetic hysteresis loop at room temperature with saturation magnetization. Interestingly, 500 °C

annealed sample shows the maximum magnetization (M_S = 0.039 emu/g) obtained after subtraction of diamagnetic contribution while the 600 °C annealed sample shows the lowest magnetization (M_S = 0.007 emu/g) value. This shows that magnetization decreases as the annealing temperature is increased above 500 °C. Reduction in ferromagnetism with increased annealing temperature can be correlated with the reduction in V_o^+/V_o^{++} ratio at these temperatures. The observed coercive field (H_C) and remnant magnetization (M_r) are 255 Oe and 0.005 emu/g for the 500 °C annealed sample. The corresponding values are 340 Oe and 0.002 emu/g for the 600 °C annealed sample. M-H data of 550 °C annealed samples recorded at 50 K is shown in Figure 3.3(d). At 50 K, the magnetization did not exhibit saturation, which indicates paramagnetic contribution from the conduction electrons [SUND06].

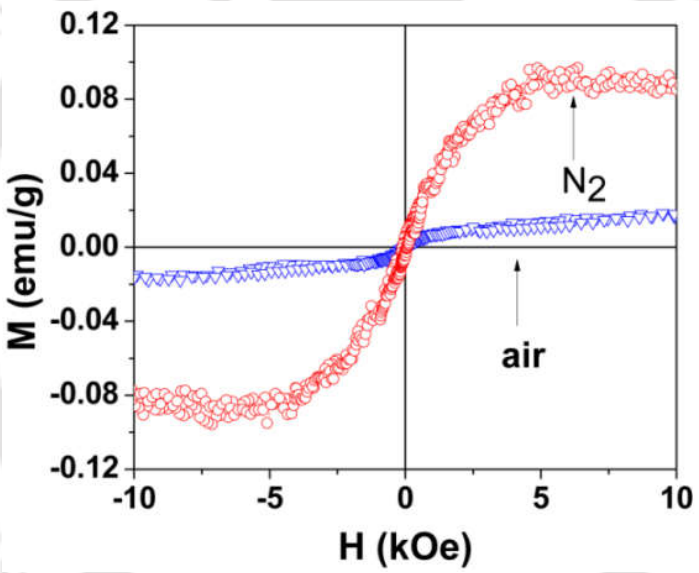

Figure 3.6: Room temperature M-H curves of ZnO nanofibers annealed at 550 °C for 90 minutes in air and nitrogen environment.

In order to understand the evolution of magnetization, samples were annealed at 550 °C under reduced ambient pressure of 10^{-3} Pa for 90 minutes. The vacuum annealed sample showed higher magnetization of 0.056 emu/g with respect to air annealed sample (0.022 emu/g). The M-H curve of sample annealed at 550 °C for 90 minutes in nitrogen atmosphere (*cf.* Figure 3.6) exhibited a higher saturation magnetic moment (0.08 emu/g) as compared to the air annealed sample. These observations indicate that oxygen vacancy is primarily responsible for the observed ferromagnetism in these samples. At higher annealing temperatures, oxygen vacancy is less as compared to lower annealing temperature and hence

magnetization decreases at higher temperatures. Further analysis of the defect states in the samples could throw more light on this proposal.

3.6. Defects analysis

Magnetization studies on the 1-d ZnO samples not only show RTFM, but also higher magnetization when annealed under oxygen environment. In order to understand these results, Raman, photoluminescence and EPR spectroscopy studies were carried out on the samples.

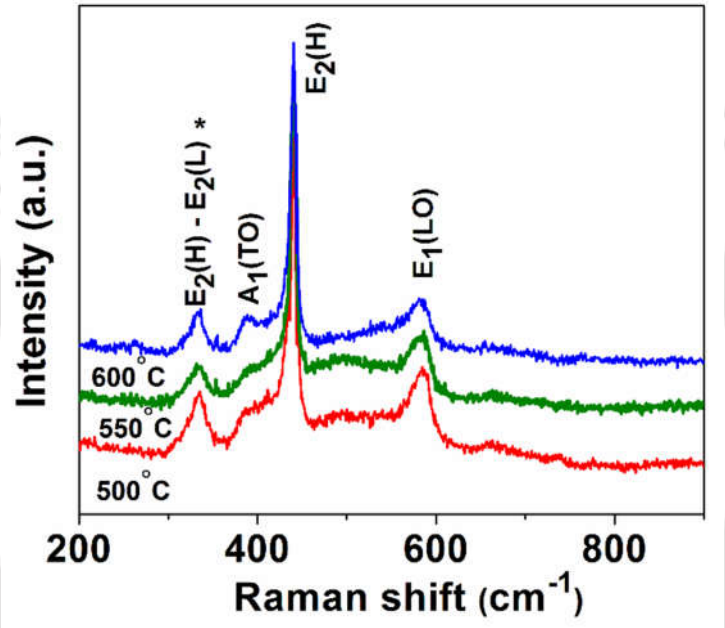

Figure 3.7: Raman spectra of PVA/ZnO nanofibers annealed at 500 °C, 550 °C and 600 °C in air. Raman spectrum of sample annealed at 550 °C in nitrogen atmosphere is also shown.

Raman scattering is one of the most effective tools for studying the crystallinity and confirming the presence of defect states in the crystal structure. Figure 3.7 shows room temperature Raman spectra of all the annealed samples in the spectral range of 200–800 cm^{-1}. The strong peak observed at 437 cm^{-1} is the E_2 (H) phonon mode which is characteristic of wurtzite ZnO and arises due to the vibration of oxygen atoms. The peak located at 385 cm^{-1} corresponds to A_1(TO) mode and the peak at 330 cm^{-1} corresponds to E_2(H)- E_2(L) mode. The peak located at ~581 cm^{-1} [E_1(LO)] is attributed to O-vacancy defects present in the crystal [MAHA74, PRAD04]. The decrease in the intensity and the broadening of the E_1(LO) peak with increasing temperature indicate a variation in defect concentration in ZnO with temperature as proposed earlier [SCHW04]. In the case of samples annealed in nitrogen

atmosphere, higher intensity of E_1(LO) peak is observed as compared to the sample annealed in air at the same annealing condition, which shows that the defect concentration is higher in the former. It is evident that annealing at higher temperatures and annealing in nitrogen environment induced more oxygen defects in these nanostructures. It is obvious that magnetization in this sample is related to the oxygen defects in the samples.

Photoluminescence is an effective tool to observe defect state present in sample. Figure 3.8 displays the PL spectra of air annealed samples. All the spectra exhibit a relatively sharp UV emission peak centered at 385 nm and a broad band in the visible range. The UV band edge emission is attributed to free excitonic emission of ZnO and the broad emission peak to intrinsic defect arising due to radiative recombination of photo-generated holes with electrons occupying the singly ionized oxygen vacancy. The peak position of UV band edge emission position remains the same for all the samples but its intensity shows a dependence on annealing temperature. Figure 3.9(a-d) show dual Gaussian profile fitting performed on the broad emission peak. It can be noticed that the broad band could be resolved into two overlapping peaks, one centered at ~505 nm (green) and the other at ~585 nm (yellow). The green emission is generally ascribed to singly ionized oxygen vacancies (V_o^+) [YLIN09, WLIU11]. This peak is attributed to the recombination of electrons trapped in singly ionized oxygen vacancies which are paramagnetic and capable of inducing ferromagnetism. The yellow emission band is attributed to doubly occupied vacancy (V_o^{++}). It is known that V_o^{++} is a shallow donor with spin-zero ground state which cannot induce ferromagnetism in ZnO [COEY07].

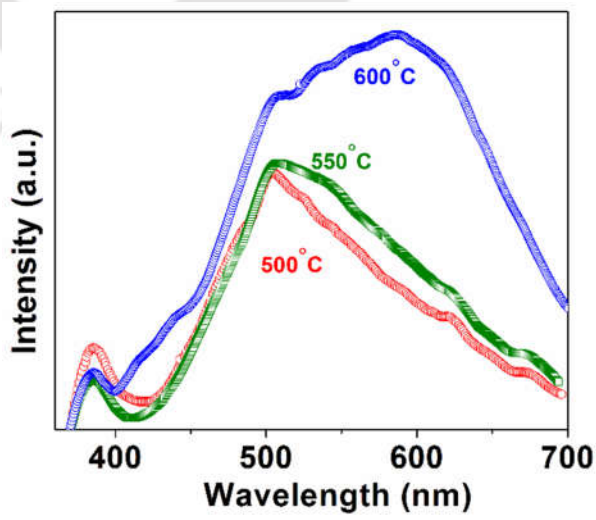

Figure 3.8: PL spectra of ZnO nanofibers annealed at 500 °C, 550 °C and 600 °C in air.

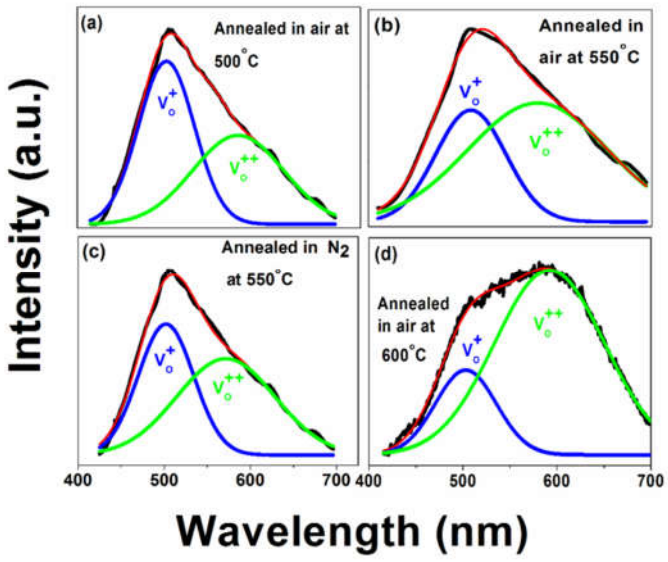

Figure 3.9: Double Gaussian profile fits to the broad band in PL spectra of samples annealed at different temperatures in air and nitrogen atmospheres, respectively.

Figure 3.10 shows that the concentration of V_o^+ and V_o^{++} defects vary with annealing temperature and with annealing environment. The plot captures the variation of the ratio between the peak areas of green and yellow bands (V_o^+ / V_o^{++}) obtained by double Gaussian fits to the broad band in the visible region. It is clear from the figure that with increasing annealing temperature, V_o^+ defect concentration decreases and V_o^{++} defect concentration increases. The high V_o^+ defect concentration in the sample annealed in nitrogen environment is also evident from the figure. So, the defects present in the undoped 1-d ZnO samples have a direct influence on the observed ferromagnetic properties. It is now important to see whether any paramagnetic defects are present in the sample.

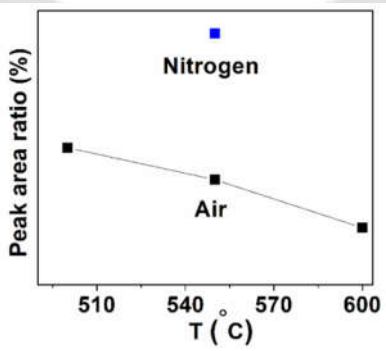

Figure 3.10: Peak area ratio of defect concentration (V_o^+/V_o^{++}) as a function for annealing temperature for samples annealed in air and nitrogen environments.

EPR is a very useful technique for measuring paramagnetic defects in a material. Point defects possible in undoped ZnO are Zn vacancy or O vacancy or their interstitials. Various research groups have investigated EPR signals from ZnO. The low field EPR signal at g value close to 2.015 or 2.002 [GALL74] is assigned to Zn vacancy and high field EPR signal at g = 1.9945 and 1.9960 [GRAC02] is assigned to singly ionized oxygen vacancy. It is well known that the EPR absorption originates from unpaired electrons. Generally, face bound radicals such as OH, CH_3 contain unpaired electron which may give rise to EPR signal. In the present studies, as the composite nanofibers were annealed above 460 °C, single (wurtzite) phase of ZnO forms and face bound radicals present in the polymer decreases. Hence, the EPR signal in the annealed samples is only related to the ZnO phase. Figure 3.11 shows the EPR spectra of 500 °C, 550 °C and 600 °C air annealed samples recorded at room temperature. It is clearly observable that all samples show a single EPR signal which suggests the presence of the same kind of paramagnetic defect in all samples. The g values corresponding to the EPR absorption obtained from the graph are 1.996, 1.994 and 1.983 for the 500 °C, 550 °C and 600 °C air annealed samples, respectively. Thus, the EPR signal at g ≈ 1.99 observed in all the samples signifies that the singly ionized oxygen (V_o^+) vacancy is the only observable defect present in these structures. This type of EPR signal is believed to be a characteristic feature of RTFM in undoped ZnO [KAKA97].

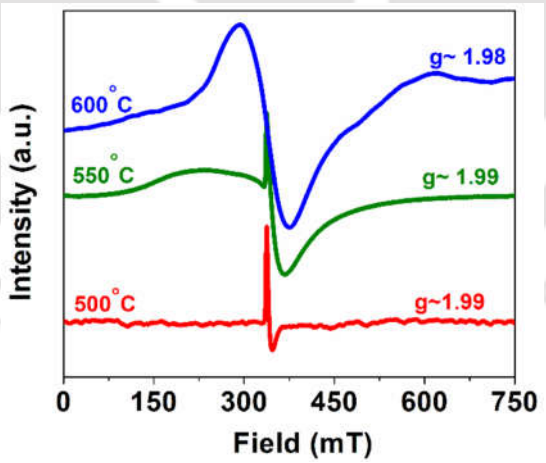

Figure 3.11: EPR spectra of ZnO nanofibers annealed at 500°C, 550°C and 600°C.

The above analyses clearly establish that the observed ferromagnetism in undoped 1-d ZnO nanostructures obtained by electrospinning route is a completely intrinsic property and is due to singly ionized oxygen vacancy (V_o^+) present in the sample.

3.7. Summary

1-d undoped ZnO nanostructures consisting of interconnected ZnO beads have been prepared by electrospinning aqueous PVA solution containing ZnO precursors followed by annealing at temperatures between 500 and 600 °C for 90 minutes.

- XRD patterns reveal that single phase wurtzite structure without any impurity phases was obtained in all the samples after annealing.
- RTFM observed in all annealed samples.
- Magnetization value decreased upon increasing annealing temperature from 500 °C to 600 °C in air.
- Magnetization was higher for the sample annealed in nitrogen environment as compared to air annealed sample at same conditions.
- Raman studies of the annealed samples showed that O vacancy is present in the annealed samples and the intensity of vacancy related peak decreased with increasing annealing temperature.
- The peak located at visible region in PL spectra of the samples which could be resolved into V_o^+ and V_o^{++} indicated that O vacancies are present in the sample and the ferromagnetic V_o^+ defect concentration could be related to the observed variation in the magnetization of the samples.
- EPR studies established that the sole absorption peak at g ~ 1.99 confirmed that single ionized oxygen vacancy is the sole paramagnetic defect in the samples.

Thus, the systematic study performed shows that single ionized oxygen vacancies is responsible for the observed RTFM in this novel undoped 1-d ZnO nanostructures obtained by electrospinning route. Very high T_C of 885 K obtained shows the potential of electrospun ZnO nanostructures for device applications.

Chapter 4

EFFECT OF ANNEALING ON Mg AND Co SUBSTITUTED ZnO NANOFIBERS

This chapter presents investigations carried out on effect of substitution of Mg, Co on the evolution of PVA/ZnO nanofibers and characterization of the same.

ZnO nanostructures have been studied extensively as pointed out in the first chapter. In this chapter, preparation and characterization of novel 1-dimentional nanostructures of ZnO containing Mg and Co are reported.

4.1. Mg substituted ZnO nanostructures:

Wide band gap semiconductors with direct band gap of ~3.36 eV and large exciton binding energy of 60 meV are of immense contemporary research interest due to their interesting intrinsic properties and prospective device applications [DJUR12]. It is now realized that doping with appropriate cations is a better strategy for tuning the bandgap of these nanostructured semiconductors rather than tailoring the size of the nanocrystalline semiconductor. Here, Mg has been chosen as a dopant despite being a non-magnetic TM because it has been pointed out that large enhancement in band gap can occur in ZnO upon doping it with Mg [MAKI01]. Moreover, the wider band gap of MgO (7.3 eV) provides more scope for band gap enhancement in Mg^{2+} doped ZnO, which can yield materials suited for fabricating light-emitting devices operating in a wider wavelength region. Mg doped ZnO nanostructures prepared by electrospinning route have not been well explored so far. Hence, this study would help us in assessing the potential of Mg^{2+} doped novel 1-dimensonal ZnO for newer applications.

4.1.1. Preparation

Aqueous polyvinyl alcohol (PVA) solution (12 wt.%) was first prepared by dissolving PVA (MW ~80,000, Sigma-Aldrich) powder in appropriate amount of deionized water heated to 80 °C under constant stirring until a homogeneous solution was obtained. Then, 20 wt.% aqueous zinc acetate [Zn $(CH_3COO)_2 .2H_2O$, Merck Specialities Pvt. Ltd., India] solution was added slowly to the PVA solution with continuous stirring for 2 h to obtain a homogeneous mixture. Finally, appropriate (0 – 8wt.%)amount of magnesium chloride was added to the mixture. The mixture was kept at room temperature for 4-5 h to obtain a viscous solution suitable for electrospinning. The solution was electrospun using a commercial electrospinner (NABOND NEU) under a potential difference of 15 kV, spinneret to collector distance of 12 cm and solution flow rate of 0.8 ml/h. The composite nanofibers ejected from the tip of the metallic syringe needle (anode) were collected on a grounded collector. To remove the organic matter in PVA/zinc acetate and PVA/zinc acetate/magnesium chloride composite

nanofibers and to convert the metal salts into crystalline metal oxide nanofibers, the as-spun samples were annealed in air at 650 °C for 3 h.

4.1.2. Thermo-gravimetric analysis

Figure 4.1 shows the TG curves of as-spun PVA/zinc acetate and 8 wt.% Mg doped PVA/zinc acetate nanofibres recorded from ambient temperature to 800 °C under a constant heating rate at 10 °C/min. It is evident from the TG curves that both samples undergo the same three stages of weight loss. The first weight loss observed between 50 and 140 °C corresponds to the removal of water from the compound. The second sharp fall in weight recorded between 200 and 270 °C corresponds to the decomposition of PVA and removal of organic components from the fibers. The final weight loss observed between 270 and 490 °C can be interpreted as due to the oxidation and conversion of zinc acetate to ZnO with the removal of compositional residues. The residual weight of the samples was about 25% for all samples which represents the final amount of ZnO and Mg doped ZnO nanofibers produced after removal of all organic components from the fibers. Since no perceptible weight loss was observed beyond 600 °C, 650 °C was chosen as annealing temperature for converting the as-spun fibers into ZnO nanowires in this study.

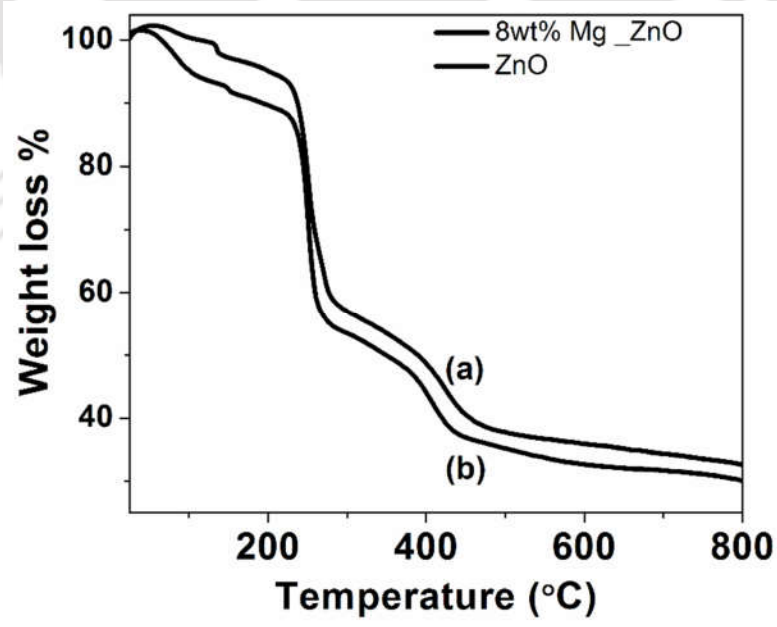

Figure 4.1: TGA thermogram of undoped and 8wt.% Mg doped Zinc acetate/PVA composite nanofibers.

4.1.3. Structural characterization and morphology

Figure 4.2(a)-(h) show FESEM images of ZnO/PVA composite nanofibers both in as-spun and annealed conditions. External electrospinning parameters (flow rate, needle to collector distance, voltage) were kept identical for all samples. However, internal parameters like solution (electrical) conductivity, viscosity and surface tension which depend on the amount of metal salts in the solution influence the fiber morphology. It can be seen that the surface of as-spun fibers both undoped zinc acetate/PVA and zinc acetate/PVA/Magnesium chloride is smooth and bead free, because of amorphous zinc acetate/PVA and zinc acetate/PVA/Magnesium chloride. Undoped ZnO/PVA nanfibers have an average diameter of ~222 nm. Average diameter reduces to ~154 nm for nanofibers containing 8 wt.% Mg^{2+}. This reduction in diameter is due to the presence of magnesium which changes the internal properties like electrical conductivity and viscosity of the solution. These parameters have direct influence on the fiber diameter. It can be seen that upon annealing at 650 °C, the average diameters of all the nanofibers shrink drastically.

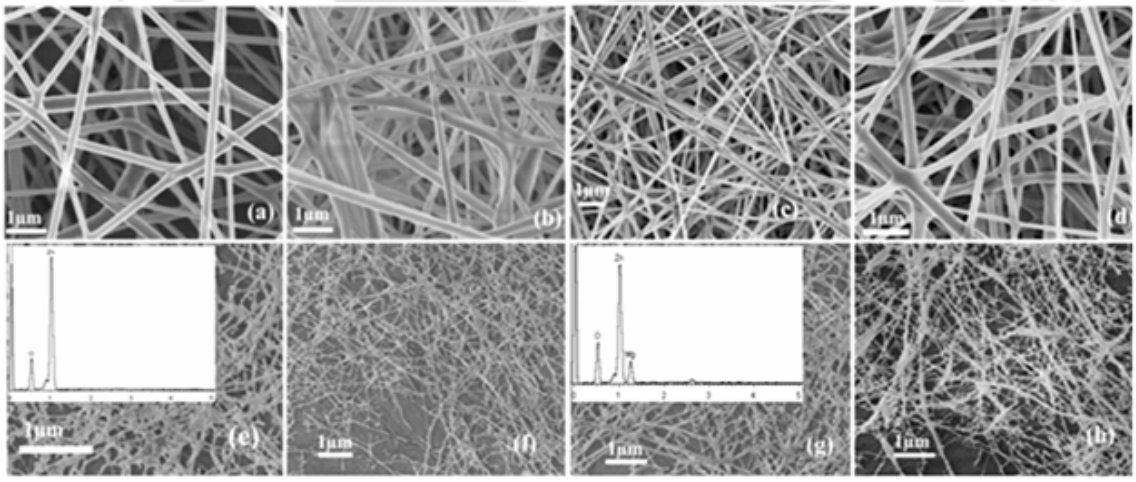

Figure 4.2: FESEM images of (a) undoped, (b) 3 wt.% Mg doped, (c) 5 wt.% Mg doped and (d) 8 wt.% Mg doped PVA/ZnO as-spun nanofibers. Morphology of annealed (e) undoped, (f) 3 wt.% Mg doped, (g) 5 wt.% Mg doped and (h) 8 wt.% Mg doped PVA/ZnO nanofibers. EDS spectra of undoped and 5 wt.% Mg doped samples are shown as insets in frames (e) and (g) respectively.

The shrinkage observed in fiber diameter is due to the removal of PVA from fibers and conversion of metal salts to metal oxides. FESEM images of annealed nanofibers exhibit a rough surface due to the formation of 1–dimensional metal oxide nanocrystalline structure

from the metal salt precursors. Insets in Figure 4.2(e) and 4.2(g) show the EDS spectra obtained for two specimens which confirm the presence of Mg in doped sample. As-spun samples exhibited predominantly amorphous nature due to the presence of weakly crystalline PVA and unreacted metal salts but annealed samples exhibited crystalline nature because of transformation of metal salts into crystalline metal oxide.

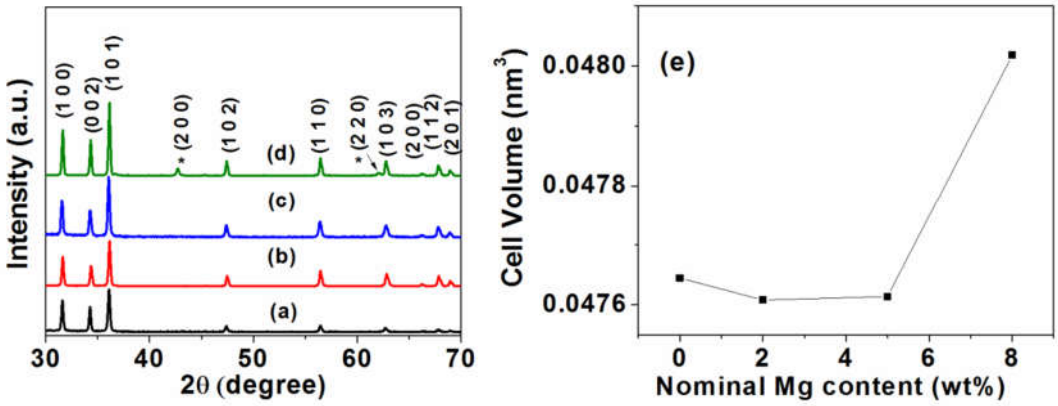

Figure 4.3: XRD patterns of annealed (a) undoped, (b) 3 wt% Mg-doped, (c) 5 wt% Mg-doped, (d) 8 wt% Mg-doped ZnO nanofibers. (e) Variation of unit cell volume with Mg concentration.

The crystal structure of the undoped and Mg^{+2} doped samples were examined by XRD at room temperature in the angle (2θ) range from 30° to 70°. As synthesized samples did not show any crystalline features because of presence of metal salts and polymer in unreacted form but the samples annealed at 650 °C for 3 h. in air exhibited crystalline nature indicating the transformation of metal salts to metal oxide crystallites. Figure 4.3 shows that XRD patterns of heat treated ZnO nanofibers. It can be observed that undoped ZnO exhibits single phase hexagonal wurtzite structure (JCPDS file # 36-1451) without any impurity phase. Single (wurtzite) phase structure was also observed in samples with Mg content up to 5 wt.%. However, sample with 8 wt.% Mg exhibited two extra reflections corresponding to (2 0 0) and (2 2 0) reflections of cubic MgO [AYKU13]. Hence, single wurtzite phase of ZnO is retained without noticeable precipitation of cubic MgO phase up to 5 wt.% Mg doping in ZnO. With increase in Mg^{2+} content in ZnO, the intensity of the reflections increases which indicates an improvement in crystallinity. Lattice constant calculated from the XRD patterns shows that the *a*-axis length increases slightly whereas the *c*-axis length decreases slightly with increase in Mg^{2+} content in ZnO. This is due to Mg atoms (with atomic radius of 145 pm) replacing the Zn atom (of atomic radius 142 pm) at the centre of the unit cell along the *c*-

axis. A pictorial view of ZnO and $Mg_xZn_{1-x}O$ hexagonal unit cells can be found elsewhere [AYKU13]. However, the overall change in unit cell volume is very small with doping due to the nearly equal atomic radius of Zn and Mg atoms. Here, figure 4(e) shows the variation of volume of the unit cell with Mg substitution in the ZnO structure. Williamson-Hall method [CULL13] was used to calculate the average crystallite size (d_{av}) and microstrain (ε) present in the samples using Eqn. 2.5. Table 4.1 shows that both d_{av} and ε decrease with increase in Mg doping. This is interesting since one can control the crystallite size of this ZnO nanostructure with appropriate Mg doping.

Table 4.1

Average crystallite size (d_{av}), microstrain (ε) and unit cell parameters of heat treated ZnO nanostructures with different Mg content.

Sample ID	d_{av} (nm)	ε ($\times 10^{-3}$)	*a* (nm)	*c* (nm)	*V* $(nm)^3$
ZnO	110	1.75	0.32484	0.52152	0.047645
3wt%Mg_ZnO	101	1.61	0.32484	0.52108	0.047608
5wt%Mg_ZnO	85	1.55	0. 32514	0.52020	0.047614
8wt%Mg_ZnO	81	1.12	0. 32614	0.52137	0.048018

4.1.4. Defect Analysis

Since this work attempts to understand the role of defects on the properties of nanocrystalline ZnO based samples, micro-Raman studies were carried out on the samples. Figure 4.4 represent the room-temperature Raman spectra of undoped and different concentration Mg^{+2} doped ZnO nanofibers annealed at 650 °C for 3h. in air. The origin of Raman spectra in Nanocrystalline ZnO has already been discussed in chapter 1, section 1.2.3. Using this notation, the Raman peak at 437 cm^{-1} observed in all the spectra corresponds to the Raman active $E_2(H)$ phonon mode of wurtzite hexagonal ZnO arising due to vibration of oxygen atoms. It can be observed from the spectra that the intensity of the $E_2(H)$ phonon mode decreases with increasing Mg^{+2} doping because of the presence of cubic MgO phase in hexagonal ZnO structure. The peak located at 330 cm^{-1} corresponds to E_{2H}-E_{2L} phonon mode which is due to the multiphonon scattering process. The other peak located at ~581 cm^{-1} is

assigned as E_1(LO) which can be attributed to O-vacancy defects present in the crystal [PRAD04].

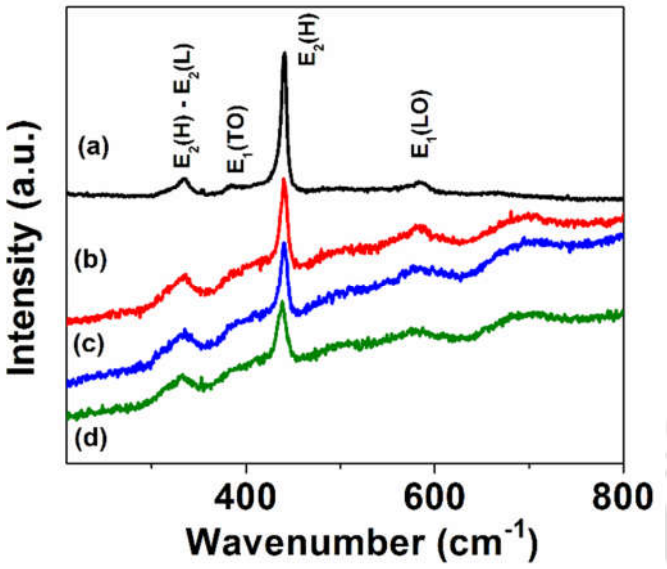

Figure 4.4: Raman spectra of ZnO nanowires containing (a) 0 wt.%, (b) 3 wt.%, (c) 5 wt.% and (d) 8 wt.% Mg.

As the next step, PL spectra were recorded for the samples. Figure 4.5 illustrates the PL spectra of all air annealed samples. All the spectra exhibit a relatively sharp UV emission peak centered at 385 nm and a broad band in the visible range which appears to be the signature of nanocrstalline ZnO. As described in the previous chapter (section 3.4), room temperature UV emission peak is attributed to near band edge emission of ZnO or recombination of excitonic centres, and the broad emission peak in the visible region to intrinsic defect arising due to radiative recombination of photo-generated holes with electrons occupying the singly ionized oxygen vacancy. It can be seen that increasing Mg^{2+} doping concentration from 0-8wt.%, shifts the ultraviolet band edge emission peak towards blue region. This indicates that Mg^{2+} substitutes for Zn^{2+} and in the process increases the band gap energy of the system. Since the atomic radii of Zn and Mg^{+2} are comparable, they can substitute each other during alloying. The broad emission peak in the visible region is due to the recombination of photo-generated holes with the electrons belonging to oxygen vacancy state [VANH96]. Considering the broad feature of the visible PL band its strong intensity dependence on Mg concentration, Gaussian profile analysis was carried out on this part of the PL spectra of the samples.

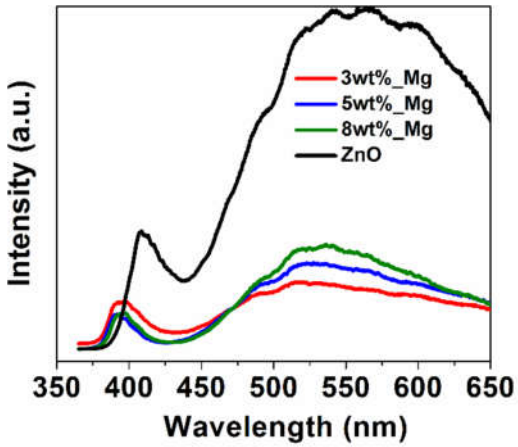

Figure 4.5: PL spectra of ZnO nanowires with different amounts of Mg.

Figure 4.6(a) shows double Gaussian peak fitting of the visible emission band of the PL spectra. The broad band could be resolved into two overlapping peaks, one centered at ~510 nm (green) and the other at ~605 nm (yellow). As discussed in the previous chapter, the green emission is generally ascribed to singly ionized oxygen vacancies (V_o^+) and the yellow emission band is attributed to doubly occupied vacancy (V_o^{++}). Figure 4.6 (b) captures the variation of the peak areas of green and yellow bands obtained by fitting double Gaussian profiles to the broad band in the visible region. It is clear from the figure that upon Mg doping, there is drastic decrease in the both types of oxygen vacancies. With increase in Mg doping concentration, there is a slight but noticeable decrease in the amount of oxygen defects. Thus, it is evident that Mg doping in 1-d ZnO quenches the oxygen vacancies.

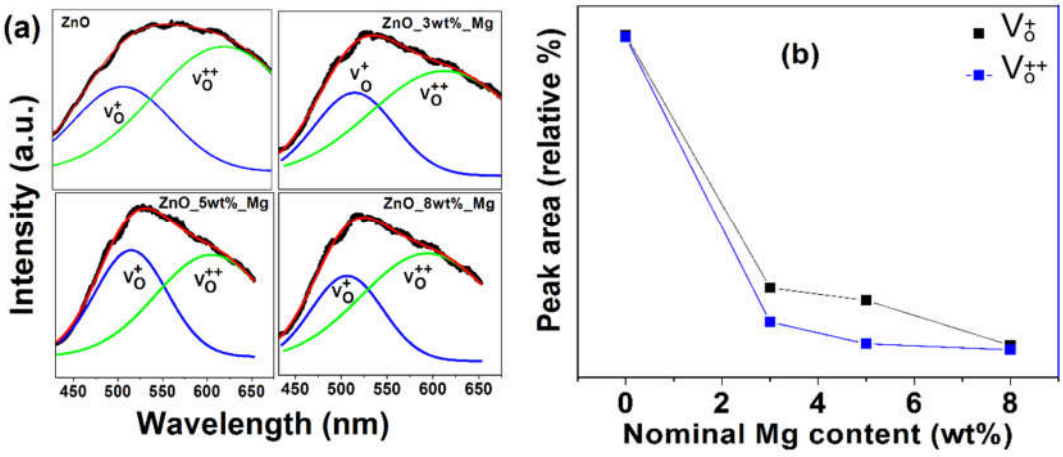

Figure 4.6: (a) Gaussian fits to the broad band in the PL spectra of the different amounts of Mg doped samples and (b) variation of peak area with Mg concentration.

4.1.5. Optical properties

Room temperature UV-visible absorption spectra of undoped and Mg doped ZnO nanowires are shown in Figure 4.7(a-d). The spectra show that undoped sample has a fundamental absorption band at 382 nm (3.25 eV) which is blue shifted from the bulk ZnO value of 400 nm [BHAT08]. In comparison, the band gap of the Mg^{2+} doped samples show a shift towards higher energies. The absorption edge is observed at 373 nm (3.32 eV), 361 nm (3.43 eV) and 348 nm (3.56 eV) corresponding to 3, 5 and 8 wt.% Mg^{2+} doped ZnO samples, respectively. Thus, band gap of ZnO increases with increase in Mg concentration. So, one can tune the band gap of the doped compound by varying the dopant concentration. Since the nanowire sizes are larger than excitonic Bohr radius of ZnO, the observed shift of band gap is not due to the size effects. Figure 4.7(e) shows the variation of average crystallite size with band gap energy of Mg doped ZnO nanostructures. From the figure it is apparent that up to 5 wt.% doping the shift is linear. So, we can conclude that the shift in the band gap is induced by the introduction of Mg ions in ZnO rather than by crystallize size effect [WANG06a]. Raman and PL studies presented in earlier section shows a decrease in defects with increase in Mg doping, which supports this conclusion. Compared to bandgap energy variations reported for similarly Mg doped electrospun ZnO nanofibers [CETI12, ZHAO10] and even for larger amounts of doping in $Mg_xZn_{1-x}O$ nanofibers, the band gap shift observed in the present samples is much higher. This difference is primarily due to differences in the preparation and processing conditions adopted in the three studies. It has to be pointed out here that much larger bandgap variation has been reported in in 2-dimensional $Mg_xZn_{1-x}O$ thin films obtained by pulsed laser ablation of ZnO and MgO targets [OHTO98].

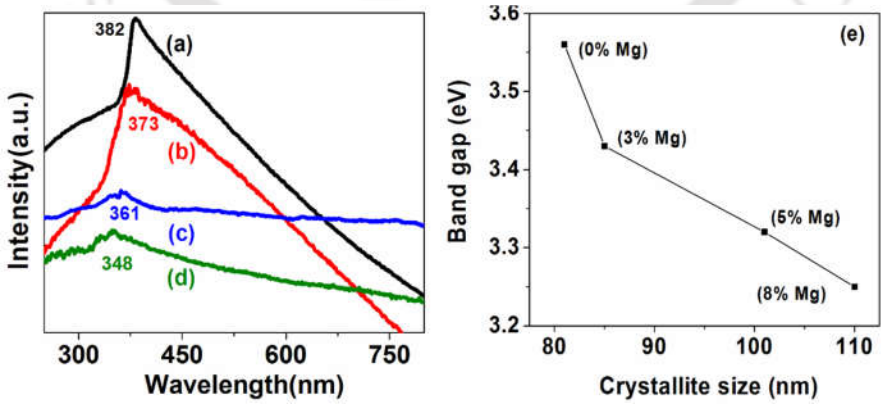

Figure 4.7: (a-d) UV-Visible absorption of ZnO nanowires containing different amounts of Mg doped annealed at 650 ^{0}C for 3 h. in air and (e) variation of band gap with crystallite size.

Figure 4.8 shows a plot of peak area ratio of the oxygen (V_o^+/V_o^{++}) defects as a function of band gap energy of the undoped and Mg doped ZnO samples. It shows that nearly linear correlation between the two parameters is seen till 5 wt.% Mg doping in ZnO. The figure also establishes that the observed change in band gap energy is related to the oxygen vacancies present in the samples.

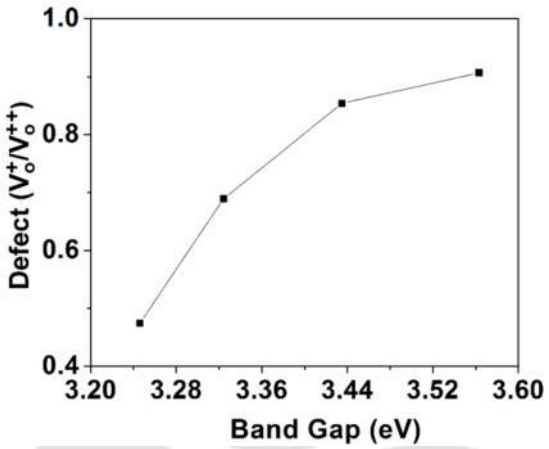

Figure 4.8: variation of band gap with defect state (V_o^+/V_o^{++}) ratio.

4.2. Co substituted ZnO nanostructures

TM doping in compound semiconductor ZnO facilitates generation of carrier mediated ferromagnetism [PEAR03]. Mg doping in ZnO by the procedure described above did not induce magnetism in the system. Hence, doping of a magnetic TM i.e. cobalt, was attempted.

4.2.1. Preparation

20 wt% aqueous zinc acetate [$Zn(CH_3COO)_2.2H_2O$, 99.9%, Merck Specialities Pvt. Ltd., India] solution was slowly added to 12 wt% aqueous PVA (MW~80,000) solution and continuously stirred till a homogeneous mixture was obtained. Then, appropriate amount of cobalt acetate [$C_4H_6COO_4.4H_2O$, 99%, Loba Chemicals, India] was added to the mixture so as include the desired amount (1 – 5 wt.%) of cobalt in the precursor mixture. The mixture was kept at room temperature for 4–5 h to obtain a viscous solution suitable for electrospinning. The solution was electrospun under a potential difference of 16 kV, spinneret needle to collector distance of 12 cm and solution flow rate of 0.5 ml/h. As-spun nanofibers were heated @4 °C/min to 550 °C in an electric furnace and held at this temperature for 90 min to obtain Co doped ZnO nanowires.

4.2.2. Thermo-gravimetric analysis

Figure 4.9 shows TG curves of as-spun PVA/zinc acetate and 5 wt.% Co doped PVA/zinc acetate nanofibers recorded a constant heating rate at 10^0 C/min. The TG curves showed three stages of weight loss, between (1) 50 and 110 °C corresponding to the removal of water from the compound, (2) 120 and 260 °C corresponding to the decomposition of PVA and removal of organic components from the fibers, and (3) 260 and 450 °C due to the oxidation and conversion of metal acetates to ZnO and Co doped ZnO. The residual weight of the samples was about 26% for all samples which represents the final amount of ZnO and Co doped ZnO nanofibers produced after removal of all organic components from the fibers. Since no perceptible weight loss was observed beyond 500 °C for these as-spun composite nanofibers, 550 °C was chosen as annealing temperature for converting the as-spun fibers into ZnO nanowires in this study.

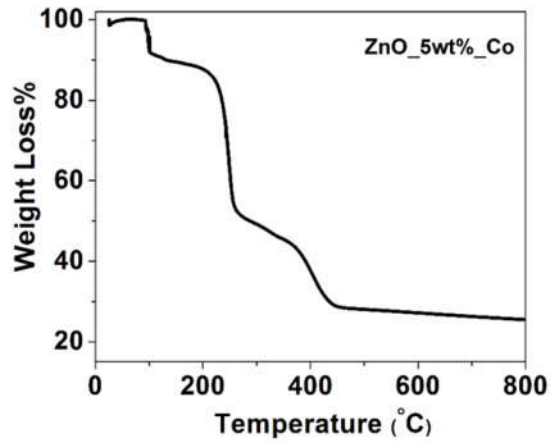

Figure 4.9: TG curve of as-spun composite nanofiber containing 5 wt.% cobalt acetate.

4.2.3. Structure and morphology

X-ray diffraction (XRD) patterns of as-spun composite nanofibers showed amorphous features with no crystalline peaks. Figure 4.10 shows the XRD patterns of 1 wt.%, 2 wt.%, 3 wt.%, and 5 wt.% Co doped ZnO composite nanofibers annealed at 550 °C for 90 minutes each. The XRD patterns could be indexed to wurtzite structure (space group $P6_3mc$) of ZnO, which indicates that the Co ions occupy the Zn lattice site of ZnO rather than the interstitial one. Single (wurtzite) phase structure was observed in samples with Co content up to 3 wt.%. However, the sample with 5 wt.% Co exhibited one extra weak peak corresponding to a reflection from (311) planes of Co_3O_4 which shows that impurity phases can occur at higher

Co doping in ZnO. Further, the decrease in the intensity of the diffraction peaks in Co-doped ZnO indicates that the dopant Co^{2+} ions are substituted in the inner lattice of Zn^{2+}. Since the ionic radius of Co^{2+} is close to that of Zn^{2+}, the observed broadening in the XRD peaks can be assigned to fine crystallite size (usually represented by the average crystallite size d_{av}) and microstrain (ε), which can be estimated from Williamsan-Hall analysis of the XRD peak profiles [CULL13]. d_{av} and ε of the samples estimated from the XRD patterns using Williamson Hall method are tabulated in Table 4.2. The reduction in d_{av} with increase in Co content is due to the distortion in the host ZnO lattice by Co^{2+} which decreases the nucleation and subsequent growth rate of ZnO structure. On the other hand, ε decreases slightly with increase in Co content. The unit cell volume does not show appreciable change with increase in Co content. The effect of incorporation of Co^{2+} ions into the ZnO lattice could be visualized from the slight changes in the lattice constants. Figure 4.10(e) shows the typical EDS spectrum recorded for 5 wt.% Co doped ZnO nanowires confirming the presence of Co in the annealed nanofibers. It may be noted that the precise determination of the elemental compositions is difficult since oxygen value is usually overestimated in the EDS measurements due to adsorbed oxygen in the samples.

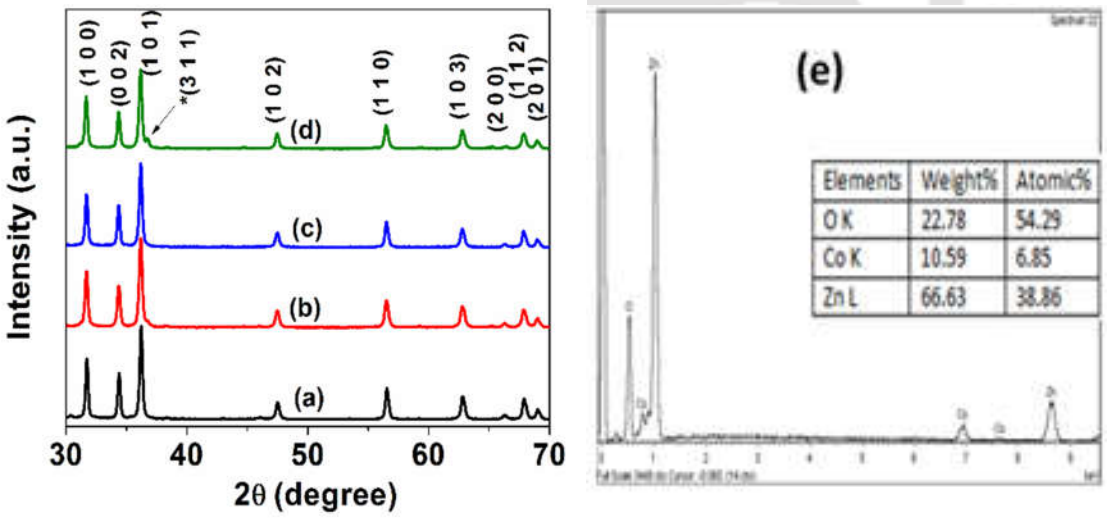

Figure 4.10: XRD patterns of (a) 1 wt.%, (b) 2 wt.%, (c) 3 wt.% and (d) 5 wt.% Co doped ZnO nanowires. (e) EDS spectrum of 5 wt.% Co doped ZnO nanostructure.

FESEM micrograph of the as-spun composite nanofibrous membranes indicate homogenous and interconnected fibrous network with no beads or string formation. The as-spun nanofibers are smooth and bead-free because of the amorphous nature of the zinc

acetate/cobalt acetate/PVA composite and the optimal electrospinning conditions, respectively. However, after annealing at 550 °C, the surface of the nanofibers turns rough and the fiber diameter decreases as a consequence of the removal of PVA and the conversion of the metal salt into ZnO with wurtzite structure. Average diameter of the individual fibers was estimated from multiple FESEM images using Image J™ software. Figure 4.11 (a)-(h) show FESEM images of inter-twined zinc acetate/PVA composite nanofibers containing 1 wt.%, 2 wt.%, 3 wt.% and 5 wt.% Co both in as-spun and annealed conditions. External electrospinning parameters (flow rate, needle to collector distance, voltage) were kept identical while preparing all the samples. However, internal parameters like solution (electrical) conductivity, viscosity and surface tension which depend on the metal salts content in the solution influence the fiber morphology varied according to the content of the precursor solution. It can be seen that the as-spun nanofibers are smooth and bead-free. 1 wt.% Co doped zinc acetate/PVA nanofibers have an average diameter of ~215 nm. Average diameter reduces to ~145 nm for nanofibers containing 5 wt.% Co. Upon annealing at 550 °C for 90 minutes, the average diameters of all the nanofibers shrank drastically. The shrinkage in fibers diameter is due to the removal of PVA from fibers and the conversion of metal salts into metal oxides. FESEM images of annealed nanofibers exhibit a rough surface due to the volatilization of PVA and the formation of 1–dimensional metal oxide nanocrystalline structure from the metal salt precursors.

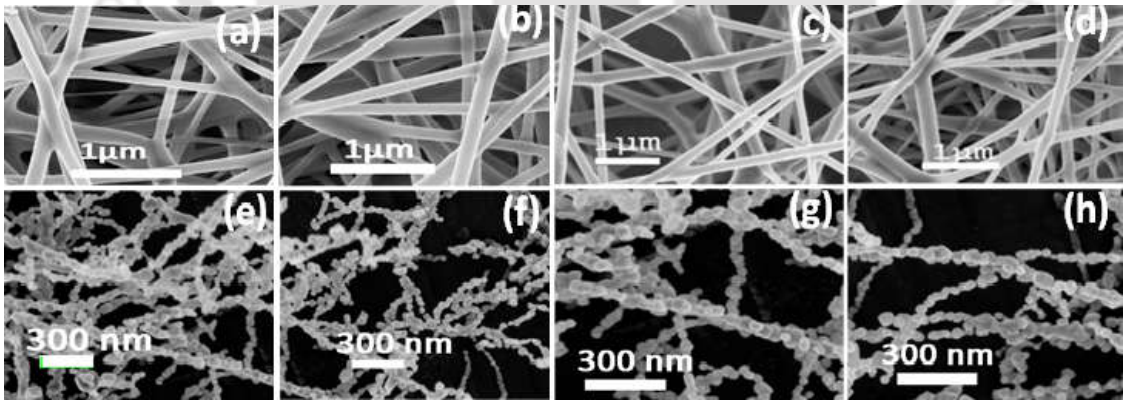

Figure 4.11: FESEM images of as-spun zinc acetate/PVA nanofibers with (a) 1 wt.%, (b) 2 wt.%, (c) 3 wt.% and (d) 5 wt.% cobalt acetate. Morphology of annealed (e) 1 wt.%, (f) 2 wt.%, (g) 3 wt.% and (h) 5 wt.% Co doped ZnO nanowires.

Table 4.2

Average crystallite size (d_{av}), microstrain (ε), lattice parameters (a, c) and unit cell volume (V) of Co doped ZnO nanowires.

Sample ID	d_{av} (nm)	ε ($\times 10^{-3}$)	a (nm)	c (nm)	V (nm)^3
1wt.%Co_ZnO	108	2.68	0.32544	0.52064	0.047754
2wt.%Co_ZnO	92	2.57	0.32544	0.52152	0.047835
3wt.%Co_ZnO	86	2.21	0. 32574	0.52152	0.047922
5wt.%Co_ZnO	82	2.20	0. 32574	0.52152	0.047922

4.2.4. Optical properties

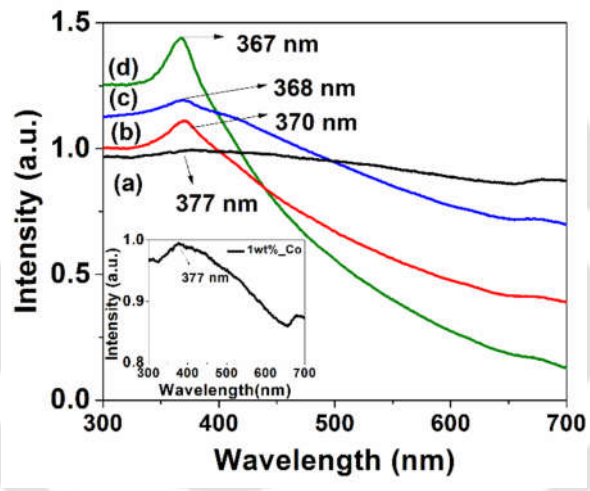

Figure 4.12: UV-Visible absorption spectra of (a) 1 wt% Co, (b) 2 wt% Co, (c) 3 wt% Co, and (d) 5 wt% Co-doped ZnO nanowires.

UV-visible absorption spectra have been used to find the possible modifications in the band structure of ZnO upon Co doping. Many groups have confirmed that Co atomically substitutes on Zn sites using a variety of optical methods such as x-ray photoelectron spectroscopy and optical absorption [SAMA05]. The four-fold coordinated ionic radius of Co^{2+} (0.058 nm) and Zn^{2+} (0.06 nm) are very similar which prompts large solubility of Co^{2+} in ZnO lattice. Figure 4.12 shows the optical absorption spectra taken at room temperature for annealed undoped and Co doped ZnO samples. Band gap energy of 3.25 eV (λ_g = 377 nm) observed for undoped ZnO [ARNA16] sample, shifts to 3.29 eV (λ_g = 377 nm) for the 1

wt.% doped sample and 3.38 eV (λ_g = 367 nm) for the 5 wt.% Co doped sample. Since the nanostructure sizes are larger than excitonic Bohr radius of ZnO, the increase in bandgap energy with Co doping in ZnO is not due to size effects. The *sp–d* exchange between the ZnO band electrons and localized *d*-electrons associated with the doped Co^{2+} cations can induce the observed changes in the band structure [ZHAN13]. Additionally, structural studies have shown that the microstrain decreases with increase in Co content in the ZnO nanocrystallites. This can also induce the change in the band gap energy of doped ZnO as pointed out by other researchers [SAMA05].

4.2.5. Magnetic properties

Magnetization was recorded as a function of applied magnetic field (M−H curves) for the Co doped ZnO nanowires at room temperature with a maximum applied field of ±15 kOe. Figure 4.13 shows that all the samples exhibit ferromagnetic behavior and there is an increase in magnetic moment with increase in concentration of Co. It is evident that the samples do not show magnetic saturation up to the maximum applied field of 15 kOe. The figure also shows that the ferromagnetic nature improves with increased Co doping in ZnO. Maximum coercivity (H_c ~68 Oe) and maximum magnetization (M_s ~0.14 emu/g) were observed upon 5 wt.% Co doping. This may be compared with M_s of 0.028 emu and H_c 189 Oe reported [JCUI06] for 2% Co doped ZnO nanowire array electrodeposited on Si substrate. The changes in the M−H loop can be explained on the basis of the magnetic contribution from the orientation of the strong exchange interaction in the *d*−*d* couple with cobalt ions. An increase in Co content increases the linear behavior of the M−H loop which indicates that Co−Co super-exchange interaction dominates at higher Co doping concentrations at room temperature. According to RKKY theory [RUDE54], the observed magnetism can be attributed to exchange interaction between local spin-polarized electrons and conduction electrons. The spin-polarized conduction electrons perform an exchange interaction with local spin-polarized electrons of other Co^{2+} ions. Thus, after the long-range exchange interaction, almost all Co^{2+} ions exhibit the same spin direction. As a result, the material exhibits ferromagnetism. The other possibility of the observed ferromagnetism could be due to secondary phases of cobalt oxides such as Co_3O_4. But Co_3O_4 is well known antiferromagnetic with a Neel temperature of ~40 K [ROTH64] although its weak presence in samples with higher Co content has been confirmed from XRD and Raman studies. So, the observed ferromagnetic behavior is not due to the presence of Co_3O_4 in some of the samples. The other possibility is the existence of Co clusters, since Co is well-known ferromagnetic

material. Nano-Co clusters can provide the dominant source of the ferromagnetism [CONG09]. However, considering the weak ferromagnetism observed in these samples, one can easily rule out this possibility. M–H loops of annealed 5 wt.% Co:ZnO nanofibers recorded at 30 K are 300 K are shown as inset in Figure 4.13. Inset shows that even at 30 K the magnetization did not exhibit saturation, which indicates considerable paramagnetic contribution in the weakly ferromagnetic sample. These results may be compared to the maximum M_s of 0.062 emu/g reported for $Ni_xZn_{1-x}O$ nanofibers with x = 0 annealed at 600 °C for 3 h [HUAN17]. M_S, M_R and H_C values extracted from the M-H curves displayed in Figure 4.13 are tabulated in Table 4.3.

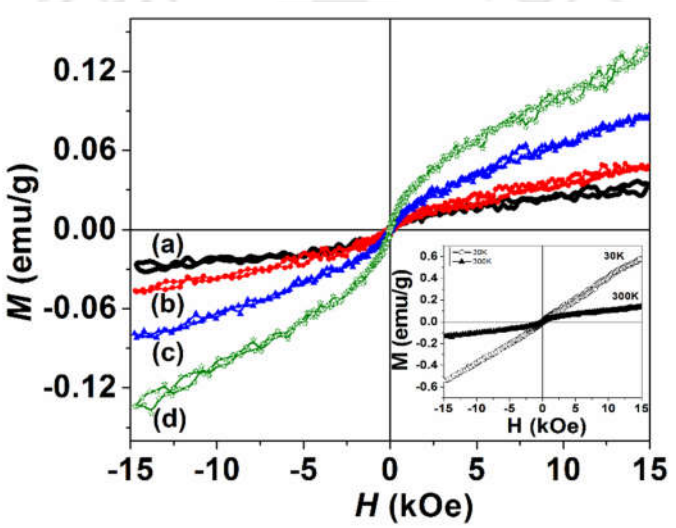

Figure 4.13: Room temperature *M-H* curves of (a) 1 wt.%, (b) 2 wt.%, (c) 3 wt.% and (d) 5 wt.% Co doped ZnO nanowires. Inset shows M-H loops of the annealed 5 wt% Co doped ZnO nanowires recorded at 30 K and 300 K.

Table 4.3

Saturation magnetization (M_S), coercivity (H_c) and retentivity (M_R) of Co doped ZnO nanowires.

Sample ID	M_S (emu/g)	H_c (Oe)	M_R (emu/g)
1wt.%Co_ZnO	0.035	24.366	9.925
2wt.%Co_ZnO	0.045	19.797	16.299
3wt.%Co_ZnO	0.084	40.017	5.47
5wt.%Co_ZnO	0.139	68.534	40.33

4.2.6. Defect analysis

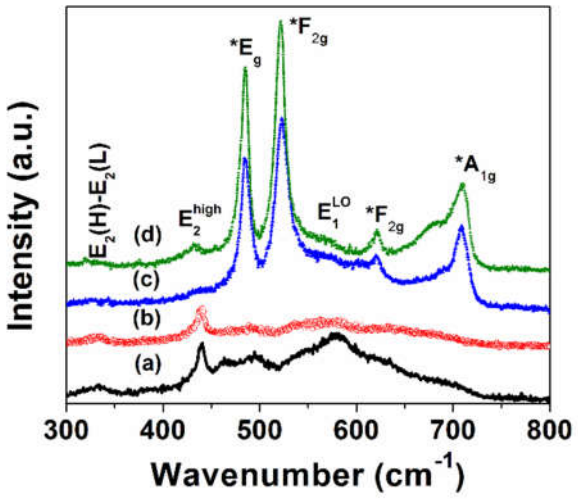

Figure 4.14: Raman spectra of (a) undoped, (b) 1 wt.% Co, (c) 2 wt.% Co, (d) 3 wt.% Co and (e) 5 wt.% Co-doped ZnO nanowires.

Figure 4.14 shows micro-Raman spectra of the undoped and doped ZnO nanostructures at room temperature. For the undoped ZnO, the sharpest and strongest peak at 439 cm^{-1} can be assigned to the high frequency branch of $E_2(H)$ phonon mode which is characteristic of wurtzite ZnO. The peaks located at 385 cm^{-1} and 330 cm^{-1} correspond to $A_1(TO)$ and $E_2(H)$–$E_2(L)$ modes, respectively. Single (wurtzite) phase structure is observed in samples with Co content up to 2 wt.%. Beyond this doping level, some extra peaks are observed. These additional peaks (marked with symbol * in Figure 4.14) in Raman spectra of samples with 3 wt.% and 5 wt.% Co can be assigned to the Co_3O_4 phase [ROMC10]. The $E_2(H)$ mode broaden asymmetrically when the Co is doped. This is due to the broken symmetry induced by the incorporation of Co dopants into the ZnO structure. The peaks located at 482 cm^{-1} and 522 cm^{-1} correspond to E_g mode and F_{2g} modes of this phase, respectively. Two other peaks located at 620 cm^{-1} and 690 cm^{-1} correspond to F_{2g} and A_{1g} modes of the same phase, respectively. It is clear from the figure that as Co concentration is increased, the intensity of peak at 439 cm^{-1} characteristics of wurtzite structure decreases and other peaks attributed to Co_3O_4 increases. Interestingly, the E_1-LO peak characteristic of O-vacancy defects expected at ~581 cm^{-1} [MAHA83] is not clearly discernible in the spectra of the Co doped ZnO samples, although it is prominently present in the undoped sample. This shows that oxygen defects are not present in a noticeable way in the 1-d Co doped ZnO samples. Hence, the RTFM observed in samples cannot be attributed to oxygen defect as in the case of the

undoped sample. Thus, Raman studies clearly clarifies that small amounts of Co_3O_4 phase which are not discernible by XRD are present in samples with Co content higher than 2 wt.% in ZnO nanofibers.

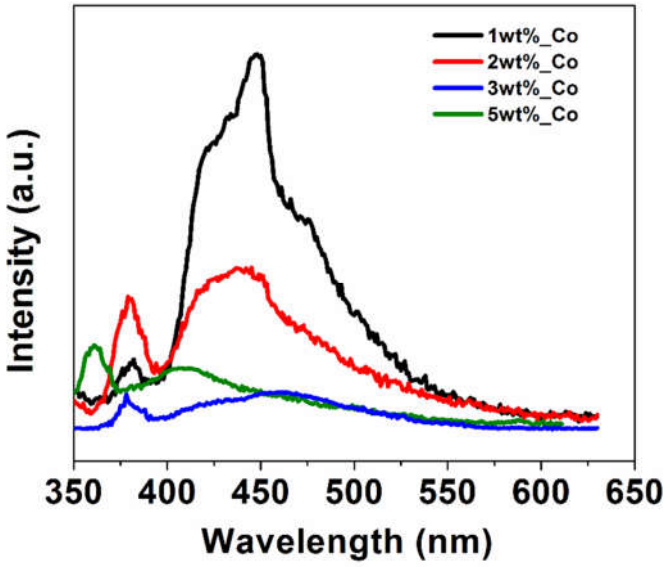

Figure 4.15: PL spectra of ZnO nanowires with different amounts of Co.

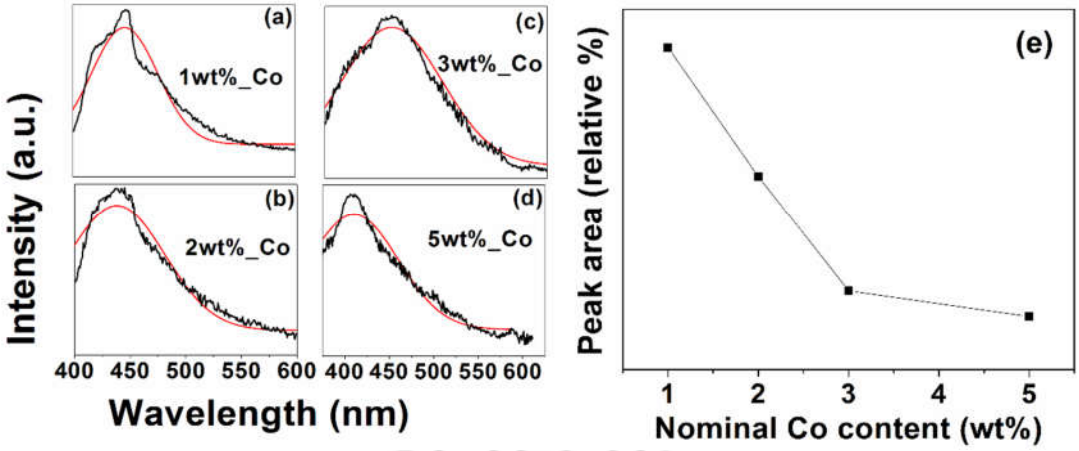

Figure 4.16: (a-d) Gaussian fit to the broad PL band of Co doped ZnO samples. (e) Variation of area under the broad PL peak area with Co doped ZnO samples.

Figure 4.15 displays the PL spectra of air annealed samples. All the spectra exhibit a relatively sharp UV emission peak centered near 382 nm. The UV band edge emission is attributed to free excitonic emission of ZnO. It can be seen that increasing Co^{2+} doping concentration from 1-5wt.%, shifts the ultraviolet band edge emission peak towards the blue

region. This indicates that Co^{2+} substitutes for Zn^{2+} and in the process increases the band gap energy of the system. Since the atomic radii of Zn^{+2} and Co^{+2} are comparable, they can substitute each other. This is in agreement with the UV-vis absorption studies discussed in section 4.2.4. It may also be seen from the figure that the broad PL peak appearing in all spectra is centred between 400-450 nm. From its shape and position, it is evident that it does not have the same origin as the one observed in undoped (cf. Figure 3.8) and Mg doped ZnO (cf. Figure 4.5) samples. In order to understand the origin of this broad peak, it was further analyzed by fitting it to Gaussian peak(s). In that process, it became clear that unlike the case of the undoped ZnO (cf. Figure 3.9) and Mg doped ZnO (cf. Figure 4.6) samples, this broad PL peak could be fitted to a single Gaussian profile as shown in Figure 4.16 (a-d). In most cases, a Gaussian peak centered at ~ 440 nm seemed to provide a decent fit to this PL emission band. It may be noted that the PL emission in ZnO centred ~440 nm is generally ascribed to doubly ionized zinc vacancies (V_{Zn}^{++}) [JANO06]. Hence, V_{Zn}^{++} appears to be the main point defect in Co doped ZnO nanowires. Figure 4.16(e) shows that upon Co doping, there is a decrease in the zinc vacancies as seen by the reduction in the peak area of this peak. The loss of linearity in the reduction in the area beyond 2 wt.% Co doped ZnO and the shift in peak position for 5 wt.% Co deoped ZnO sample could be due to the formation of Co_3O_4. Since, ferromagnetism in Co doped ZnO samples increase with Co content, one cannot attribute the origin of RTFM in this system to either oxygen or zinc vacancies.

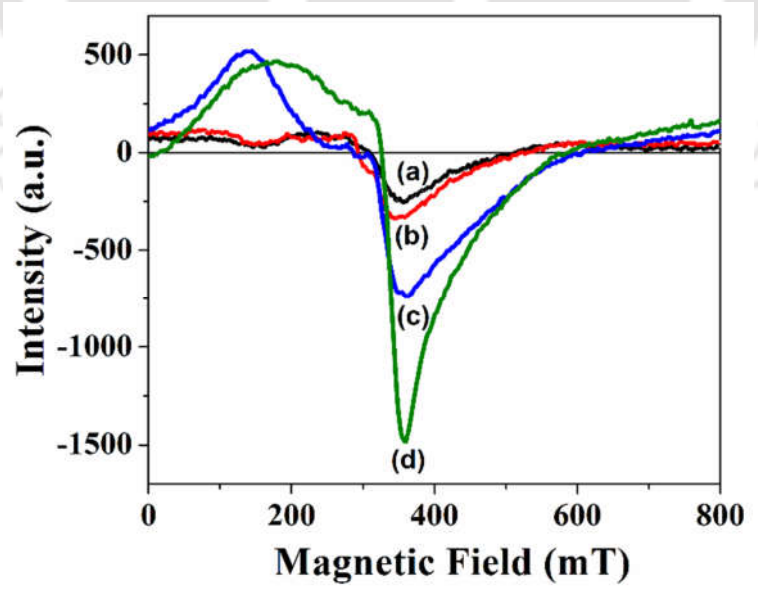

Figure 4.17: EPR spectra of (a) 1 wt.% Co, (b) 2 wt.% Co, (c) 3 wt.% Co and (d) 5 wt.% Co doped ZnO nanowires.

EPR studies were performed to understand how the Co ions are incorporated in the ZnO lattice and the magnetic behavior of the samples. Co atoms are expected to substitute Zn atoms in the compound and the neutral charge state is Co^{2+} (a $3d^7$ configuration) [GAND14]. Room temperature EPR spectrum of undoped ZnO exhibits a single absorption at g~1.99, which indicates the presence of a paramagnetic defect [ARNA16]. Figure 4.17 shows the EPR spectra obtained for annealed Co doped ZnO nanowires. The spectra consist of a single EPR absorption signal. The resonance field (H_r) of the signal is found to shift from 287.3 mT to 325.7 mT (g = 2.16 to 2.45) as the Co content is increased from 1 wt.% to 5 wt.%. EPR spectra of 1 wt.% and 2 wt.% Co doped ZnO nanofibers are symmetric with H_r below 300 mT. However, the EPR spectra of 3 wt.% and 5 wt.% Co doped ZnO nanofibers are asymmetric with larger shift in H_r. The linewidth of the signal also increases with increase in Co content. Raman studies have already pointed the existence of Co_3O_4 in 3 wt.% and 5 wt.% Co doped ZnO nanowires. Co_3O_4 is an antiferromagnetic compound whose EPR signal is composed of a wide line located at H_r of ~300 mT [MESA14]. Hence, EPR spectra of 3 wt.% and 5 wt.% Co doped ZnO nanowires show indications of Co_3O_4 phase by the asymmetry in the EPR signal and higher (> 300 mT) H_r and EPR linewidth.

4.3. Summary

Upto 8 wt.% Mg and 5 wt.% Co doped inter-twinned 1-d ZnO nanowires have been prepared by electrospinning metal oxide precursors and PVA followed by heat treatment. The highlights of the investigations carried out on these samples are summarized below:

- Annealed nanowires are crystalline with single hexagonal structure of ZnO for Mg doping up to 5 wt%.
- Analysis of the blue-green PL band shows that the oxygen vacancies decrease with increase in Mg doping. Enhancement in band gap energy from 3.25 to 3.56 eV and a reduction in oxygen defects observed upon Mg^{2+} doping in ZnO nanowires.
- XRD analysis showed that Co^{2+} ions get incorporated in Zn^{2+} sites in ZnO structure and annealed nanowires exhibit single phase (wurtzite) structure for Co doping up to 3 wt.%. However, Raman and EPR studies indicate the presence of Co_3O_4 phase in samples with more than 2 wt.% Co.
- Enhancement in band gap energy from 3.29 to 3.38 eV is observed upon Co doping in ZnO nanowires.

- 1-d Co doped ZnO were weakly ferromagnetic at room temperature with considerable paramagnetic component. RTFM observed can be attributed to exchange interaction between local spin-polarized electrons and conduction electrons of Co.
- Lack of oxygen defects in Co doped ZnO nanowires exhibiting RTFM shows that alternate mechanisms can also induce RTFM in TM doped ZnO nanostructures.

Chapter 5

PHASE TRANSITION IN NANOCRYSTALLINE CUBIC $CaFe_2O_4$ AND $Ca_{0.9}Co_{0.1}Fe_2O_4$ POWDERS PREPARED BY SOL-GEL ROUTE

This chapter presents the preparation of $CaFe_2O_4$ and $Ca_{0.9}Co_{0.1}Fe_2O_4$ nanoparticles by sol-gel method, its heat treatment and the properties of the resulting nanostructures.

As mentioned in the first chapter, ferrites in nanometer scale are known to exhibit novel structural and magnetic properties which are not observed in their bulk counterparts. One of the most interesting magnetic properties of ferrite materials is the on-set of superparamagnetism in single domain particles with nanometer size. Among the ferrites, calcium ferrite is special because it can crystallize with orthorhombic structure. Since it has not been studied in detail in nanocrystalline form, this chapter is devoted to the preparation, processing and characterization of nanocrystalline $CaFe_2O_4$ and $Ca_{0.9}Co_{0.1}Fe_2O_4$.

5.1. Nanocrystalline $CaFe_2O_4$

5.1.1. Preparation

$CaFe_2O_4$ nanoparticles were synthesized by sol-gel method. Analytical grade $Ca(NO_3)_2.4H_2O$ and $Fe(NO_3)_3.9H_2O$ purchased from Loba Chemie, India, were used as precursors. 1.18 g and 4.04 g of the metal salts of calcium and iron taken in molar ratio of 1:2 were mixed in 50 ml of deionized water. Then, the solution was heated slowly to 90 °C with continuous stirring followed by addition of 5 ml of ethylene glycol. The resulting solution was kept at 120 °C with continuous stirring until it transformed into a xero gel. On further heating, the gel burnt out completely to form a loose powder. Parts of the as-synthesized powder were separately annealed at T_A ranging between 300 °C and 1100 °C for 8 h each.

5.1.2. Thermo-gravimetric analysis

The as-synthesized powder consists of a composite of metal precursors. In order to obtain the target compound $CaFe_2O_4$ from the precursor, heat treatment is essential. In order to understand the effect of heat treatment on the as-synthesized powder and to optimize the heat treatment conditions, TG analysis was performed on the samples. Figure 5.1 shows TG curve of as-synthesized powder. Three different stages of mass loss observed in the data. The first mass loss of 12.5% is observed in the region between room temperature and ~160 °C corresponding to the removal of water and absorbed gases. The second stage of weight loss observed between 200 and 460 °C represents complete crystallization of $CaFe_2O_4$. The final mass loss between 460 °C and 740 °C can only indicate a structural transition in the system to more stable state. The thermogram shows the relative mass loss in the crystallization of the crystalline phase and the structural transformation along with the temperature range at which these reactions are complete. Based on the TG data, the as-synthesized samples were

annealed at 400°C, 500°C and 1100 °C for 8 h each to understand the significance of the reactions occurring in the sol-gel sample at these temperatures.

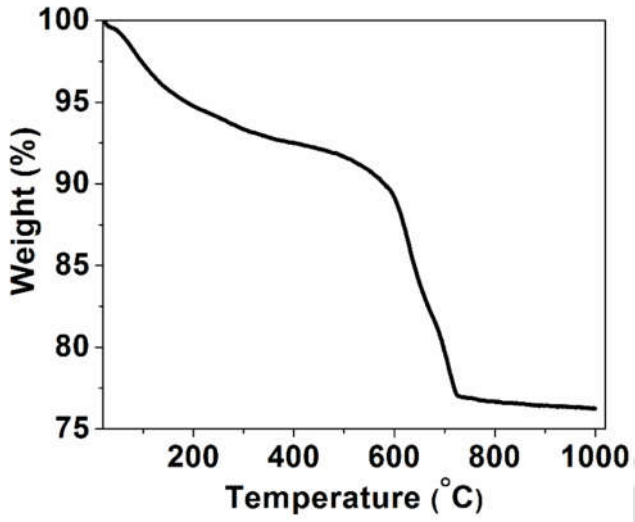

Figure 5.1: Thermogravimetric curve for as-synthesized $CaFe_2O_4$ nanoparticles.

5.1.3. Structure and morphology

Room temperature XRD patterns of as-synthesized and samples annealed at 400°C, 500°C and 1100 °C for 8 h each are depicted in Figure 5.2(a,b). It can be seen that all the Bragg reflections in Figure 5.2(a) could be indexed to face centred cubic Fe_3O_4-type structure (space group *Fd*3*m*, No: 227, JCPDS file # 85-1436) without any appreciable impurity phases. This confirms that the as-synthesized and samples annealed below 400 °C crystallize in single phase cubic spinel structure. The lattice constant of as-synthesized sample and those annealed at 400 °C and 500 °C are 8.33 Å, 8.34 Å and 8.35 Å, respectively. This shows that the spinel unit cell of the as-synthesized $CaFe_2O_4$ expands slightly when the annealing temperature is increased up to 500 °C. Average crystallite size estimated using Debye-Schërrer equation [AKZA11] for various peaks in the XRD patterns was averaged to obtain the average crystallite size (D_{av}). D_{av} of the as-synthesized, 400 °C and 500 °C annealed samples are 11.5, 14.0 and 15.6 nm, respectively. Upon annealing above 400 °C, new peaks (marked as * in figure) such as the (3 2 0), (0 3 1) and (6 1 0) reflections of orthorhombic $CaFe_2O_4$ start appearing along with the cubic peaks of spinel $CaFe_2O_4$. Annealing at 1100 °C for 8 h yielded a single phase orthorhombic $CaFe_2O_4$ as observed in the XRD pattern depicted in Figure 5.2(b). Rietveld refinement of the diffraction pattern was carried out for the

orthorhombic unit cell in which all atoms occupy the 4c position (space group Pnma, No. 62). Based on the analysis, the orthorhombic unit cell parameters were deduced to be a = 9.2362 Å, b = 10.7111 Å and c = 3.0213 Å. The refined unit cell parameters (*cf.* Table 5.1) are in good agreement with the values reported in the literature [SAMA13] and JCPDS file # 32-0168. The average crystallite size of orthorhombic $CaFe_2O_4$ is 46.4 nm, which is more than thrice that of the spinel phase obtained by annealing at 400 °C. This study shows that the sol-gel powders contain cubic $CaFe_2O_4$. The cubic spinel structure could be stabilized till 300 °C. Heat treatment above this temperature induces a slow transformation of the cubic phase into orthorhombic phase. Complete transformation of the cubic structure to orthorhombic structure occurs only after the heat treatment at 1100 °C.

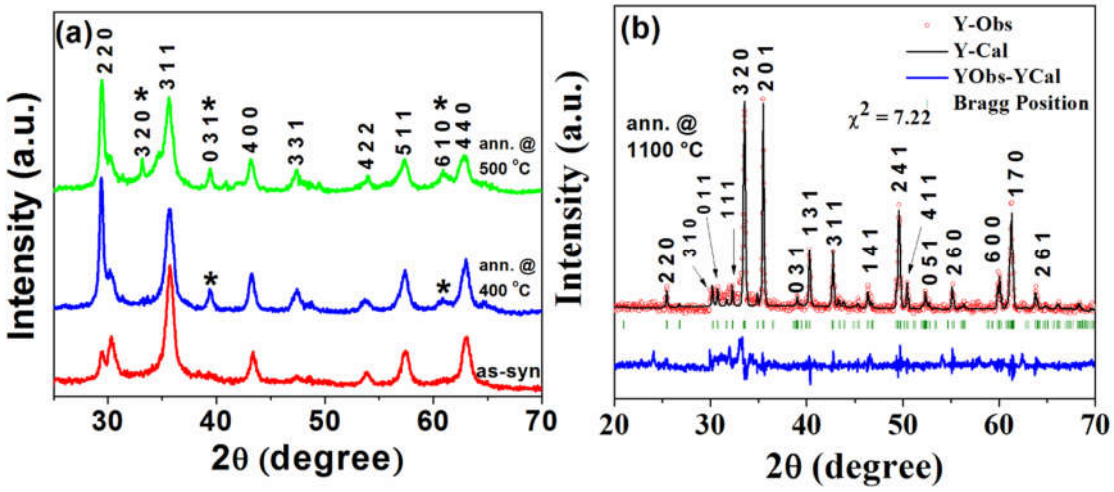

Figure 5.2: (a) XRD patterns of as-synthesized, 400 °C and 500 °C annealed samples exhibiting predominantly cubic structure. (b) XRD pattern of 1100 °C annealed sample (red open circles) exhibiting single phase orthorhombic structure. Solid line in black colour represents the least squares (Rietveld) fit to the experimental data (red open circles). The difference plot between the experimental and fit data is also shown below the XRD pattern.

Transmission electron micrographs of cubic Fe_3O_4 and orthorhombic $CaFe_2O_4$ powder obtained by annealing the as synthesized powder at 300 °C and 1100 °C for 8 h are shown in Figure 5.3 (a,b). Figure 5.3(a,b) shows the low resolution image of a typical cubic and orthorhombic $CaFe_2O_4$ particle, respectively. It can be seen that this particle is an aggregation of several smaller crystallites. Figure 5.3(c) provides a high resolution image of the lattice fringes of an orthorhombic $CaFe_2O_4$ crystallite. Inter planar spacing of the plane

corresponding to the lattice fringes was found to be 2.61 Å, which corresponds to the (3 2 0) plane of orthorhombic $CaFe_2O_4$. EDS spectrum of the orthorhombic sample is shown in Figure 5.3(d) which confirms the presence of Ca, Fe and O. The table given as an inset in this figure provides the elemental composition of the particle. It can be seen that the composition is very close to that of the compound $CaFe_2O_4$.

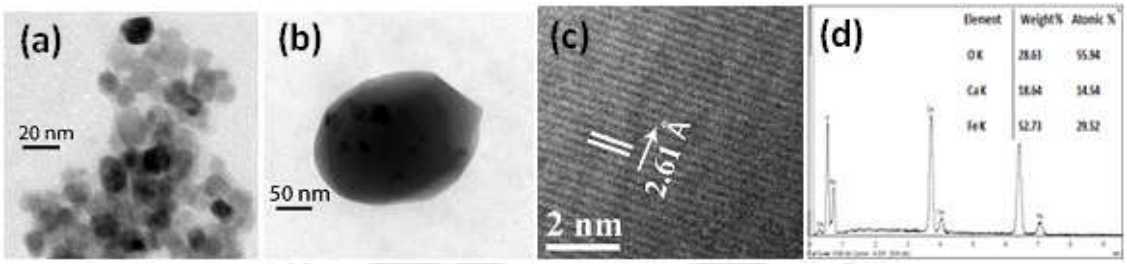

Figure 5.3: Morphology of $CaFe_2O_4$ nanoparticle annealed (a) at 300 °C (b) 1100 °C. (c) High resolution TEM lattice image of a $CaFe_2O_4$ particle annealed at 1100 °C. (d) EDX spectrum and elemental composition of the orthorhombic $CaFe_2O_4$ sample.

Table 5.1. Atomic positions in orthorhombic $CaFe_2O_4$ unit cell [space group: Pnma (No. 62)].

Atom	*Site (Wyck)*	*X*	*Y*	*Z*	*Occupancy*
Ca	4c	0.76279	0.25000	0.64919	0.50000
Fe1	4c	0.41305	0.25000	0.10128	0.50000
Fe2	4c	0.43695	0.25000	0.61377	0.50000
O1	4c	0.23961	0.25000	0.15115	0.50000
O2	4c	0.11191	0.25000	0.49913	0.50000
O3	4c	0.50817	0.25000	0.78692	0.50000
O4	4c	0.43539	0.25000	0.42120	0.50000

5.1.4. Magnetic properties

Figure 5.4(a) shows the room temperature field dependent magnetization curve recorded for as-synthesized and $CaFe_2O_4$ powder annealed at 400 °C and 500 °C. All the samples show nearly zero remanent magnetization (M_r) and zero coercivity (H_c) indicating that they exhibit superparamagnetic behaviour at room temperature. Saturation magnetization (M_s), M_r and H_c extracted from the M-H curves are tabulated in Table 5.2. The table shows that M_s increases with annealing temperature and attains its maximum value for the sample annealed at 400 °C and then decreases slightly. To understand these results, let us revisit the XRD results which

show that annealing below 400 °C stabilizes the cubic spinel structure and annealing above this temperature induces a slow transformation to orthorhombic structure. Hence, one expects a well crystallized cubic phase exhibiting superparamagnetic behaviour near 400 °C and a mixed (cubic and orthorhombic) phase at 500 °C. Presence of a small amount of ferrimagnetic orthorhombic phase at 500 °C is the reason for the observed reduction in M_s in this sample. Figure 5.4(b) shows that room temperature M-H curve of the 1100°C annealed sample which exhibits ferrimagnetic nature with low magnetization value.

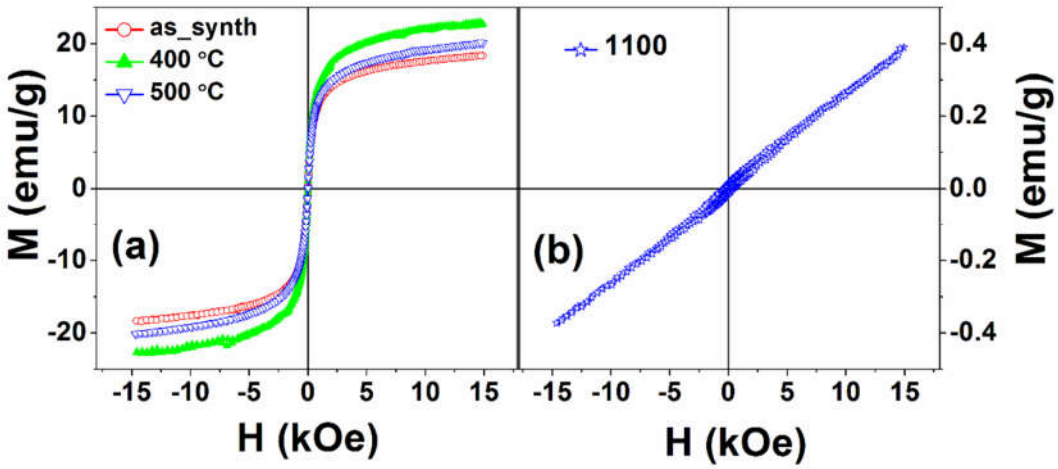

Figure 5.4: Room temperature M-H curves of (a) as-synthesized, 300 °C and 400 °C annealed sample and (b) 1100 °C annealed sample.

Temperature dependent magnetization of the nanoparticles was recorded under zero-field cooled (ZFC) and field cooled (FC) conditions. In ZFC measurement, the sample was cooled from room temperature to 30 K without applying any magnetic field. After reaching that temperature, a small magnetic field of 500 Oe was applied and magnetization of the sample was measured as a function of increasing temperature. During FC measurement, the sample was cooled from room temperature to 30 K under an applied magnetic field of 500 Oe. ZFC and FC curves of sample annealed at 400 °C depicted in Figure 5.5(a) show a bifurcation at 190 K and a broad peak at 141 K in the ZFC curve. The latter corresponds to the blocking temperature (T_B) below which the single domain particle's magnetic moment is blocked. T_B shifts between 248 K and 104 K when the applied field is varied between 100 Oe to 1 kOe, indicating the influence of applied field on spin fluctuation. M-H curves of as-synthesized sample recorded at 30 K and 300 K are shown in Figure 5.5(b). The M-H loops clearly show that nanocrystalline $CaFe_2O_4$ is superparamagnetic at room temperature.

Magnetic hysteresis observed at 30 K signifies the blocked spin at this temperature. The hysteresis loops recorded below T_B show a small value of coercivity. But the loops show no shift in the magnetic field axis signifying that there is no exchange bias.

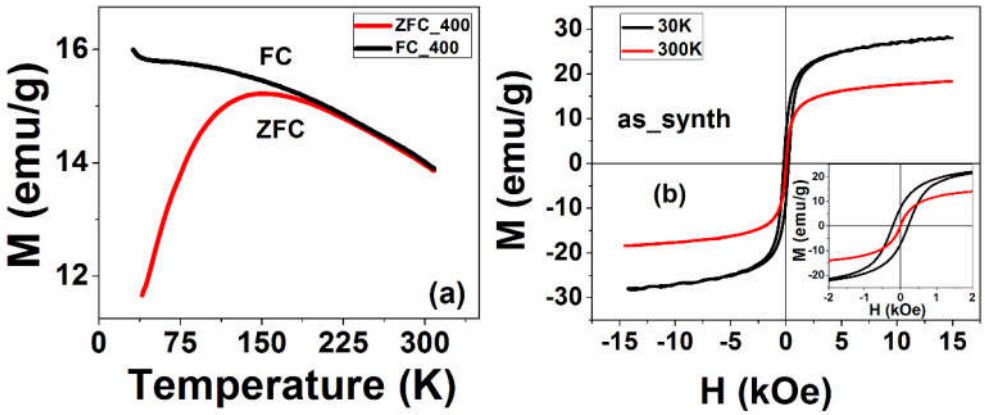

Figure 5.5: (a) M-T curves of the 400 °C annealed sample. (b) M-H curves of as-synthesized sample recorded at 30 and 300 K. Inset shows an enlarged view of data close to the origin.

Coercivity (H_c) of as-synthesized sample extracted from M-H loops recorded from 30 K to 300 K is plotted as a function of temperature in Figure 5.6. Variation in coercivity with temperature is analysed by considering the thermal fluctuations of the blocked moments around the blocking temperature. At low temperatures, magnetic moment of the single domain particles is blocked and coercivity is expected to follow the $T^{1/2}$ law in the intermediate temperatures [SANC04]. Inset of Figure 5.6 shows that the $T^{1/2}$ law behaviour depicted by the as-synthesized spinel nanoparticles.

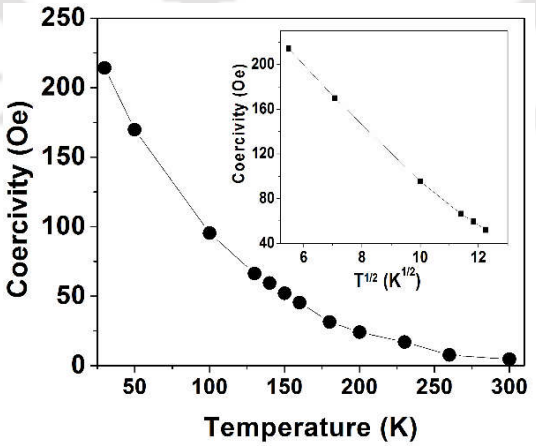

Figure 5.6: Temperature dependence of coercivity of as-synthesized $CaFe_2O_4$ nanoparticles. Inset shows $T^{1/2}$ power law dependence of the data in the intermediate temperatures.

Table 5.2. Remanent magnetization M_r, saturation magnetization M_s, coercive field H_c and average crystallite size (D_{av}) of as synthesized and heat treated $CaFe_2O_4$ powders.

Sample	Coercivity H_c (Oe)*)*	Retentivity M_r (emu/g)	Magnetization M_s (emu/g)	D_{av} (nm)
As synthesized	4.66	0.27	18.38	11.5
Annealed at 400 °C	5.34	0.33	22.92	14.0
Annealed at 500 °C	5.21	0.21	20.13	15.6
Annealed at 1100 °C	350.28	13.18	0.39	46.4

M-T curves of the sample annealed at 1100 °C are shown in Figure 5.7(a), which are very different from the ones depicted in Figure 5.7(a). In this case, both the ZFC and FC curves exhibit the same trend as the sample is cooled from room temperature. Magnetization is initially constant as the temperature is decreased. On further lowering the temperature, magnetization increases sharply, reaches a maximum value and then decreases almost linearly down to 30 K. This behaviour is typical of an antiferromagnetic material exhibiting a transition to paramagnetic state at Néel temperature (T_N) of ~175 K. To confirm the validity of this observation, M-H loops were recorded at different temperatures ranging from 30 K to room temperature under an applied field of 500 Oe. M-H loops recorded at 30, 140, 160 and 200 K are depicted in Figure 5.7(b). M-H loops measured at temperatures below T_N clearly exhibit antiferromagnetic nature along with a shift in the loop position from the origin towards the negative magnetic field axis. Generally, exchange bias is characterized by coercivity enhancement as a consequence of induced uniaxial or multiaxial anisotropy. A shift in the hysteresis loop along the field axis after field cooling reveals unidirectional anisotropy in the sample. On the other hand, M-H loops recorded above T_N show neither magnetic hysteresis nor exchange bias effect, thereby clearly indicating the paramagnetic state of the sample at these temperatures. Below T_N, the Fe^{3+} magnetic moments order antiferromagnetically [KOLE03]. This antiferromagetic ordering is the reason for the observed shift in the hysteresis loops along field axis. Antiferromagnetic to paramagnetic transition in nanocrystalline $CaFe_2O_4$ at T_N ~190 K has also been reported in the literature [BERT66]. The slight variation in the observed T_N may be due to differences in crystallite size in the two samples.

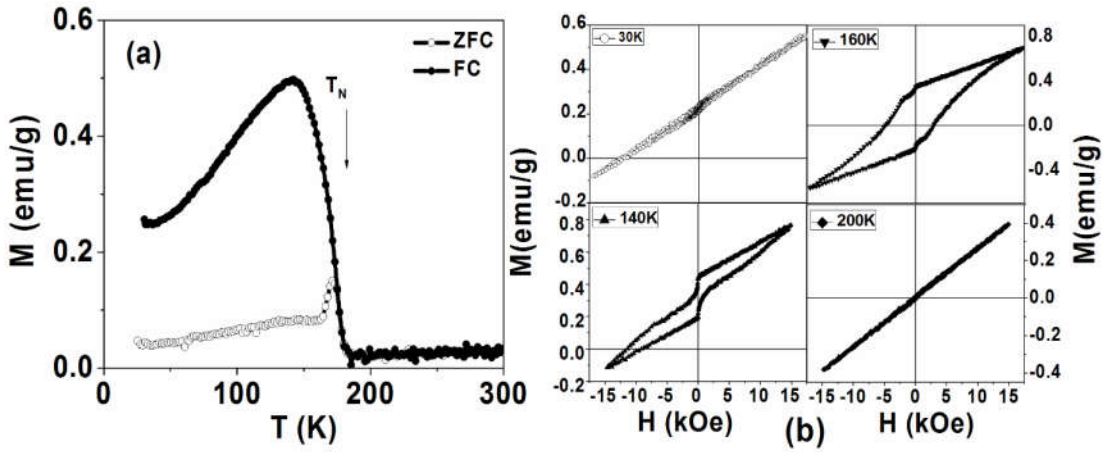

Figure 5.7: (a) M-T curves and (b) M-H loops recorded at selected temperatures for the 1100 °C annealed sample.

Figure 5.8 shows room temperature Mössbauer spectrum of $CaFe_2O_4$ nanoparticles subsequent to annealing at 400 °C. The spectrum is predominantly deconvoluted into two doublets with isomer shift close to 0.3 mm/s and quadrupole splitting around 0.25 mm/s and 0.75 mm/s, respectively. These doublets mainly arise due to superparamagnetic nature of the $CaFe_2O_4$ spinel nanocrystalline particles. Average crystallite size of these cubic particles has already been deduced to be 14 nm by XRD studies. A small fraction of Fe atoms associated with slightly larger sized $CaFe_2O_4$ particles experiences magnetic interactions leading to the occurrence of a small sextet. The isomer shift, quadrupole splitting, internal field have been evaluated from the Mössbauer data.

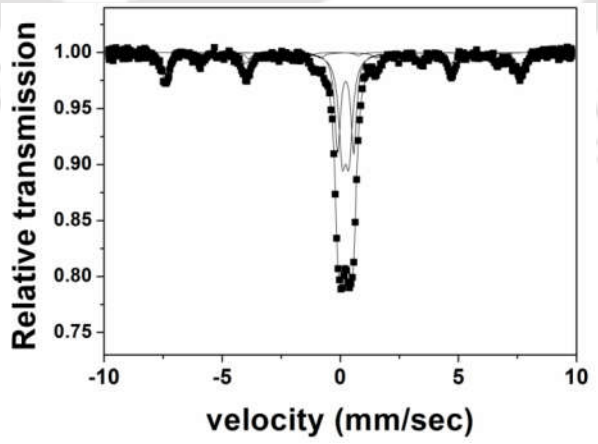

Figure 5.8: Room temperature ^{57}Fe Mössbauer spectrum of $CaFe_2O_4$ powders subsequent to annealing at 400 °C.

Figure 5.9 shows the Mössbauer spectra recorded for the 1100 °C annealed sample as a function of temperature. At higher temperatures, the magnetic splitting gradually collapses due to decrease in superparamagnetic relaxation time, forming a well-defined quadrupole doublet. It can be seen that the sextet component at 85 K changes dramatically into the paramagnetic doublet at 200 K, corresponding to disappearance of magnetic ordering with increase in temperature [HIRA06]. This shows that there is a transition from antiferromagnetic to paramagnetic state in the sample with a T_N between 170 and 200 K. It has already been pointed out earlier that M-T data show T_N to be ~175 K for this sample, which has now been confirmed by the Mössbauer studies. It has also been mentioned earlier that there is a report of such an antiferromagnetic to paramagnetic transition near 190 K in $CaFe_2O_4$ in the literature [LOBA11]. Mean hyperfine field $<B_{hf}>$ extracted from the Mössbauer spectra as a function of temperature is plotted in Figure 5.10.

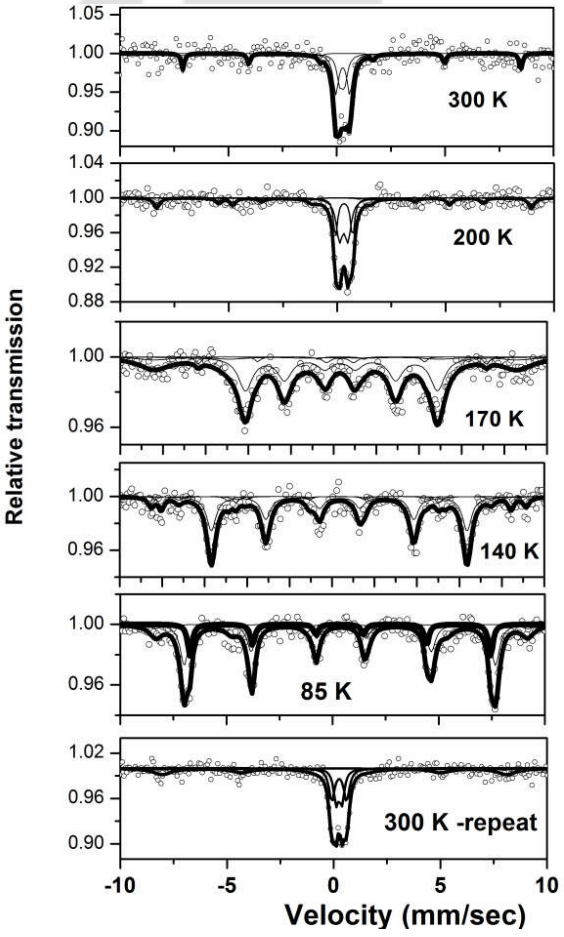

Figure 5.9: ^{57}Fe Mössbauer spectra of $CaFe_2O_4$ powders annealed at 1100 °C recorded at different temperatures.

The hyperfine magnetic field $<B_{hf}>$ decreases as the temperature is increased due to collective magnetic excitations. It is seen that $<B_{hf}>$ decreases drastically after 170 K, implying the proximity of the antiferromagnetic T_N of this system. This observation is also consistent with the reported results in the literature.

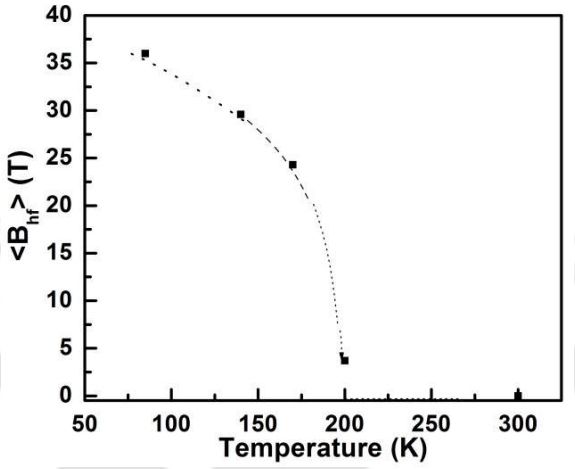

Figure 5.10: Temperature dependence of the mean hyperfine field $<B_{hf}>$ of 1100 °C annealed $CaFe_2O_4$ particles.

5.2. Nanocrystalline $Ca_{0.9}Co_{0.1}Fe_2O_4$

It is generally expected that substitution of a ferromagnetic element in Ca site can improve the magnetic properties of $CaFe_2O_4$. In order to verify this, Co has been substituted in $CaFe_2O_4$ at Ca site. The resulting effect on the structure and magnetic properties of the ferrite are presented below.

5.2.1. Preparation

$Ca_{1-x}Co_xFe_2O_4$ (x = 0.1) nanoparticles were also synthesized by sol-gel method. Analytical grade $Ca(NO_3)_2.4H_2O$ and $Fe(NO_3)_3.9H_2O$ and $C_4H_6COO_4.4H_2O$ purchased from Loba Chemie, India were used as precursors. 1.06 g, 0.13 g and 4.04 g of calcium, cobalt and iron salts taken in appropriate molar ratio corresponding to the stoichiometry, were mixed in 50 ml of deionized water. Then, the solution was heated slowly to 90 °C with continuous stirring followed by addition of 5 ml of ethylene glycol. The resulting solution was held at 120 °C with continuous stirring until it transformed into a xero gel. The xero gel was burnt out completely on further heating to form a powder.

5.2.2. Thermo-gravimetric analysis

Figure 5.11 shows the TG curve of as-synthesized $Ca_{0.9}Co_{0.1}Fe_2O_4$ powder. Three different stages of mass loss are observed in the graph just as in the case of $CaFe_2O_4$ powders. Hence, the TG data is interpreted in the same lines. The first mass loss is observed in the region between room temperature and ~170 °C corresponding to the removal of water and absorbed gases. The second stage of weight loss observed between 200 and 450 °C represents complete crystallization of the cubic spinel phase in $Ca_{0.9}Co_{0.1}Fe_2O_4$. The final mass loss between 450 °C and 700 °C indicates the crystallization of orthorhombic phase of $Ca_{0.9}Co_{0.1}Fe_2O_4$. As-synthesized $Ca_{0.9}Co_{0.1}Fe_2O_4$ powders were annealed at 1100 °C for 8h to obtain the orthorhombic phase in the Co substituted $CaFe_2O_4$ nanoparticles.

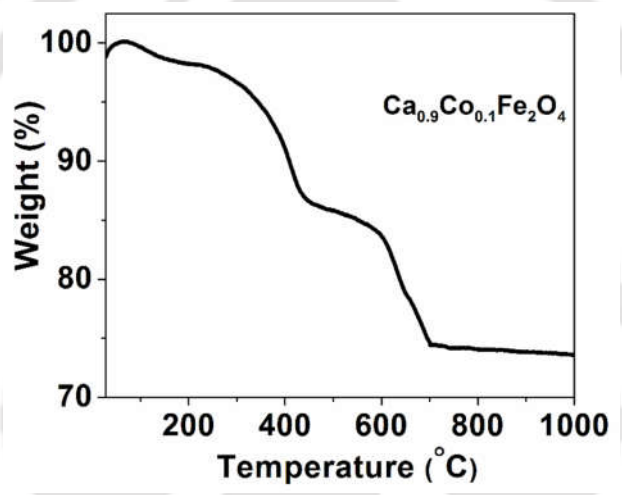

Figure 5.11: Thermogravimetric curve for as-synthesized $Ca_{0.9}Co_{0.1}Fe_2O_4$ nanoparticles.

5.2.3. Structure and morphology

Room temperature XRD patterns of as-synthesized and 1100 °C annealed $Ca_{0.9}Co_{0.1}Fe_2O_4$ are depicted in Figure 5.12(a,b). Figure 5.12(a) shows that most of the peaks in the XRD patterns of as-synthesized samples could be indexed to face centred cubic Fe_3O_4-type structure (space group *Fd3m*, No: 227, JCPDS file # 85-1436). Some peaks not belonging to the cubic phase were also found in all the cases. These peaks (marked as *) could be identified as due to $CoFe_2O_4$ phase (space group Fd-3m, No: 227, JCPDS file # 22-1086) precipitation. Thus, the as-synthesized powder crystallized mainly in cubic spinel structure along with Co precipitates. This shows that even 0.1 mole% of Co could not be substituted in $CaFe_2O_4$ without inducing $CoFe_2O_4$ precipitation. The lattice constant of as-synthesized cubic

$Ca_{0.9}Co_{0.1}Fe_2O_4$ is 7.86 Å. This shows that the spinel unit cell of the as-synthesized $Ca_{0.9}Co_{0.1}Fe_2O_4$ decreases slightly as compared to $CaFe_2O_4$ powder. Figure 5.12(b) shows that despite the presence of $CoFe_2O_4$ phase precipitates in cubic $Ca_{0.9}Co_{0.1}Fe_2O_4$, a structural transition to orthorhombic phase was observed when annealed at 1100 °C. However, along with the orthorhombic peaks, some extra peaks (marked as #) due to cubic $CoFe_2O_4$ (space group Fd-3m, No: 227, JCPDS file # 22-1086) is also observed in all the annealed samples. Average crystallite size estimated using Debye-Schërrer equation [AKZA11] for various peaks in the XRD patterns was averaged to obtain the average crystallite size (D_{av}). The average crystallite size obtained for this structure is found to be 35.4 nm. The orthorhombic unit cell parameters were deduced to be a = 9.2808 Å, b = 10.5433 Å and c = 3.0111 Å for $Ca_{0.9}Ca_{0.1}Fe_2O_4$ nanostructure.

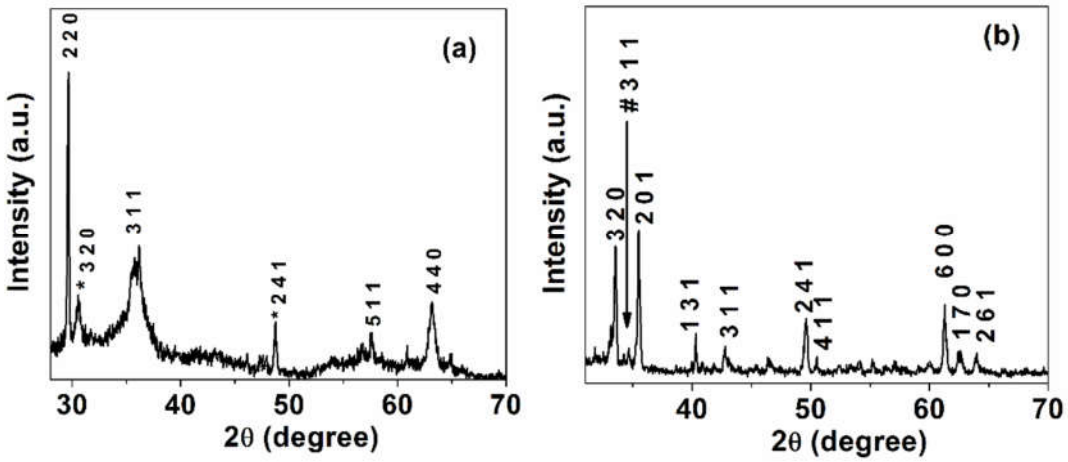

Figure 5.12: X-ray diffraction patterns of (a) as-synthesized samples exhibiting predominantly cubic structure and (b) 1100 °C annealed sample exhibiting orthorhombic structure.

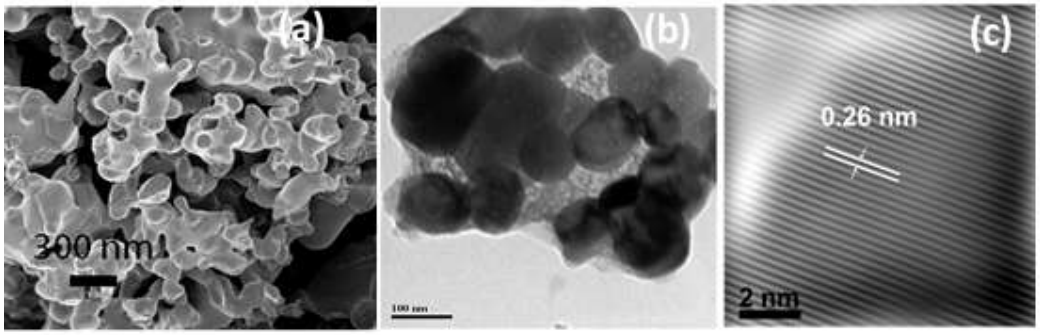

Figure 5.13: (a) FESEM image, (b) TEM image, and (c) high resolution TEM lattice image of $Ca_{0.9}Co_{0.1}Fe_2O_4$ particle annealed at 1100 °C.

Figure 5.13(a) displays an FESEM image of $Ca_{0.9}Co_{0.1}Fe_2O_4$ nanoparticles annealed at 1100 °C. The image shows irregularly shaped particles with mainly spherical and capsule-like shapes. The average particle size was found to be ~180 nm. Low resolution TEM image of the sample is shown in Figure 5.13(b). Figure 5.13(c) illustrates the high resolution lattice image of a crystallite. Inter planar spacing of the plane corresponding to the lattice fringes was found to be 0.26 nm, which corresponds to the (3 2 0) plane of orthorhombic $CaFe_2O_4$. EDX analysis shows that overall composition of the compound to be $Ca_{0.88}Co_{0.12}Fe_{2.02}O_{3.85}$.

5.2.4. Magnetic properties

Figure 5.14 shows the room temperature field dependent magnetization curves recorded for as-synthesized and 1100 °C annealed $Ca_{0.9}Co_{0.1}Fe_2O_4$ powders. In the case of as-synthesized $CaFe_2O_4$ nanoparticles, superparamagnetic behaviour with nearly zero remanent magnetization (M_r) and zero coercivity (H_c) at room temperature was observed. But with substitution of mere 0.1 mole % Co in Ca site of $CaFe_2O_4$, superparamagnetic behaviour is lost and ferromagnetic behaviour sets in as can be noticed by the large H_c and M_r of the sample. In fact, M_s of $Ca_{0.9}Co_{0.1}Fe_2O_4$ is slightly lower than the as-synthesized (superparamagnetic) $CaFe_2O_4$.

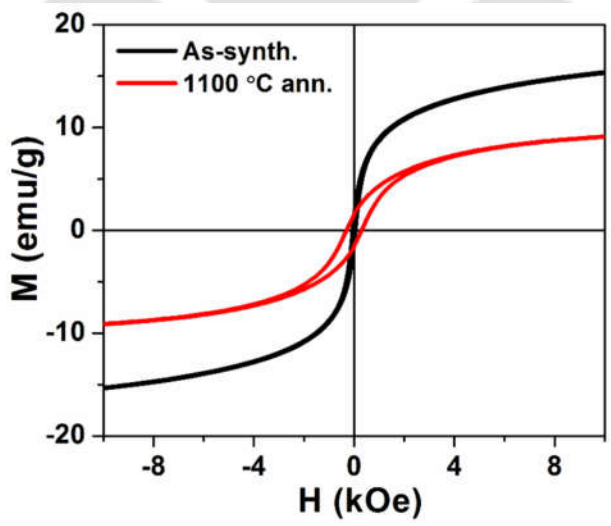

Figure 5.14: Room temperature M-H curve of $Ca_{0.9}Co_{0.1}Fe_2O_4$ as-synthesized and 1100 °C annealed sample.

On the other hand, the 1100 °C annealed $Ca_{0.9}Co_{0.1}Fe_2O_4$ exhibits lower M_s than the as-synthesized sample. The reason for this can be understood from the XRD results which show that as-synthesized sample stabilizes the cubic spinel structure and annealing it 1100

°C transforms it to orthorhombic structure. From our previous $CaFe_2O_4$ data we see that sample annealed at 1100 °C shows ferrimagnetic behaviour with low saturation magnetization but with substitution of Co it shows ferromagnetic behaviour with high M_s. It should be noted that small amounts of $CoFe_2O_4$ present as impurity phase in both the cubic and orthorhombic samples can also contribute to the observed magnetic properties. Magnetic parameters of the $Ca_{0.9}Co_{0.1}Fe_2O_4$ samples are tabulated in Table 5.3.

Table 5.3. Remanent magnetization M_r, saturation magnetization M_s, coercive field H_c and average crystallite size (D_{av}) of as synthesized and heat treated $Ca_{0.9}Co_{0.1}Fe_2O_4$ powders.

Sample	M_s (Oe)	H_c (Oe)	M_r (Oe)	D_{av} (nm)
As-synthesized	16.34	50.72	1.24	18.1
Annealed at 1100 °C	9.33	303.45	1.55	35.4

5.3. Summary

$CaFe_2O_4$ and $Ca_{0.9}Co_{0.1}Fe_2O_4$ nanostructures have been prepared by sol-gel method followed by annealing at temperatures between 300 to 1100 °C for 8 h.

- Room temperature XRD patterns shows that cubic nanocrystalline $CaFe_2O_4$ powder transforms to orthorhombic phase when annealed above 300 °C. Annealing as-synthesized powder at 1100 °C yields single phase $CaFe_2O_4$ powder with orthorhombic structure.
- Cubic $CaFe_2O_4$ shows superparamagnetic behaviour and weak ferromagnetic behaviour appears in the sample upon crystallization of the orthorhombic phase at temperatures above 400 °C.
- The orthorhombic phase exhibits antiferromagnetic to paramagnetic transition with $T_N \sim 175$ K.
- Mössbauer spectroscopy confirmed the superparamagnetic behaviour of the spinel $CaFe_2O_4$ and the antiferrmagnetic to paramagnetic transformation in orthorhombic $CaFe_2O_4$.
- Even 0.1 mole% Co substitution for Ca in $CaFe_2O_4$ induces precipitation of $CoFe_2O_4$ phase. Co substitution does not alter the cubic to orthorhombic transition in $CaFe_2O_4$.

- Magnetic properties of $CaFe_2O_4$ are drastically modified upon Co substitution. Superparamagnetism in as-synthesized cubic $CaFe_2O_4$ is lost upon Co substitution.

Chapter 6

STRUCTURAL & MAGNETIC PROPERTIES OF 1-DIMENSIONAL $CaFe_2O_4$

This chapter presents the structural and magnetic properties of heat treated PVA nanofibers containing calcium and iron salts.

In the previous chapter, investigations carried out on $CaFe_2O_4$ and $Ca_{0.9}Co_{0.1}Fe_2O_4$ prepared by sol-gel route was discussed. Considering the interesting results obtained in that work, it was decided to look at other forms of Nanocrystalline $CaFe_2O_4$. This chapter is devoted to investigations on 1-demensional form of calcium ferrite.

6.1. Preparation

Since the samples were prepared by electrospinning route, the precursor polymer solution was first prepared. For this, 12 wt.% aqueous PVA solution (MW ~80,000, Sigma-Aldrich) was prepared by dissolving PVA powder in deionized water heated to 80 °C under constant stirring. Then, analytical grade $Ca(NO_3)_2.4H_2O$ and $Fe(NO_3)_3.9H_2O$ [Merck Specialities Pvt. Ltd., India] taken in molar ratio of 1:2, respectively, were added to the PVA solution with continuous stirring until a homogeneous mixture was obtained. This mixture was kept at room temperature for 4-5 h to obtain a viscous solution suitable for electrospinning. The solution was then electrospun under a potential difference of 14 kV, spinneret to collector distance of 12 cm and solution flow rate of 0.5 ml/h. As-spun nanofibers were annealed at temperatures ranging from 400 °C to 1000 °C in an electric furnace under ambient conditions for 8 h each to obtain well crystallized $CaFe_2O_4$.

6.2. Thermo-gravimetric analysis

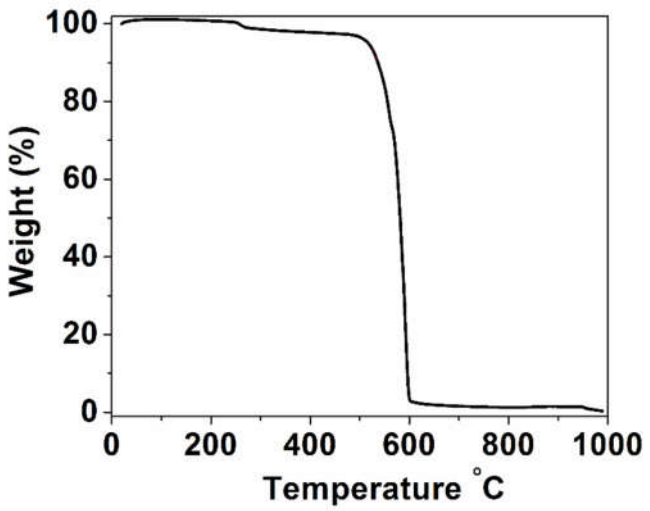

Figure 6.1: Thermogravimetric curve for PVA/calcium nitrate/ferric nitrate composites.

Figure 6.1 shows TG curve of as-spun composite nanofibers. The curve shows two prominent stages of weight loss unlike the clear three stage weight loss observed in the sol-gel derived

$CaFe_2O_4$ nanoparticles discussed in the previous chapter. The first mass loss of 4% is observed between room temperature and ~260 °C. This could be attributed to removal of water content and organic matter (by decomposition of PVA) and the complete crystallization of cubic $CaFe_2O_4$ from the pre-cursor salts. The sharp weight loss between 550 °C and 610 °C could represent the solid state transformation of cubic $CaFe_2O_4$ phase to orthorhombic phase. This large (90%) weight loss leads to a stable structure since no further weight loss is observed in this system. The two-stage weight loss pattern indicates that the cubic $CaFe_2O_4$ phase could have partially formed during the electrospinning process itself. On the basis of the TG data, as-spun samples were heat treated at 400 °C, 500 °C, 600 °C and 1000 °C for 8 h each.

6.2. Structure and morphology

Room temperature XRD patterns of as-spun as well as annealed specimen are depicted in Figure 6.2. It can be seen that all the Bragg reflections in the XRD patterns of samples annealed up to 500 °C could be indexed to face centred cubic (marked as (c)) Fe_3O_4-type structure (space group Fd3m, No: 227, JCPDS file # 85-1436) without any appreciable impurity phases(figure 6.2(b)). However, the as-spun nanofibers showed weak cubic peaks with a predominantly amorphous character which is shown in figure 6.2(a). This indicates that the cubic phase of $CaFe_2O_4$ partially crystallizes during the electrospinning process. A closer look at the XRD patterns will confirm that as-spun composite nanofibers annealed up to 500 °C for 8h crystallize in single phase cubic spinel $CaFe_2O_4$ structure. The lattice constant of the nanofibers annealed at 400 °C, 500 °C, 600 °C are 8.37 Å, 8.37 Å, 8.38 Å, respectively. This shows that the spinel unit cell of the as-synthesized $CaFe_2O_4$ expands slightly when the annealing temperature is increased up to 600 °C. Average crystallite size (D_{av}) of 400 °C, 500 °C and 600 °C annealed samples estimated using Schërrer's equation [AKZA11] are 11.5 nm, 14.0 nm and 18.0 nm, respectively. The D_{av} values represent the mean value of estimates made from various reflections in the corresponding XRD pattern. It it is apparent that the average crystallite size increases with increasing annealing temperature. Upon annealing above 500 °C, new XRD peaks from (3 1 0), (0 3 1) and (4 3 1) planes of orthorhombic $CaFe_2O_4$ start appearing along with the cubic peaks of spinel $CaFe_2O_4$. In order to obtain single phase $CaFe_2O_4$ nanostructure, the as-spun sample had to be annealed at 1000 °C for 8 h as illustrated in the figure. Orthorhombic unit cell parameters were deduced to be a = 9.2981 Å, b = 10.7271 Å and c = 3.0243 Å for the single phase $CaFe_2O_4$ sample. The

calculated unit cell parameters are in good agreement with the values reported in the literature [KHAN13, SAMA13] and JCPDS file # 32-0168. D_{av} of orthorhombic $CaFe_2O_4$ obtained by annealing at 1000 °C for 8 h is 28.6 nm which is almost double that of the spinel phase obtained by annealing at 500 °C. Further comparison with the XRD patterns of sol-gel derived $CaFe_2O_4$ nanoparticles depicted in Figure 5.2 will show that the cubic phase could be stabilized at higher temperaures (up to 500 °C) in the electrospun $CaFe_2O_4$. Thus, the cubic to orthorhombic transition is delayed in this novel nanostructure as compared to the nanoparticles obtained by sol-gel route. Similarly, single phase orthorhombic structure was obtained upon on annealing a lightly lower temperature in this nanostructure as compared the sol-gel derived nanoparticles. This shows that the cubic to orthorhombic transition is compete in a shorter temperature range in these nanostructures as compared to the nanoparticles obtained by sol-gel route.

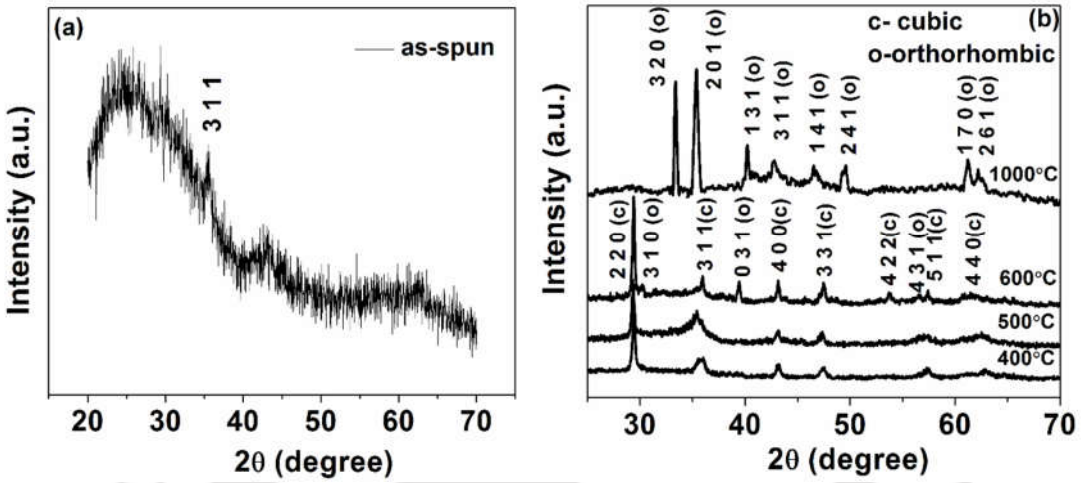

Figure 6.2: X-ray diffraction patterns of (a) as-spun and (b) 400 °C, 500 °C, 600 °C and 1000 °C annealed nanofibers.

FESEM micrograph of as-spun composite nanofibers depicted in Figure 6.3(a) indicate homogenous and interconnected fibrous network with no beads or string formation. The as-spun nanofibers are smooth and bead-free because of the amorphous nature of PVA and the optimal electrospinning conditions, respectively. However, after annealing at 500 °C and 1000 °C, the surface of the nanofibers turns rough and the fiber diameter decreases as a consequence of the removal of PVA and the complete conversion of the metal salts into nanocrystalline $CaFe_2O_4$. Average diameter of the individual fibers was estimated from multiple FESEM images using Image J™ software. The average diameter of the as-spun

fibers was about 160 nm. Upon heat treatment, fiber diameter shrinks dramatically to about 90 nm. The typical corrugated 1-d nanostructure obtained by this process can be seen from the figure. Due to the restricted growth geometry and high concentration of nucleates, the crystallites merge and grow as interconnected beads leading to a weakly bound but extended 1-d $CaFe_2O_4$ nanostructure. Such novel 1-d nanostructure is typical nanomaterials obtained by electrospinning process. EDX spectrum of the sample is shown in Figure 6.3(d) which confirms the presence of Ca, Fe and O and table given as an inset provides the elemental composition of the particle. It can be seen that the composition is very close to that of the compound $CaFe_2O_4$.

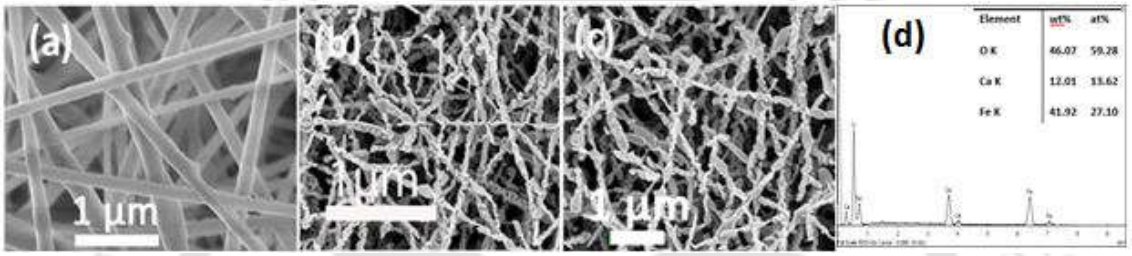

Figure 6.3: FESEM images of (a) as-spun, (b) 500 °C annealed and (c) 1000 °C $CaFe_2O_4$ nanofibers. (d) EDX spectrum and elemental composition of the orthorhombic $CaFe_2O_4$ sample depicted in (c).

6.3. Magnetic properties

Figure 6.4 shows the room temperature M-H curves recorded for 1-d $CaFe_2O_4$ nanostructures obtained by annealing the nanofibers at 400 °C, 500 °C, 600 °C and 1000 °C. Inset (a) in Figure 6.4 shows the M-H loop of poorly crystallized as-spun nanofibers. The poor magnetic properties of the as-spun nanofibers motivated the annealing treatment. Inset (b) in Figure 6.4 provides an expanded view of the M-H curves of the annealed samples close to the origin. It is clear from inset (b) and the data presented in Table 6.1 that M_s increases, whereas M_r and H_c decrease as the annealing temperature is increased up to 600 °C. High M_s, and nearly zero M_r and H_c exhibited by these samples indicate superparamagnetic behaviour at room temperature. M_s increases with annealing temperature and attains its maximum value for the sample annealed at 500 °C and then decreases drastically as the annealing temperature is increased further. M-H curve of the 1000 °C annealed sample exhibits ferrimagnetic nature with low magnetization value. XRD results depicted in Figure 6.2 shows that annealing up to 500 °C stabilizes the cubic spinel structure and annealing above this temperature induces a

slow transformation of the cubic phase to orthorhombic structure. Presence of a small amount of ferrimagnetic orthorhombic phase at 600 °C and complete transformation to weakly magnetic single phase orthorhombic structure at 1000 °C are the reasons for the observed reduction in the magnetization of these samples. Hence, one expects a well crystallized cubic phase exhibiting superparamagnetic behaviour near 500 °C and a mixed (cubic and orthorhombic) phase at 600 °C.

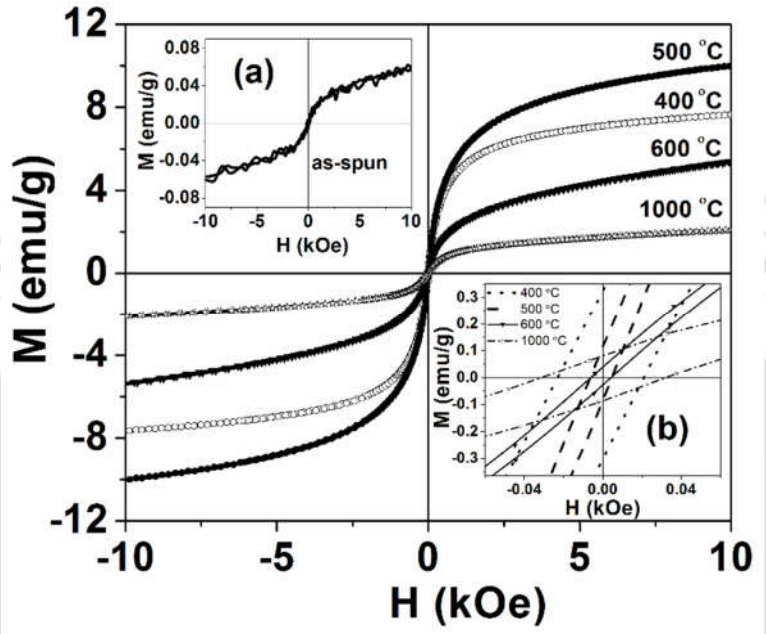

Figure 6.4: Room temperature M-H curves of annealed samples. Inset (a) shows M-H curve of as-spun sample. Inset (b) shows an expanded view of the data on annealed samples close to the origin.

Table 6.1. Properties of as synthesized and heat treated $CaFe_2O_4$ nanofibers.

Sample ID	Coercivity H_C (Oe)	Retentivity M_r (emu/g)	Magnetizatin M_s (emu/g)	D_{av} (nm)
As-spun	108.36	0.3	0.07	-
400 ˚C	21.93	0.57	14.73	11.4
500 ˚C	5.46	0.18	19.58	14
600 ˚C	5.31	0.03	6.23	18
1000 ˚C	31.65	13.18	2.19	28.6

A comparison with the literature reveals that the cubic to orthorhombic transformation is delayed till 500 °C in 1-d $CaFe_2O_4$ as compared to spherical nanoparticles in which the transformation was observed upon annealing above 400 °C [SAMA13]. This indicates that superparamagnetism associated with the spinel phase sustains for slightly higher temperatures in 1-d $CaFe_2O_4$ as compared to 0-d $CaFe_2O_4$ nanoparticles. It may noted that the Ca:Fe ratio in $CaFe_2O_4$ obtained by sol-gel route is 1:2, whereas it is 1:1.9 for the electrospinning samples. It is not expected that this small change in the stoichiometry could be the reason for the large variation in the structural transition observed. M-H curves of 500 °C annealed sample recorded at 30 K and 300 K (*cf.* Figure 6.5(a)) illustrate that while 1-d $CaFe_2O_4$ is superparamagnetic at 300 K. Magnetic hysteresis with higher H_c observed at 30 K signifies the state of the blocked magnetic moment below T_B. H_c of the 500 °C annealed sample is plotted as a function of temperature in Figure 6.5 (b). $T^{1/2}$ law behaviour expected from the H_c of the 1-d $CaFe_2O_4$ sample in the intermediate temperatures [SANC04] is evident from the inset in the figure.

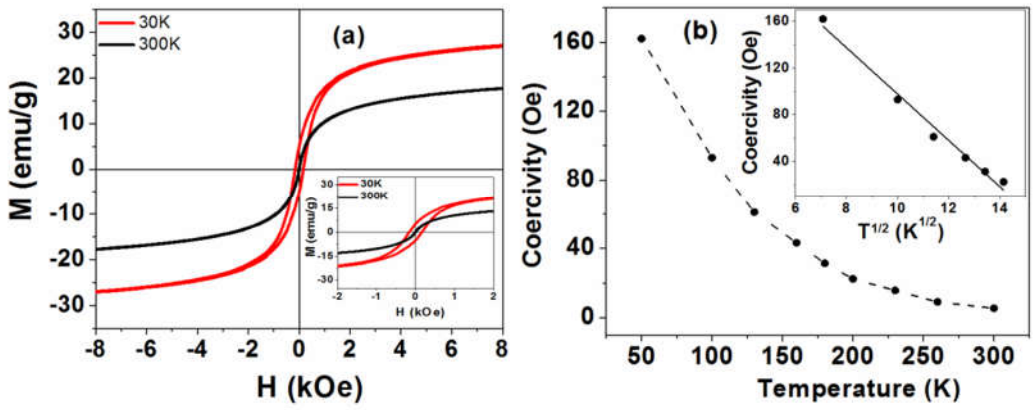

Figure 6.5: (a) M-H curves of the 500 °C annealed sample recorded at 30 and 300 K (b) Temperature dependence of coercivity of the 500 °C annealed sample. Inset shows $T^{1/2}$ power law dependence of the data in the intermediate temperatures.

Zero-field cooled (ZFC) and field cooled (FC) thermos-magnetization curves corresponding to the annealed samples recorded under an applied field of 500 Oe are shown in Figure 6.6. The ZFC magnetization curve shows a maximum value corresponding to the blocking temperature (T_B) at a certain low temperature depending on D_{av} of the nanoparticle. Below T_B of the nanoparticle, the single domain particle's magnetic moment is blocked. T_B decreases as the annealing temperature is increased for the 1-d $CaFe_2O_4$ samples. Such

temperature-dependent magnetization is also a characteristic feature of superparamagnetism in nanostructures. The superparamagnetic properties of $CaFe_2O_4$ nanoparticles show that the magneto-crystalline anisotropy (E_A) of the nanomaterial is a key parameter. The height of E_A decides the temperature range in which the thermal activation overcomes E_A and the nanoparticles show a superparamagnetic behavior. The relationship between the blocking temperature and the nanoparticle size reflects the size dependence of E_A. Here, blocking temperature has been plotted as a function of average crystallite size of the nanostructures and it is observed that the blocking temperature decreases with increasing crystallite size of the $CaFe_2O_4$ nanostructures which is shown in Figure 6.7.

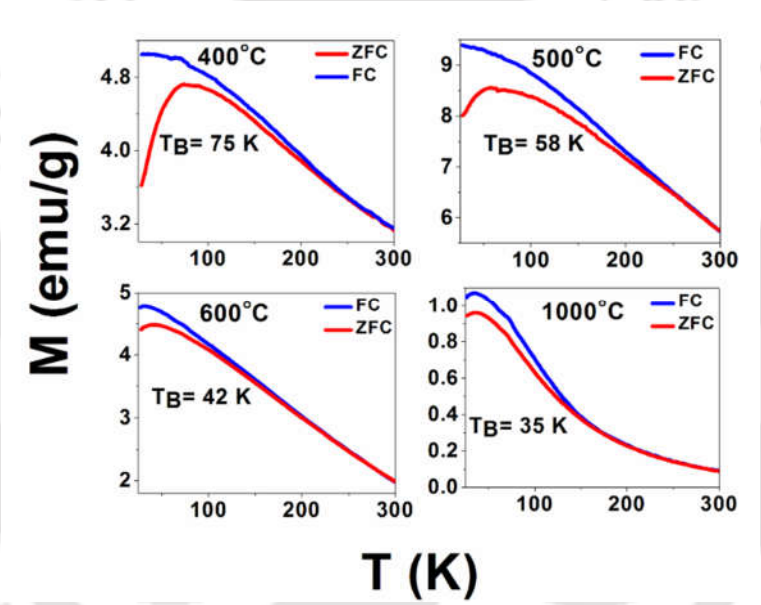

Figure 6.6: Thermo-magnetization curves of 1-d $CaFe_2O_4$ nanostructures obtained by annealing at 400 °C, 500 °C, 600 °C and 1000 °C.

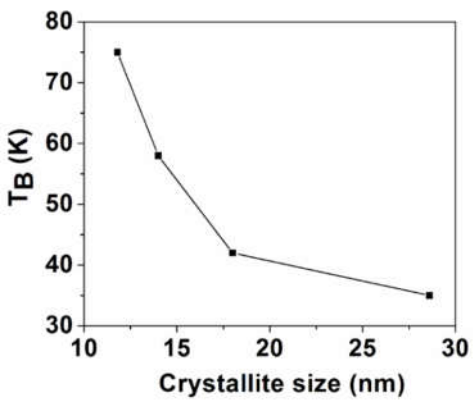

Figure 6.7: Variation of blocking temperature with crystallite size of 1-d $CaFe_2O_4$.

6.4. Summary

The following points summarize the salient results obtained from the work presented in this chapter.

- 1-d $CaFe_2O_4$ nanostructures consisting of interconnected $CaFe_2O_4$ beads have been prepared by electrospinning aqueous PVA solution containing metal precursors followed by annealing at temperatures between 400 and 1000 °C for 8h.
- Cubic nanocrystalline $CaFe_2O_4$ exhibits a transformation to orthorhombic phase when annealed above 500 °C. Annealing as-spun nanofibers at 1000 °C yielded single phase 1-d $CaFe_2O_4$ with orthorhombic structure.
- Cubic $CaFe_2O_4$ shows superparamagnetic behaviour and weak ferrimagnetic behaviour appears in the sample upon crystallization of the orthorhombic phase at temperatures above 500 °C.
- Blocking temperature of $CaFe_2O_4$ nanoparticles shifts with average crystallite size.
- This study shows subtle differences in the structural and magnetic properties of 1-d $CaFe_2O_4$ prepared by electrospinning as compared to 0-d $CaFe_2O_4$ nanoparticles.

Chapter 7

CONCLUSIONS AND SCOPE FOR FUTURE WORK

This chapter presents an overall summary of the work presented in this thesis and proposes some possibilities for future course of research in these topics

7.1. Conclusions

The main goal of this study was to develop 0-d and 1-d semiconducting and magnetic ferrite nanostructures with tailored physical, optical properties for application purpose. Here, undoped and TM doped ZnO based DMS material have been chosen for study to (1) obtain DMS with RTFM and high T_C which can be used in spintronic devices, and (2) to unravel the mechanism(s) leading to RTFM in this DMS. On the ferrite side, $CaFe_2O_4$ was taken up for study due to its unusual magnetic properties.

1-d undoped, ferromagnetic TM (Co) doped and non-magnetic TM (Mg) doped ZnO nanowires consisting of interconnected nanometer sized beads have been prepared by electrospinning method followed by heat treatment at different temperatures for 8h each. The investigations carried out on these nanostructures led to the following understanding:

- Heat treatment of as-spun undoped nanofibers results in formation of single phase hexagonal wurtzite structure. Apart from exhibiting RTFM, this 1-d ZnO exhibited the highest ever achieved T_C of 885 K. Maximum magnetization of 0.039 emu/g was observed for 500 °C annealed sample at an applied field of 10 kOe. A combined analysis of Raman, PL and EPR data revealed that singly ionized oxygen vacancy present in the annealed samples is responsible for the observed RTFM in undoped 1-d ZnO.
- Mg doped 1-d ZnO also exhibited single phase hexagonal structure of ZnO up to 5 wt.% Mg doping. No magnetization was observed in the Mg doped samples. Raman and PL spectra analysis showed the oxygen vacancy which was responsible for RTFM in the undoped sample decreased drastically upon Mg doping. Thus, Mg doping appears to quench the oxygen vacancies and hence magnetism in this system. However, considerable enhancement in band gap energy was observed upon Mg^{2+} doping in ZnO nanowires might help in our tryst to develop wide bandgap optoelectronic devices.
- Up to 3 wt.% Co could be incorporated in Zn^{2+} sites in 1-d ZnO without inducing impurity phase in the wurtzite structure as pointed out by XRD studies. However, Raman and EPR studies indicated the presence of an antiferromagnetic Co_3O_4 phase in samples with more than 2 wt.% Co. All Co doped samples exhibited RTFM. Interesting, no oxygen vacancy was detected in Raman or Pl studies. However, analysis of PL data showed that Zn vacancy present in the samples decreases upon increased Co doping. This ruled out both (oxygen and zinc) vacancies and impurity phase as possible sources of the observed RTFM in these samples. So, the RTFM is attributed to exchange interaction between local spin-polarized electrons and conduction electrons of Co.

- In conclusion, the mechanism responsible for RTFM in undoped and non-magnetic element doped 1-d ZnO appears to be different from the one in magnetic element doped 1-d ZnO. Based on the investigations carried out in this this thesis, different mechanisms can lead to the observed RTFM depending on the constitution of the DMS and there appears to be no universal mechanism for this phenomenon. These studies also showcase the potential of dopants like Mg and Co in 1-d ZnO for wide bandgap optoelectronic and spintronic applications.

The investigations carried out on $CaFe_2O_4$ nanoparticles prepared by sol-gel route and 1-d $CaFe_2O_4$ prepared by electrospinning routed have led to the following conclusions:

- As-synthesized cubic $CaFe_2O_4$ nanoparticles slowly transformed to orthorhombic phase when annealed above 300 °C and the transformation completes at 1100 °C. Superparamagnetic behavior is associated with the cubic phase and weak ferrimagnetic behaviour with the orthorhombic phase. 1100 °C annealed orthorhombic sample exhibited T_N at ~175 K. In an attempt to improve the magnetic properties, Co was substituted in Ca site. Phase transformation from cubic to orthorhombic phase was also observed in $Ca_{0.9}Co_{0.1}Fe_2O_4$. However, Co substitution induced precipitation of $CoFe_2O_4$ and a drastic change in magnetic properties. The cubic phase lost superparamagnetism and the orthorhombic phase exhibited higher magnetization.
- 1-d cubic $CaFe_2O_4$ also transformed to orthorhombic phase. However, the superparamagnetic cubic phase could be stabilized till 500 °C and single phase orthorhombic could be obtained at 1000 °C in this 1-d nanostructure. Apart from bringing out the subtle differences between 0-d and 1-d $CaFe_2O_4$, this work also shows for the first time a methodology to prepare cubic, mixed phase or orthorhombic $CaFe_2O_4$ with different magnetic properties.

7.2. Scope for future work

The present investigations on 0-d and 1-d ZnO was aimed at understanding the RTFM observed in this DMS. In that process, the possibility of tuning the optical and magnetic properties of ZnO nanostructures with proper doping has come to light. There is still a lot of scope for exploring the effect of various other TM elements in these compounds. Probing these DMS with synchrotron based X-ray absorption spectroscopy and X-ray circular magnetic dichroism may help in understanding the extrinsic or intrinsic nature of RTFM in

the ZnO nanostructures further. Considering the advantages demonstrated by 1-d nanostructures prepared by electrospinning route, it would be interesting to explore other TM doped DMS using this method. On the application side, it would be interesting to fabricate such inter-twined 1-d semiconductor nanostructures for catalytic and gas sensing applications.

1-d $CaFe_2O_4$ prepared for the first time in this work using electrospinning route has opened up this technique for preparing a wide variety of ferrites with novel 1-d nanostructure with large surface area. The potential of such novel nanostructures in memory and biomedical applications is worthy of investigation. Biocompatibilty of the $CaFe_2O_4$ prompts attempts to substitute other TM elements such as Ni, Zn, Mn, etc., in Ca site in $CaFe_2O_4$ with a view to obtain products best suited for applications such as targeted drug delivery and hyperthermia treatment of cancer.

References

[ABON07] A. Bonanni, Semicond Sci Tech. 22 (2007) R41

[ABRA69] S. C. Abrahams, J. L. Bernstein, Acta Crystallogr. B 25 (1969) 1233

[AKZA11] A.K. Zak, W.H.A. Majid, M.E. Abrishami, R. Yusefi, Solid State Sci., 13 (2011) 251

[ALBA73] G. Albanese, M. Carbucicchio, and A. Deriu, Il Nuovo Cimento B, 15 (1973) 147

[ANEY10] A. Ney, T. Kammermeier, K. Ollefs, S. Ye, V. Ney, T. C. Kaspar, S. A. Chambers, F. Wilhelm and A. Rogalev, Phys. Rev. B 81 (2010) 054420

[ARNA16] A. K. Das and A. Srinivasan, J. Magn. Magn. Mater. 404 (2016) 190

[ARNO07] Donna C. Arnold, Olga Kazakova, Guillaume Audoit, Joseph M. Tobin, Jaideep S. Kulkarni, Sergey Nikitenko, Michael A. Morris, and Justin D. Holme, Chem. Phys. Chem. 8 (2007) 1694

[ASHK03] N. Ashkenov, B. N. Mbenkum, C. Bundesmann, V. Riede, M. Lorenz, D. Spemann, E. M. Kaidashev, A. Kasic, M. Schubert, and M. Grundmann, J. Appl. Phys. 93, (2003) 126

[AVRU10] V. Avrutin, N. Izyumskaya, U. Ozgur, D. J. Silversmith and H. Morkoc, Proceedings of the IEEE 98 (2010) 1288

[AYKU13] Y. Aykut, G.N. Parsons, B. Pourdeyhimi, S.A. Khan, Langmuir 29 (2013) 4159

[BAAB15] M. M. Ba-Abbad, P. V. Chai, M. S. Takriff, A. Benamor and A. W. Mohammad, Mater. Design 86 (2015) 948

[BACH98] U. Bach, D. Lupo, P. Comte, J.E. Moser, F. Weissörtel, J. Salbeck, H. Spreitzer and M. Grätzel, Nature 395 (1998) 583

[BAIK05] J. M. Baik and J. L. Lee, Advanced Materials 17 (2005) 2745

[BARD54] J. Bardeen, F. J. Blatt, L. H. Hall, in proceedings of the conference on photoconductivity, Atlantic city, Breckenridge R. G, Russell B. R, and HahnE. E, (Edt.), John Wiley, New York, (1954) 146

[BART72] F. J. Bartoli and T. A. Litovitz, J. Chem. Phys. 56 (1972)404

[BEDI97] I. Bedja, Prashant V. Kamat, Xiao Hua, A. G. Lappin, and Surat Hotchandani, Langmuir 13 (1997) 2398

[BELG06] Y. Belghazi, G. Schmerber, S. Colis, J.L. Rehspringer, A. Dinia, A. Berrada, Appl. Phys. Lett. 89 (2006) 122504

[BERC10] L.J. Berchmans, M. Myndyk, K.L. Da Silva, A. Feldhoff, J. Subrt, P. Heitjans, K.D. Becker, V. Sepelak, J. Alloys Compds. 500 (2010) 68

[BERT66] E.F. Bertaut, J. Chappert, A. Apostolov, V. Semenov, Bull. Soc. Fr. Miner. Crystallogr. 89 (1966) 206

[BETH88] S. Bethke, H. Pan and B. Wessels, Appl. Phys. Lett. 52 (1988) 138

[BHAT08] D.K. Bhat, Nanoscale Res. Lett. 3 (2008) 31

[BINN14] Chris Binns, Nanomagnetism: Fundamentals and Applications, Volume 6 1st Edition, 6th June 2014 by Elsevier

[BLAX62] B. Lax and K. J. Button, Microwave Ferrites and Ferrimagnetics (McGraw Hill Book Company), New York, 1962

[BLIN01] B. Lin, Z. Fu and Y. Jia, Appl. Phys. Lett. 79 (2007) 943

[BLUN03] S. Blundell, Magnetism in Condensed Matter, Oxford University Press, Chapter 3 (2003)

[BOUB10] C.M. Boubeta, J.I. Beltran, Li Balcells, Z. Konstantinovic, S. Valencia, D.Schmitz, J. Arbiol, S. Estrade, J. Cornil, B. Martinez, Phys. Rev. B 82 (2010) 024405.

[BPAL14] B. Pal, S. Dhara, P.K.Giri, D.Sarkar, Journal of Alloys and Compounds. 615 (2014) 378

[BRIN90] C. Jeffrey Brinker and George W. Scherer, sol-gel science, Academic Press, 1990, Science

[BURD52] A. Burdese, Ric. Sci. 22 (1952) 259

[CALD07] M. J. Calderón and S. Das Sarma, Annals of Physics 322 (2007) 2618

[CALL77] J. M. Calleja and M. Cardona, Phys. Rev. B 16 (1977) 3753

[CAND04] R.A. Candeia, M.I.B. Bernardi, E. Longo, I.M.G. Santos, A.G. Souza, Mater. Lett.58 (2004) 569

[CETI12] S.S. Cetin, I. Uslu, A. Aytimur, S. Ozcelik, Ceram. Int. 38 (2012) 4201

[CHAK11] A. Chakrabarty and C. H. Patterson, Physical Review B 84 (2011) 054441

[CHAM09] S. A. Chambers, Advanced Materials 22 (2009) 219

[CHAN11] Y. Q. Chang, P. W. Wang, Q. L. Sun, Y. W. Wang and Y. Long, Journal of Nanomaterials 2011 (2011).

[CHAO00] Chao Liu, Bingsuo Zou, Adam J. Rondinone, and Z. John Zhang, J. Am. Chem. Soc. 122 (2000) 6263

[CHAR92] Charles Evans, Richard Brundle and Shaun Wilson, Encyclopedia of Materials Characterization, (1992) Elsevier

[CHEN08] Y. F. Chen, D. Spoddig and M. Ziese, Journal of Physics D: Applied Physics 41 (2008) 205004

[CHEN12] G. Chen, C. Song, C. Chen, S. Gao, F. Zeng and F. Pan, Advanced Materials 24 (2012) 3515

[CHEN13] L. Chen, F. Matsukura and H. Ohno, Nat Commun 4 (2013).

[CHEN98] Qi Chen and Z. John Zhang, Appl. Phys. Lett. 73 (1998) 3156

[CHEN99] Q. Chen, A. Rondinone, B. Chakoumakos, Z. Zhang, J. Magn. Magn. Mater. 194 (1999) 1

[CHHS10] C.-H. Hsu and. H. Chen, Nanotechl. 21 (2010) 285603

[CHIK13] E. Chikoidze, M. Boshta, M. H. Sayed and Y. Dumont, Journal of Applied Physics 113 (2013) 4

[CHIN00] C N Chinnasamy, A Narayanasamy, N Ponpandian, K Chattopadhyay, H Guerault and J-M Greneche, J. Phys.: Condens. Matter 12 (2000) 7795

[CIOR09] M. Ciorga, A. Einwanger, U. Wurstbauer, D. Schuh, W. Wegscheider and D. Weiss, Physical Review B 79 (2009) 165321

[CLAU07] A. F. F. N. V. D. Claude Chappert, Nature Materials 6 (2007) 813

[CLEE04] E.C. Lee and K. J. Chang, Physical Review B 69 (2004) 085205.

[CLIU00] Chao Liu, Bingsuo Zou, Adam J. Rondinone, and Z. John Zhang, J. Am. Chem. Soc. 122 (2000) 6263

[CLIU00a] C. Liu, B. Zou, A.J. Rondinone, Z.J. Zhang, J. Phys. Chem. B 104 (2000) 1141

[CMFU05] C. M. Fu, Y. F. Wang, Y. F. Guo, T. Y. Lin, and J. S. Chiu, IEEE Transactions on Magnetics, 41 (2005) 4120
[COEY05] J.M.D. Coey, M. Venkatesan and C.B. Fitzgerald, Nat. Mater. 4 (2005) 4
[COEY07] J.M.D. Coey, M. Venkatesan and C.B. Fitzgerald, Nature Mater 4 (2007) 173
[COEY08] J. M. D. Coey, K. Wongsaprom, J. Alaria and M. Venkatesan, Journal of Physics D: Applied Physics 41 (2008) 134012
[COEY08a] J. M. D. Coey and S. A. Chambers, MRS Bulletin 33 (2008) 1053
[COEY10] J. M. D. Coey, P. Stamenov, R. D. Gunning, M. Venkatesan and K. Paul, New Journal of Physics 12 (2010) 053025
[CONG09] C.J. Cong, J.H. Hong, K.L. Zhang, Mater. Chem. Phys. 113 (2009) 435
[CORL67] L.M. Corliss, J.M. Hastings, W. Kunnmann, Phys. Rev. 160 (1967) 408
[CULI72] B. D. Culity, Introduction to Magnetic Materials (Addison-Wesley Publishing Company, Inc. Massachusetts, 1972
[CULL13] B.D. Cullity, S.R. Stock, Elements of X-Ray Diffraction, 3rd edn. (Pearson, 2013)
[CXU005] C. Xu, M. Kim, J. Chun and D. Kim, Appl. Phys. Lett. 86 (2005) 133107
[CZIC06] H. Czichos, T. Saito, L. Smith, Handbook of materials measurements methods, Springer, Berlin (2006)
[DAME66] T. C. Damen, S. P. S. Porto, and B. Tell, Phys. Rev. 142 (1966) 570
[DATT90] S. Datta and B. Das, Appl. Phys. Lett. 56 (1990) 665
[DDAW07] D. D. Awschalom and M. E. Flatte, Nature Physics 3 (2007) 153
[DEBE11] A. Debernardi and M. Fanciulli, Physical Review B 84 (2011) 024415
[DECK57] B. F. Decker and J. S. Kasper, Acta Cryst. 10 (1957) 332
[DENG10] S. Z. F. Deng, H. M. Wang, M. Zheng, M. R. Yi, J. B. Wu, and H. R. S. R. Q. Tan,C. H. Ding, J. Feng, Y. P. Loh, K. P., ACS Nano 495 (2010) 495
[DGAO09] D. Gao, Z. Zhang, J. Fu, Y. Xu, J. Qiand, D. Xue, J. Appl. Phys. 105 (2009) 113928
[DIEB03] U. Diebold, Surface Science Reports 48 (2003) 53
[DIET00] T. Dietl, H. Ohno, F. Matsukura, J. Cibert and D. Ferrand, Science 287 (2000) 1019
[DIET01] T. Dietl, H. Ohno and F. Matsukura, Physical Review B 63 (2001) 195205
[DIET03] T. Dietl, Nature materials 2 (2003) 646
[DIET10] T. Dietl, Nature materials 9 (2010) 965
[DIET14] T. Dietl and H. Ohno, Reviews of Modern Physics 86 (2014) 187
[DJUR07] A. B. Djurišic, Y. H. Leung, K H Tam, Y F Hsu, L Ding, W K Ge, Y C Zhong, K SWong, W K Chan, H L Tam, K W Cheah, W M Kwok and D L Phillips, Nanotechnol.,18 (2007) 095702
[DJUR12] A.B. Djurišić, X. Chen, Y. H. Leung, A.M.C. Ng, J. Mater. Chem. 22 (2012) 6526
[DORM97] J. L. Dormann, D. Fiorani, and E. Tronc, Adv. Chem. Phys. 98 (1997) 283
[DRES07] M. S. Dresselhaus, Y.-M. Lin, O. Rabin, M. R. Black, J. Kong and G. Dresselhaus, in Springer handbook of nanotechnology, edited by B. Bhushan (Springer, Berlin, Germany, 2007), pp. 113-153.
[ECLE04] E.C. Lee and K. J. Chang, Physical Review B 69 (2004) 085205

[FENG13] T. Yu-Feng, H. Shu-Jun, Y. Shi-Shen and M. Liang-Mo, Chinese Physics B 22 (2013) 088505

[FETI06] Y. K. Fetisov, A. A. Bush, K. E. Kamentsev, A. Y. Ostashchenko, and G.Srinivasan, IEEE Sensors Journal, 6 (2006) 935

[FINK89] D. G. Fink, D. Christiansen, Electronics engineers' handbook, McGrawHill, 1989

[FMAT14] F. Matsukura and H. Ohno, in Nanomagnetism and Spintronics (Second Edition), edited by T. Shinjo (Elsevier, Oxford, 2014), pp. 315-358.

[FORT80] M. Fortes and M.R. Okos, Advances in Drying, Vol. 1. Ed. A.S. Mujumdar (Hemisphere, New York, 1980), pp. 119-154

[FPAN08] F. Pan, C. Song, X. J. Liu, Y. C. Yang and F. Zeng, Materials Science and Engineering: R: Reports 62 (2008) 1

[FREN30] J. Frenkel and J. Dorfman, Nature 126 (1930) 274

[FUKU99] T. Fukumura, Z. Jin, A. Ohtomo, H. Koinuma and M. Kawasaki, Applied Physics Letters 75 (1999) 3366

[FURU03] Akihiro Furube, Ryuzi Katoh, Kohjiro Hara, Shigeo Murata, Hironori Arakawa, and M. Tachiya, J. Phys. Chem. B 107 (2003), 4162

[GALL74] D. Galland, A. Herve, Solid State Commun. 14 (1974) 953.

[GAND14] V. Gandhi, R. Ganesan, H. Hameed, A. Syedahamed, M. Thaiyan, J. Phys. Chem. C 118 (2014) 9715

[GHOS13] S. Ghosh, G. G. Khan, A. Ghosh, S. Varma and K. Mandal, Cryst. Eng. Comm 15 (2013) 7748

[GILL97] G. D. Gilland, Mat. Sci. Eng. R 18 (1997) 99

[GIRI05] J. Giri, P. Pradhan, T. Sriharsha and D. Bahadurar, J. Appl. Phys. 97 (2005) 10Q916

[GOLD90] A. Goldman, Modern Ferrite Technology,Van Nostrand Reinhold, New York, 1990.

[GOVE02] K. Govender, D.S. Boyle, P. O'Brien, D. Binks, D. West and D. Coleman, Adv. Mater. 14 (2002) 1221

[GRAC02] N.Y. Graces, L. Wang, L. Bai, N.C. Giles, L.E. Halliburton, G. Cantwell, Appl. Phys. Lett. 80 (2002) 1334

[GRIM75] N. W. Grimes, Phys. Technol. 6 (1975) 22

[GRUN01] P. Grünberg, Phys. Today 54 (2001) 31

[GTDU06] G. T. Du, W. F. Liu, J. M. Bian, L. Z. Hu, H. W. Liang, X. S. Wang, A. M. Liu, and T. P. Yang, Appl. Phys. Lett. 89 (2006) 052113

[HAFE97] U. Hafeli, W. Schutt,J. Teller,M. Zborowski, Eds. Scientific and Clinical Applications of Magnetic Carriers; Plenum: New York, 1997

[HAGF95] A. Hagfeldth, M. Gratzel, Chem. Rev. 95 (1995) 49.

[HANE87] K. Haneda, Can. J. Phys. 65 (1987) 1233

[HASS11] M. Hassan, G. Springholz, R. T. Lechner, H. Groiss, R. Kirchschlager and G. Bauer, Journal of Crystal Growth 323 (2011) 363

[HAYS07] J. Hays, K M Reddy, N Y Graces, M H Engelhard, V Shutthanandan, M Luo, C. Xu, N C Giles, C Wang, S Thevuthasan, Journal of Physics: Condensed Matter,19 (2007) 26

[HERG06] Rudolf Hergt, Silvio Dutz, Robert Müller and Matthias Zeisberger, Journal of Physics: Condensed Matter 18 (2006) S2919

[HERN10] T. S. Herng, D. C. Qi, T. Berlijn, J. B. Yi, K. S. Yang, Y. Dai, Y. P. Feng, I. Santoso, C. Sánchez-Hanke, X. Y. Gao, A. T. S. Wee, W. Ku, J. Ding and A.Rusydi, Physical Review Letters 105 (2010) 207201

[HIMP98] F. J. Himpsel, J. E. Ortega, G. J. Mankey, and R. F. Willis, Adv. Phys 47 (1998) 511

[HIRA06] D. Hirabayashi, Y. Sakai, T. Yoshikawa, K. Mochizuki, Y. Kojima, K. Suzuki, K. Ohshita,Y. Watanabe, Hyperfine Interact., 167 (2006) 809

[HJXU10] H. J. Xu, H. C. Zhu, X. D. Shan, Y. X. Liu, J. Y. Gao, X. Z. Zhang, J. M. Zhang, P.W. Wang, Y. M. Hou and D. P. Yu, Journal of physics. Condensed matter: an Institute of Physics journal 22 (2010) 016002

[HOHN10] H. Ohno, Nature materials 9 (2010) 952

[HONG06] N.H. Hong, J. Sakai, N. Poirot, V. Brize, Phys. Rev. B 73 (2006) 132404

[HUAN01] M. H. Huang, Samuel Mao, H. Feick, H. Yan, Y. Wu, H. Kind, E. Weber, R. Russo, P. Yang, Science 292 (2001) 1897

[HUAN07] B. Huang, D. J. Monsma and I. Appelbaum, Appl. Phys. Lettr. 91 (2007) 072501

[HUAN17] Huan Xu, Wen Sun, Xu Qiu, Lixi Wang, Mingxun Yu and Qitu Zhang, J Mater Sci: Mater Electron. 28 (2017) 2803

[HYUN09] Hyun Gyu kim, Pramod H. Borse, Jum Suk Jang, Euh Duck Jeong, Ok-Sang Jung, Yong Jae Suh and Jae Sung Lee, Chem. Commum.(2009) 5889

[JANO06] A. Janotti and C. G. Van de Walle, J. Cryst. Growth 287 (2006) 58

[JANO07] A. Janotti and C. G. V. d. Walle, Phys. Rev. B 76 (2007) 165202

[JANO09] A. Janotti and C. G. V. d. Walle, Reports on Progress in Physics 72 (2009) 126501 (2009)

[JBAO06] J. Bao, Mariano A. Zimmler, and Federico Capasso, Nano Lett. 6 (2006) 1719

[JCUI06] J. Cui, Q. Zeng, and U.J. Gibson, J. Appl. Phys. 99 (2006) 08M113

[JEUN09] M. Jeun, S. Bae, A. Tomitaka, Y. Takemura, K.H. Park, S. H. Paek, K. W. Chung, Appl. Phys. Lett. 95 (2009) 082501

[JLIU09] J. Liu, S. Lee, Y.H. Ahn, J.-Y. Park and K. H. Koh, J. Phys. D: Appl. Phys. 42 (2009) 095401

[KAKA97] N.G. Kakazev, T.V. Sreckovic, M.M. Ristic, J. Mater. Sci. 32 (1997) 4619

[KASP08] T. C. Kaspar, T. Droubay, S. M. Heald, P. Nachimuthu, C. M. Wang, V. Shutthanandan, C. A. Johnson, D. R. Gamelin and S. A. Chambers, New J Phys 10 (2008) 055010

[KATA13] T. Kataoka, Y. Yamazaki, V. R. Singh, Y. Sakamoto, A. Fujimori, Y. Takeda, T.Ohkochi, S.-I. Fujimori, T. Okane, Y. Saitoh, H. Yamagami, A. Tanaka, M. Kapilashrami, L. Belova and K. V. Rao, Applied Physics Letters 99 (2011)13

[KATO04] R. Katoh, A. Furube, T. Yoshihara, K. Hara, G. Fujihashi, S. Takano, S. Murata, H. Arakawa, and M. Tachiya, J. Phys. Chem. B 108 (2004) 4818

[KATY02] K. S. A. H. Katyama-Yoshida, Semicond. Sci. Technol. 17 (2002) 367

[KEIS02] K. Keis, C. Bauer, G. Boschloo, J. Photochem. Photobiol. A 148 (2002), 57

[KHAL09] M. Khalid, M. Ziese, A. Setzer, P. Esquinazi, M. Lorenz, H. Hochmuth, M. Grundmann, D. Spemann, T. Butz, G. Brauer, W. Anwand, G. Fischer, W. A. Adeagbo, W. Hergert and A. Ernst, Physical Review B 80 (2009) 035331

[KHAN13] L. Khanna, N.K. Verma, J. Magn. Magn. Mater. 336 (2013) 1

[KHOR11] A. Khorsand Zak, W.H. Abd. Majid, M.E. Abrishami and Ramin Yousefi, Solid State Sciences 13 (2011) 251

[KITT05] K. R. Kittilstved, N. S. Norberg and D. R. Gamelin, Physical Review Letters 94 (2005) 147209

[KITT05a] Charles Kittel, Introduction to solid state physics, Willey 8th ed. 2005

[KITT46] C. Kittel, Phys. Rev. 70 (1946) 965

[KNUT10] R. Knut, J. M. Wikberg, K. Lashgari, V. A. Coleman, G. Westin, P. Svedlindh and O. Karis, Physical Review B 82 (2010) 094438

[KOHA00] A. F. Kohan, G. Ceder, D. Morgan, C. G. V. de Walle, Phys. Rev. B 61 (2000) 15019

[KOLE03] N. Kolev, M.N. Ileiv, V.N. Popov, M. Gospodinov, Solid State Commun. 128 (2003) 153

[KRYD96] M. H. Kryder, MRS Bull. 21 (1996) 17

[KUBE31] P. Kubelka and F. Munk, Z. Tech. Phys. 12 (1931) 593

[KUDR04] J. Kudrnovský, I. Turek, V. Drchal, F. Máca, P. Weinberger and P. Bruno, Physical Review B 69 (2004) 115208

[LAUR99] Laurence Bouet, Philippe Tailhades, Isabelle Pasquet, Corine Bonningue, Stéphane Le Brun, Abel Rousset, Jpn. J. Appl. Phys. 38 (1999) 1826

[LHU013] L. Hu, J. Huang, H. He, L. Zhu, S. Liu, Y. Jin, L. Sun and Z. Ye, Nanoscale 5 (2013) 3918

[LOBA11] L.S. Lobanovsky, S.V. Trukhanov, Crystallogr. Rep. 56 (2011) 482

[LONG71] G. Longworth and B. Window, J. Phys. D: Appl. Phys. 4 (1971) 835

[LOWN62] H. A. Lowenstam, Bulletin Geological Society of America, 73 (1962) 435

[LUKA12] I. Lukacevic, S. K. Gupta, P. K. Jha and D. Kirin, Materials Chemistry and Physics 137 (2012) 282

[MACD05] A. H. MacDonald, P. Schiffer and N. Samarth, Nature materials 4 (2005) 195

[MAHA74] G.D. Mahan, J. Appl. Phys.54 (1983) 3825

[MAHA83] G.D. Mahan, J. Appl. Phys. 54 (1983) 3825

[MAKI01] T. Makino, N.T. Tuan, H.D. Sun, C.H. China, Y. Segawa, M. Kawasaki, A. Ohotomo, K. Tamura, T. Suemoto, H. Akiyama, M. Baba, T. Tomita, H. Koinuma, Appl. Phys. Lett. 78 (2001) 1979

[MART98] C. R. Martin and D. T. Mitchell, "Nanomaterials in analytical chemistry," Analytical Chemistry 70 (1998) 322A

[MATS01] Y. Matsumoto, M. Murakami, T. Shono, T. Hasegawa, T. Fukumura, M. Kawasaki, P. Ahmet, T. Chikyow, S.-y. Koshihara and H. Koinuma, Science 291(2001) 854

[MCCA97] G. H. McCabe, T. Fries, M. T. Liu, Y. Shapira, L. R. Ram-Mohan, R. Kershaw, A. Wold, C. Fau, M. Averous and E. J. McNiff, Physical Review B 56 (1997) 6673

[MCCU94] R. A. McCurrie, Ferromagnetic Materials structure and properties, University of Bradford, UK (1994)

[MCMI92] R. D. McMichael, R. D. Shull, L. J. Swartzendruber, and L. H. Bennett, J. Magn. Magn. Mater. 111 (1992) 29

[MEAD77] D. G. Mead and G. R. Wilkinson, J. Raman Spectrosc.6 (1977) 123

[MESA14] Mesaros A., Ghitulica C.D., Popa M., Mereu R., Popa A., Petrisor Jr. T., Gabor M., Cadis A.I., Vasile B.S., Ceram. Inter. 40 (2014) 2835

[MITC97] D. G. Mitchell, J. Magn. Reson. Imaging 7 1997) 7

[MOHA14] D. K. P. Mohanty, R.K. Mandal, P.K. Kulriya, A.S.K. Sinha, Chandana Rath, J. Magn. Magn. Mater. 355 (2014) 240

[MORA07] A. E. Morales, E. S. a. Mora and U. Pal, Revista Mexicana De F´Isica S 53 (2007) 18

[MOUN96] N. Moumen, P. Bonville, M. P. Pileni, J. Phys. Chem., 100 (1996)14410

[NAEE12] M. Naeem and S. K. Hasanain, Journal of physics. Condensed matter: An Institute of Physics journal 24 (24), 245305 (2012)

[NHOA13] N. Hoa and D. Huyen, J Mater Sci: Mater Electron 24 (2013) 793

[NORB04] N. S. Norberg, K. R. Kittilstved, J. E. Amonette, R. K. Kukkadapu, D. A. Schwartz and D. R. Gamelin, Journal of the American Chemical Society 12 (2004) 9387

[OHNO00] H. Ohno, D. Chiba, F. Matsukura, T. Omiya, E. Abe, T. Dietl, Y. Ohno and K.Ohtani, Nature 408 (2000) 944

[OHNO96] H. Ohno, A. Shen, F. Matsukura, A. Oiwa, A. Endo, S. Katsumoto and Y. Iye, Applied Physics Letters 69 (1996) 363

[OHTO98] A. Ohtomo, M. Kawasaki, T. Koida, K. Masubuchi, H. Koinuma, Y. Sakurai, Y. Yoshida, T. Yasuda, Y. Segawa, Appl. Phys. Lett. 72 (1998) 2466

[OHYA10] S. Ohya, I. Muneta and M. Tanaka, Applied Physics Letters 96 (2010) 052505

[OLEJ08] K. Olejník, M. H. S. Owen, V. Novák, J. Mašek, A. C. Irvine, J. Wunderlich and T.Jungwirth, Physical Review B 78 (2008) 054403

[OLSO06] D. C. Olson, Jorge Piris, Reuben T. Collins, Sean E. Shaheen, David S. Ginley, Thin Solid Films 496 (2006) 26

[OPEL12] M. Opel, Journal of Physics D: Applied Physics 45 (2012) 033001

[OZGU05] Ü. Özgür, Y. I. Alivov, A. T. C. Liu, M. A. Reshchikov, S. Dogan, V. Avrutin, S.J. Cho and H. Morkoçd, J. Appl. Phys. 98 (2005) 041301

[PANI08] B. Panigrahy, M. Aslam and D. Bahadur, The Journal of Physical Chemistry C 114 (2010) 11758.

[PANI10] B. Panigrahy, M. Misra, D. S. Ghosh, M. Bahadur, Adv. Funct. Mater. 20 (2010) 1161

[PANI12] B. Panigrahy, M. Aslam and D. Bahadur, Nanotechnology 23 (2012) 11

[PARK90] J.C. Parker and R.W. Seigel, Appl. Phys. Lett. 57 (1990) 943

[PATT06] C. H. Patterson, Physical Review B 74 (2006) 144432

[PDEV10] P. Dev, H. Zeng and P. Zhang, Physical Review B 82 (2010), 165319

[PEAR03] S. J. Pearton, C. R. Abernathy, M. E. Overberg, G. T. Thaler, D. P. Norton, N. Theodoropoulou, A. F. Hebard., Y. D. Park, F. Ren, J. Kim, L. A. sBoatner, J.Appl. Phys. 93 (2003) 1

[PEAR07] S. J. Pearton, D. P. Norton, M. P. Mil, A. F. Hebard, J. M. Zavada, W. M. Chen and I. A. Buyanova, Electron Devices, IEEE Transactions on 54 (2007) 1040

[PENG09] H. Peng, H. J. Xiang, S.-H. Wei, S.-S. Li, J.-B. Xia and J. Li, Physical Review Letters 102 (2009) 017201

[PHAN13] T.L. Phan, Y.D. Zhang, D.S. Yang, N.X. Nghia, T.D. Thanh, S.C. Yu, Appl.Phys. Lett. 102 (2013) 072408

[PICO04] S. Picozzi, Nature materials 3 (2004) 349

[PORT67] S. P. S. Porto and R. S. Krishnan, J. Chem. Phys. 47 (1967) 1009

[PRAD04] A.K. Pradhan, K. Zhang, G.B. Loutts, U.N. Roy, Y. Cui, A. Burger, J. Phys. Condens. Matter 16 (2004) 7123

[PRAS98] S. Prasad, N. S. Gajbhiye, J. Alloys Compd. 265 (1998) 87

[PRIN98] G. A. Prinz, Science 282 (1998) 1660

[QLI012] Q. Li, T. T. Shen, Z. K. Dai, Y. L. Cao, S. S. Yan, S. S. Kang, Y. Y. Dai, Y. X.Chen, G. L. Liu and L. M. Mei, Appl. Phys. Lett. 101 (2012) 172405

[RAJA00] M. Rajalakshmi, A. K. Arora, B. S. Bendre, and S. Mahamuni, J. Appl.Phys. 87 (2000) 2445

[RAMA05] S. Ramakrishna, K. Fujihara, W.E Teo, (2005) An Introduction to Electrospinning and Nanofibers, World Scientific Pub. Singapore.

[RAMA06] S. Ramachandran, J. Narayan, J.T. Prater, Appl. Phys. Lett. 88 (2006) 242503

[RANA10] S. Rana, J. Philip, B. Raj, Mater. Chem. Phys. 124 (2010) 264

[RAVI06] P. Ravirajan, A. M. Peiró, M. K. Nazeeruddin, M. Graetzel, Donal D. C. Bradley, James R. Durrant, and Jenny Nelson, J. Phys. Chem. 110 (2006) 7635

[ROMC10] N. Romcevica, R. Kostica, B. Hadžica, M. Romcevica, I. Kuryliszyn-Kudelskab, W.D. Dobrowolskib, U. Narkiewiczc and D. Siberac, J. Alloys Compds. 507 (2010) 386

[ROSA15] Rosa A. Lukaszew, Handbook of Nanomagnetism: Applications and Tools October 6, 2015 by Pan Stanford

[ROTH64] W. L. Roth, J. Phys. Chem. Solids, 25 (1964) 1

[ROUT06] C. S. Rout, A. R. Raju, A. Govindaraj, C. N. R. Rao, Solid State Commun. 138 (2006) 136

[RUBI07] D. Rubi, J. Fontcuberta, A. Calleja, L. Aragonès, X. G. Capdevila and M. Segarra, Physical Review B 75 (2007) 155322

[RUDE54] M.A. Ruderman, C. Kittel, Phys. Rev. 96 (1954) 99

[SAMA05] K. Samanta, P. Bhattacharya, and R.S. Katiyar, Appl. Phys. Lett. 87 (2005) 101903

[SAMA13] A. Samariya, S.N. Dolia, A.S. Prasad, P.K. Sharma, S.P.Pareek, M.S. Dhawan, S. Kumar, Curr. Appl. Phys. 13 (2013) 830

[SANC04] R. D. Sanchez, C. A. Ramos, J. Rivas, P. Vaqueiro, M. A. Lopez-Quintela, Physica B 354 (2004) 104

[SANC08] N. Sanchez, S. Gallego and M. C. Muñoz, Physical Review Letters 101 (2008) 067206

[SANG14] L. Sang, Y. Zhao and C. Burda, Chemical Reviews 114 (2014) 9283

[SATO00] K. Sato and H. Katayama-Yoshida, Jpn J Appl Phys 2 39 (6B) (2000) L555

[SATO01] K. Sato and H. Katayama-Yoshida, Jpn. J. Appl Phys 2 40 (4A) (2001) L334

[SAWO01] S. A. Wolf, D. D. Awschalom, R. A. Buhrman, J. M. Daughton, S. von Molnár, M.L. Roukes, A. Y. Chtchelkanova and D. M. Treger, Science 294 (2001) 1488

[SCHR06] D. K. Schroder, Semiconductor material and device characterization, 3rd ed., Wiely Interscience , New Jercy, USA (2006)

[SCHU05] T. C. Schulthess, W. M. Temmerman, Z. Szotek, W. H. Butler and G. Malcolm Tocks, Nature materials 4 (2005) 838

[SCHW04] D. A. Schwartz and D. R. Gamelin, Advanced Materials 16 (2004) 2115

[SDAS03] S. Das Sarma, Nature materials 2 (2003) 292

[SHAR12] Ibrahim Sharifi, H.Shokrollahi and S. Journal of Magnetism and Magnetic Materials 324 (2012) 903

[SHE012] S. He, H. Bai, G. Liu, Q. Li, S. Yan, Y. Chen, L. Mei, H. Liu, S. Wang and X.Han, Applied Physics Letters 100 (2012)132406

[SHIN04] S.R. Shinde, S.B. Ogale, J.S. Higgins, H. Zheng, A.J. Millis, V.N. Kulkarni, R.Ramesh, R.L. Greene, T. Venkatesan, Phys. Rev. Lett. 92 (2004) 166601

[SLUI05] M. H. F. Sluiter, Y. Kawazoe, P. Sharma, A. Inoue, A. R. Raju, C. Rout and U. V. Waghmare, Physical Review Letters 94 (2005) 187204

[SMIT53] J. Smith and H. P. J. Wijn, Ferrites (Philiphs Technical Library, Eindhoven, Haneda, Can. J. Phys. 65 (1987) 1233

[SRIN13] G. Srinet, R. Kumar and V. Sajal, Journal of Applied Physics 114 (2013)

[STON47] E. C. Stoner and E. P. Wohlfarth, Philos. Trans. R. Soc. A 240 (1948) 599

[STRO01] M. A. Stroscio and M. Dutta, Phonons in Nanostructures Cambridge University Press, Cambridge, 2001

[SUND06] A. Sundaresan, R. Bhargavi, N. Rangarajan, U. Siddesh, C. N. R. Rao, Phys. Rev. B. 74 (2006) 161306

[SUND09] A. Sundaresan and C. N. R. Rao, Nano Today 4 (2009) 96

[SVOB04] J. Svoboda, Magnetic Techniques for the Treatment of Materials, Kluwer Academic Publishers, Dordrecht (2004)

[TANG92] Z. X. Tang, C. M. Sorensen, K. J. Klabunde, and G. C. Hadjipanayis, Phys. Rev.Lett. 67 (1991) 3602

[TAUC66] J. Tauc, R. Grigorovici, A. Vancu, Physica Status Solidi (b) 15 (1996) 627

[TCYE95] T. C. Yeh, W. Zhang, S. T. Ildstad, and C. Ho.,Magnetic Resonance in Medicine, 33 (1995) 200

[TFLI07] T. F. Li, H. Qiu, P. Wu, M. W. Wang and R. X. Ma, Thin Solid Films 515 (2007) 3905

[THAN10] A. A. Thant, S. Srimala, P. Kaung, M. Itoh, O. Radzali, M.N. Ahmad Fauzi, J. Australian Ceram. Soc. 11 (2010) 46

[THON01] K. Thonke, T. Gruber, N. Teofilov, R. Schönfelder, A. Waag, and R. Sauer, Physica B 308 (2001) 945

[TIEN05] L. C. Tien, P. W. Sadik, D. P. Norton, L. F. Voss, and S. J. Pearton, Appl. Phys. Lett. 87 (2005) 222106

[TRAV08] Travis J. Sill and Horst A. von Recum, Biomaterials 29 (2008) 1989

[VALE12] Rau´l Valenzuela, Novel appications of Ferrites, Physics Research International (2012)

[VALE94] R. Valenzuela, Magnetic Ceramics, Chemistry of Solid State Materials Series Ed. B.Dunn, J. W. Goodby and A. R. West, (Cambridge Univ. Press, Cambridge, 1994).

[VANH96] K. Vanheusden, W. L. Warren, C. H. Seager, D. R. Tallant, J. A. Voigt, B. E. Gnade, J. Appl. Phys. 79 (1996) 7983

[VENK04] M. Venkatesan, C. B. Fitzgerald, J. G. Lunney and J. M. D. Coey, Physical Review Letters 93 (2004) 177206

[VERM06] A. Verma, M. I. Alam, R. Chatterjee, T. C. Goel, and R. G. Mendiratta, J. Magn. Magn. Mater. 300 (2006) 500

[VISW90] B. Viswanathan and V. R. K. Murthy, Ferrite Materials: Science and technology Narosa Publishing House, New Delhi, 1990

[WALK12] C. D. Walkey, J. B. Olsen, H. Guo, A. Emili, W. Chan, J. Am. Chem. Soc., 134 (2012) 2139

[WALS08] A. Walsh, J. L. F. Da Silva and S.H. Wei, Physical Review Letters 100 (2008) 256401

[WANG05] H. T. Wang, B. S. Kang, and F. Ren, Appl. Phys. Lett. 86 (2005) 243503

[WANG06] Z. L. Wang and J. Song, Science 312 (2006) 242

[WANG06a] Y.S. Wang, P. John Thomas, P. O'Brien, J. Phys. Chem. B 110 (2006) 21412

[WANG08] X. Wang, R. Zheng, Z. Liu, H. P. Ho, J. Xu and S. P. Ringer, Nanotechnology 19 (2008) 455702

[WANG08a] J. Wang, L. Cywinski, C. Sun, J. Kono, H. Munekata and L. J. Sham, Physical Review B 77 (2008) 235308

[WANG13] M. Wang, K. W. Edmonds, B. L. Gallagher, A. W. Rushforth, O. Makarovsky, A. Patanè, R. P. Campion, C. T. Foxon, V. Novak and T. Jungwirth, Physical Review B 87 (2013) 121301

[WHIT03] G. M. Whitesides, Nat. Biotechnol. 21 (2003) 1161

[WLIU11] W. Liu, W. Li, Z. Hu, Z. Tang, X. Tang, J. Appl. Phys. 110 (2011) 013901.

[XING11] G.Z. Xing, Y.H. Lu, Y.F. Tian, J.B. Yi, C.C. Lim, Y.F. Li, G.P. Li, D.D. Wang, B. Yao, J. Ding, Y.P. Feng and T. Wu, AIP Advances 1 (2011) 022152

[XLIU06] X. Liu, F. Lin, L. Sun, W. Cheng, X. Ma and W. Shi, Applied Physics Letters 88 (2006) 6

[XMLI07] X.M. Liu, G. Yang, S.Y. Fu, Mater. Sci. Eng. C 27 (2007) 750

[YANG06] C. Yang, F. Liu, T. Ren et al., Sensors and Actuators A, vol. 130-131, pp. 365–370, 2006

[YANG14] X. Li and J. Yang, Journal of Materials Chemistry C 2 (2014)7071

[YFLU00] Y. F. Lu, H. Q. Ni, and Z. M. Ren, J. Appl. Phys. 88 (2000) 498

[YLIN09] C.Y. Lin, W.H. Wang, C.-S. Lee, K.W. Sun, Y.W. Suen, Appl. Phys. Lett. 94 (2009) 151909

[YLIU09] Y. Liu, J. Yang, Q. Guan, L. Yang, Y. Zhang, Y. Wang, B. Feng, J. Cao, X. Liu, Y. Yang, M. Wei, J. Alloys Compounds. 486 (2009) 835 (2011) 251

[YPAN06] D. Y. Pan, G. L. Xu, L. Y. Lv, Y. Yong, X. W. Wang, J. G. Wan and G. H. Wang, Appl. Phys. Lett. 89 (2006) 082510

[YWHE04] Y. W. Heo, D. P. Norton, L. C. Tien, Y. Kwon, B. S. Kang, F. ren, S. J. Pearton and J. R. Laroche, Mater. Sci. Eng. R 47 (2004) 1

[YWU09] Y. Wu, X.-H. Zhang, F. Xu, L.-S. Zheng and J. Kang, Nanotechnol. 20, (2009) 325709

[ZASP04] V. Zaspalis, V. Tsakaloudi, E. Papazoglou, M. Kolenbrander, R.Guenther, and P.V. D. Valk, Journal of Electroceramics, 13 (2004) 585

[ZELE10] A. Zelenkova, J. Kovác, and V. Zelenák, J. Appl. Phys. 108 (2010) 034323

[ZENE51] C. Zener, Physical Review 83 (1951) 299

[ZHAN06] Z. Zhanga, Q. Chen, H. D. Lee, Y. Y. Xue, Y. Y. Sun, H. Chen, F. Chen, and Wei-Kan Chu, journal of applied physics, 100 (2006) 043909

[ZHAN09] Y. Wu, X.-H. Zhang, F. Xu, L.-S. Zheng and J. Kang, Nanotechnol. 20 (2009) 325709

[ZHAN13] Y. Zhang, Z. Wang and J. X. Cao, Journal of Applied Physics 113 (2013) 203913

[ZHAN98] C. Zhang, H. Vali, C. S. Romaner, T. J. Phelps, and S. V. Liu, American Mineralogist,83 (1998) 1409

[ZHAO10] M. Zhao, X. Wang, L. Ning, H. He, J. Jia, L. Zhang, X. Li, J. Alloys Compd. 507 (2010) 97

[ZUKO06] A. Zukova, A. Teiserskis, S. van Dijken, Y. K. Gun'ko and V. Kazlauskiene, Applied Physics Letters 89 (2006) 233902

[ZUTI04] I. Žutic, J. Fabian and S. Das Sarma, Reviews of Modern Physics 76 (2004) 323

Publications/communications originating from the thesis work:
In journals:

1. **Arnab Kumar Das**, Manoranjan Kar and Ananthakrishanan Srinivasan, "Room temperature ferromagnetism in undoped ZnO nanofibers prepared by electrospinning" Physica B **448** (2014) 112
2. **Arnab Kumar Das** and Ananthakrishnan Srinivasan, "Evidence of oxygen defect induced ferromagnetism in heat treated electrospun ZnO nanowires", J. Magn. Magn. Mater. **404** (2016) 190
3. **Arnab Kumar Das** and Ananthakrishnan Srinivasan, "Band gap tuning and defects suppression upon Mg doping in electrospun ZnO nanowires", J. Mater. Sci. Mater. Electron. **28** (2017) 6488
4. **Arnab Kumar Das** and Ananthakrishnan Srinivasan, "Magnetic and structural properties of Co doped ZnO nanowires prepared by heat treatment of electrospun PVA nanofibers containing Zn and Co acetates", J. Mater. Sci. Mater. Electron. **29** (2018) 4351
5. **Arnab Kumar Das** and Ananthakrishnan Srinivasan, "Structural and magnetic properties of sol-gel derived $CaFe_2O_4$ nanoparticles", J. Magn. Magn. Mater. **451** (2018) 526
6. **Arnab Kumar Das** and Ananthakrishnan Srinivasan, "Structural transition and associated magnetic properties of heat treated electrospun one-dimensional $CaFe_2O_4$" (communicated)

Publications not part of the thesis work:

1. Bhagaban Kisan, P. Ravikumar, **Arnab Kumar Das**, A. Srinivasan and A. Perumal, "Structural, Vibrational, Optical and magnetic properties of NiO nanoparticles" J. Sci. Lett 4 (2015) 160
2. **Arnab Kumar Das**, Rajkumar Modak and Ananthakrishnan Srinivasan, "Structural and optical properties of electrospun MoO_3 nanowires" AIP Conference Proceedings 1953 (2018) 030021

In Conferences:

1. Arnab Kumar Das and A. Srinivasan, "Magnetic properties of heat treated PVA nanofibers containing transition metal (Zn, Co) salts"

   Presented in The International Conference on Magnetic Materials and Applications (ICMAGMA - 2017), Leonia Holistic Resorts, Hyderabad, 1 - 3 February 2017.

2. Arnab Kumar Das and A. Srinivasan, "Structural and morphological studies of Mg doped ZnO nanowires prepared by electrospinning route"

   Presented in The NANOS-2015, GITAM University, Visakhapatnam,14-17 December 2015.

3. Arnab Kumar Das and A. Srinivasan, "Magnetic properties of $CaFe_2O_4$ nanoparticles prepared by solvothermal method"

   Presented in The EMCA-2014, CGCRI, Kolkata,4-6 December 2014

4. Arnab Kumar Das and A. Srinivasan, "Structural and optical properties of Mg doped ZnO nanowires prepared by electrospinning route"

   Presented in The ICONSAT-2014, Punjab University, 2-5 March 2014

5. Arnab Kumar Das and A. Srinivasan, "Room temperature ferromagnetism of ZnO nanofibers prepared via electrospinning"

   Presented in MAGMA-2013, IIT Guwahati, 5-7 December 2013

* * * * * * * * * *